UNIVERSIDADE DE SÃO PAULO
Escola de Engenharia de São Carlos

Comparison between Backprojection and Algebraic Methods for ultrasound tomography of concrete elements

Comparação entre Retroprojeção e Métodos Algébricos para Tomografia Ultrassônica de Elementos de Concreto

Lara Guizi Anoni

Dissertação de Mestrado do Programa de Pós-Graduação em Engenharia Civil (Engenharia de Estruturas) da Escola de Engenharia de São Carlos, Universidade de São Paulo.

EESC · USP

LARA GUIZI ANONI

Comparison between Backprojection and Algebraic Methods for ultrasound tomography of concrete elements

Comparação entre Retroprojeção e Métodos Algébricos para tomografia ultrassônica de elementos de concreto

This dissertation was submitted to the Post-Graduate Program in Civil Engineering (Structural Engineering) of the São Carlos School of Engineering at the University of São Paulo for the degree on Master of Science.

Dissertação apresentada ao Programa de Pós-Graduação em Engenharia Civil (Engenharia de Estruturas) da Escola de Engenharia de São Carlos da Universidade de São Paulo para a obtenção do Título de Mestre em Ciências.

Advisor: Prof. Dr. Vladimir Guilherme Haach

CORRECTED VERSION

(Original version is available at São Carlos School of Engineering)

São Carlos

2024

AUTORIZO A REPRODUÇÃO TOTAL OU PARCIAL DESTE TRABALHO, POR QUALQUER MEIO CONVENCIONAL OU ELETRÔNICO, PARA FINS DE ESTUDO E PESQUISA, DESDE QUE CITADA A FONTE.

Ficha catalográfica elaborada pela Biblioteca Prof. Dr. Sérgio Rodrigues Fontes da EESC/USP com os dados inseridos pelo(a) autor(a).

A613c

Anoni, Lara Guizi
Comparison between Backprojection and Algebraic Methods for ultrasound tomography of concrete elements / Lara Guizi Anoni; orientador Vladimir Guilherme Haach. São Carlos, 2024.

Dissertação (Mestrado) - Programa de Pós-Graduação em Engenharia Civil (Engenharia de Estruturas) e Área de Concentração em Estruturas -- Escola de Engenharia de São Carlos da Universidade de São Paulo, 2024.

1. Image Reconstruction. 2. Concrete. 3. Ultrasound. 4. Ultrasound Tomography. 5. Backprojection. 6. Algebraic Methods. 7. Ultrasonic. 8. FBP. I. Título.

Eduardo Graziosi Silva - CRB - 8/8907

FOLHA DE JULGAMENTO

Candidata: Bacharela **LARA GUIZI ANONI**.

Título da dissertação: "Comparação entre Retroprojeção e Métodos Algébricos para Tomografia Ultrassônica de Elementos de Concreto".

Data da defesa: 06/05/2024.

Comissão Julgadora	Resultado
Prof. Associado Vladimir Guilherme Haach (Orientador) (Escola de Engenharia de São Carlos/EESC-USP)	APROVADA
Prof. Dr. Lev Khazanovich (University of Pittsburgh)	APROVADA
Prof. Titular José Tadeu Balbo (Escola Politécnica/EP-USP)	APROVADA

Coordenador do Programa de Pós-Graduação em Engenharia Civil (Engenharia de Estruturas):
Prof Associado **Ricardo Carrazedo**

Presidente da Comissão de Pós-Graduação:
Prof. Titular **Carlos De Marqui Junior**

To my parents, who have always believed in me and taught me the value of perseverance.

ACKNOWLEDGMENTS

I would like to thank God for guiding my paths in the right direction, always.

Thank you to my parents, Jusela and Lucio, who support me in every step, celebrate with me the good opportunities and help me to overcome all difficulties. Your constant encouragement has led me to where I am today. I have no words to thank you for all you did for me. I would also like to thank my life partner, Felipe Santana Pena, for always listening and providing good advice, for sharing love and time, for understanding and supporting my choices, and for being with me to celebrate every achieved step.

Special gratitude is reserved for my advisor, Dr. Vladimir Guilherme Haach, for being patient and kind when I needed help, for listening to my ideas, and also supporting me in my choices. I am honored to have the opportunity to learn with him.

Thank you to Dr. Lev Khazanovich, who accepted me to be part of his research group for three months in the Department of Environmental and Civil Engineering at the University of Pittsburgh, and gave me support to develop my research. I extend a special thank you to the members of the research group: Igor Sukharev, Mason Smetana, and Kathryn Ann Kennebeck.

My gratitude extends to my qualification exam committee members and my final defense committee members for all contributions and time spent to improve my research.

A heartfelt thank you to my friends, for all support during the mandatory courses and during the experimental steps of my research, Gustavo Rocha, Luiz Mattos, Paulo Cunha, Marina Furukawa, Deborah Nardi, Matheus Yokomizo, Eduardo Hayashi, João Segala, Juliana Silva, Gabriel Spinola, Humberto Lima, and José Caio Carneiro. Also, during the experimental steps, the valuable assistance provided by Luiz Vareda, Romeu and Fabiano (Structural Lab), Oscar (Geotechnical Lab), and Paulo (Wood Lab) is greatly appreciated.

I also thank for the financial support during the 26 months of elaboration of the dissertation. This study was financed in part by the Coordenação de Aperfeiçoamento de Pessoal de Nível Superior – Brasil (CAPES) – Finance Code 001. This study was also financed with the support of the São Paulo Research Foundation (FAPESP) - processes number 2022/15224-0 and 2023/04604-0.

The opinions, hypotheses, and conclusions or recommendations expressed in this material are the responsibility of the author and do not necessarily reflect the views of FAPESP and CAPES.

“Learn everything you can, anytime you can, from anyone you can, there will always come a time when you will be grateful you did.”

Sarah Caldwell

ABSTRACT

ANONI, L. G. **Comparison between Backprojection and Algebraic Methods for ultrasound tomography of concrete elements**. 2024. Dissertation (Master Program) – São Carlos School of Engineering, University of São Paulo, 2024.

Ultrasound tests have been widely applied for the evaluation of concrete elements, since they cause no damage to the inspected structure. One of its achievements in a simple analysis is the fast detection of non-homogeneities of the structure. The analysis of ultrasound results has gained complexity with the support of mathematical tools and computational data crossing, thus enabling the generation of tomographic images of internal sections of concrete. Among the several techniques addressed by the actual concrete tomography research are algebraic ones. Nevertheless, Backprojection method, widely used and consolidated in medical tomography, has been barely explored for concrete image reconstruction. This dissertation compares Backprojection, implemented in TUSom software, to recognized algebraic techniques. Additionally, methods such as Inverse Distance Weighting interpolation and interpolation of data using Artificial Neural Networks were employed to expand data and enhance image resolution. Velocity and attenuation tomography was generated from the time of flight of the ultrasonic wave and the variation in its amplitude through the reconstruction of numerically simulated and experimental concrete sections. As a primary result, it was possible to demonstrate the excellent performance of Backprojection, with and without the application of filters, in comparison to other evaluated image reconstruction techniques. Backprojection allowed for image generation even with a limited amount of data or enabled mesh enrichment to produce more accurate images. Although the interpolation techniques used reduced the image quality, IDW interpolation was successfully employed to generate images with only 12 readings. Furthermore, using the response of Backprojection as an initial guess for other techniques also proved to be a highly advantageous coupling method. With the results of this work, the aim is to have contributed to spreading the use of ultrasound tomography as a Non-Destructive Testing method for concrete structures.

Keywords: image reconstruction; concrete; ultrasound; ultrasound tomography; backprojection; algebraic methods.

RESUMO

ANONI, L. G. **Comparação entre Retroprojeção e Métodos Algébricos para Tomografia Ultrassônica de Elementos de Concreto**. 2024. Dissertação (Mestrado) – Escola de Engenharia de São Carlos, Universidade de São Paulo, São Carlos, 2024.

Com a vantagem de não danificar a estrutura inspecionada, o ensaio de ultrassom tem sido procurado para avaliação de elementos de concreto. Em uma análise simplificada, a detecção rápida de não homogeneidades da estrutura é uma das facilidades conquistadas com o ultrassom. Com o auxílio de ferramentas matemáticas e cruzamento de dados de forma computacional, a análise de resultados do ultrassom ganha complexidade e permite a geração de imagens tomográficas de seções internas do concreto. Diversas são as técnicas apresentadas nas pesquisas atuais para a tomografia do concreto, com um destaque para as técnicas algébricas. Apesar disso, uma técnica amplamente utilizada e consolidada na tomografia médica, a Retroprojeção, é pouco explorada para a reconstrução de imagens do concreto. Sendo assim, este trabalho teve como objetivo a comparação da técnica da Retroprojeção, implementada no software TUSom, com técnicas algébricas já reconhecidas. Além disso, técnicas como a interpolação IDW e a interpolação de dados com Redes Neurais Artificiais foram utilizadas na ampliação de dados como forma de promover melhorias na resolução das imagens. Tomografia de velocidade e de atenuação foi gerada a partir do tempo de voo da onda ultrassônica e da variação em sua amplitude por meio da reconstrução de seções de concreto simuladas numericamente e experimentais. Como resultado principal, foi possível mostrar o ótimo desempenho da Retroprojeção com e sem a aplicação de filtro em relação às demais técnicas de reconstrução de imagem avaliadas. A Retroprojeção permitiu a geração de imagens mesmo que com um número limitado de dados, ou ainda, permitiu o enriquecimento da malha garantindo a geração de imagens mais precisas. As técnicas de interpolação utilizadas reduziram a qualidade das imagens, porém a interpolação IDW foi utilizada com sucesso na geração de imagens com apenas 12 leituras. Ainda, o uso da resposta da Retroprojeção como estimativa inicial para as demais técnicas também se mostrou de grande vantagem. Com os satisfatórios resultados deste trabalho, espera-se ter contribuído para disseminar o uso da tomografia ultrassônica como Ensaio Não Destrutivo de estruturas de concreto.

Palavras-chave: reconstrução de imagens; concreto; ultrassom; tomografia ultrassônica; retroprojeção; reconstrução algébrica.

LIST OF FIGURES

LIST OF TABLES

LIST OF ABBREVIATIONS AND ACRONYMS

ABNT	Associação Brasileira de Normas Técnicas
Acc	Accuracy
ANN	Artificial Neural Network
ART	Algebraic Reconstruction Technique
ASCE	American Society of Civil Engineers
BP	Backprojection
DFT	Discrete Fourier Transform
EESC	Escola de Engenharia de São Carlos
FBP	Filtered Backprojection
FWI	Full Waveform Inversion
GA	Genetic Algorithm
ICC	Image Correlation Coefficient
IDW	Inverse Distance Weight
MBIR	Model-Based Reconstruction Technique
MLEM	Maximum Likelihood Expectation Maximization
MSE	Mean Squared Error
NDT	Non-Destructive Testing
Np	Negative Precision
OLS	Ordinary Least Squares
SAFT	Synthetic Aperture Focusing Tomography
SIRT	Simultaneous Iterative Reconstruction Technique
SR	Systematic Review
TOF	Time of Flight
USP	Universidade de São Paulo

CONTENTS

1 INTRODUCTION

Non-Destructive Testing (NDT) has gained prominence due to its advantages for inspections of concrete structures. It enables a periodic monitoring of concrete elements with no permanent damage to the structure and facilitates the prediction of maintenance or strengthening activities. Moreover, the number of possible tests has significantly increased in comparison to destructive tests, leading to more reliable results.

Ultrasound test is an NDT which uses transducers that emit and receive pulsed signals at above 20kHz frequencies. The well-directed gauging of the recorded data with a subsequent mathematical analysis enables the correlation of test results with the state of homogeneity of the evaluated concrete (ABNT NBR 8802:2019).

Although simplified data analysis is satisfactory, ultrasound test provides a large amount of information from each new measurement and a more complex treatment of the test data leads to more information on the analyzed structure. As an example, an ultrasound tomography is achieved from a proper mathematical equation with all collected data and a fast solution of the robust system of equations through computational tools that also enable image construction and visualization.

Tomographic images of concrete sections have already identified voids and damage in a structure and more recent attention has been devoted to new methodologies that use the technique with higher accuracy and speed (Kwon, Choi and Song, 2005; Soetomo *et al*., 2016; Zielińska and Rucka, 2020; Basu *et al.*, 2021; Haach and Juliani, 2014; Haach and Ramirez, 2016). However, the tomography of concrete structures is still at an early stage when compared to medical tomography. Studies of the techniques used in medical tomography can contribute to the transfer of knowledge between the two areas, thus improving the quality of tomography in concrete elements.

Backprojection (BP) is presented in such a context. One of the most classical techniques in medical image reconstruction, it is simple, enables the generation of quality images and offers, as a main advantage, effectiveness in localizing regions with properties that differ from the others (Wahab *et al.*, 2017; Mather and Baldock, 2003; Kim and Marmarelis, 2003; Hansen *et al.*, 2007; Cam, Villa and Anastasio, 2022; Wahab *et al.*, 2017; Kai Luo *et al.*, 2023). However, its use in ultrasound tomography of concrete has been barely explored.

This study focuses on Backprojection and evaluates it in comparison to algebraic techniques already recognized in concrete imaging.

1.1 Objectives

The main objective of this research is a comparison of Backprojection with algebraic reconstruction techniques for concrete tomography and its specific objectives include:

- Study of Backprojection and algebraic techniques;
- Implementation of the Backprojection and Filtered Backprojection codes in TUSom software;
- Adaptation of the conventional algorithm of Backprojection by a data interpolation tool towards increasing the number of projections of a studied element;
- Adaptation of the algorithm for the generation of velocity or attenuation tomograms;
- Comparative evaluation of the quality of the images generated by Backprojection and algebraic techniques from numerical and experimental models with artificial discontinuities; and
- Analysis of a possible coupling of the techniques.

1.2 Motivation

The maintenance costs of structures are inevitable for the preservation of their useful life. However, they can be minimized in function of the quickness with which a pathology is identified. Periodic inspection services contribute to preventive maintenance and reductions in expenses during the life cycle of a structure. Inspection with ultrasound testing has excelled due to the large amount of information that can be extracted from a signal. Moreover, it is an agile method and causes no damage to the structure.

A correct methodology of measurement and interpretation of ultrasound test results enables the generation of tomographic images, higher accuracy in the verification of the integrity of the medium, and more assertive decision-making regarding maintenance and repairs by ultrasound tomography.

The exploration of image reconstruction techniques has been extensively pursued, given the importance of visualizing the internal structure of concrete to identify damage and voids accurately. While Backprojection is a well-established method in medical studies, its application in engineering remains relatively unexplored. This study aims to fill this gap by comparing the Backprojection technique with established methods in concrete imaging, thereby expanding the possibilities of concrete tomography. The goal is to redefine Backprojection's

application in engineering, bringing fresh perspectives and broadening concrete imaging capabilities.

1.3 Text Organization

This dissertation is organized as follows: Chapter 1 encompasses introduction, general and specific objectives, motivation, and text organization; Chapter 2 addresses Background and Related Work supported by ultrasound tomography concepts, reconstruction methods, and TUSom software; Chapter 3 provides an overview of research conducted through a Systematic Review; Chapter 4 presents the Backprojection and Filtered Backprojection implementation method, IDW and ANN Interpolation implementation, inputs of image reconstruction algorithms, and numerical and experimental analysis methods; Chapter 5 reports results of performance of the image reconstruction techniques; and Chapter 6 is devoted to the highlights and considerations on the dissertation and to future work recommendations.

2 BACKGROUND AND RELATED WORK

This chapter addresses Background and the Related Work that supports this dissertation with concepts of ultrasound tests, ultrasound tomography, image reconstruction methods, inputs for the algorithms, and TUSom software.

2.1 Ultrasonic pulse velocity test

The basic principle of non-destructive testing by ultrasound, simplified by Andreucci (2011), is: “a sound wave reflects when incident on any bulkhead”. Therefore, an ultrasound wave traveling through an elastic medium will reflect in the same way, when incident on a discontinuity or internal flaw in the medium whose elastic properties and density influence the particular velocity of each wave (Malhotra; Carino, 2004).

Apart from changes in velocity, another wave property variation is attenuation. An ultrasound wave undergoes its path scattering and absorption effects, thus reducing its energy when traveling through any material. According to Andreucci (2011), the attenuation effect is seen in variations in wave amplitude between emitting and receiving transducers.

Several ultrasound applications have been developed due to the possibility of measuring the wave velocity or its attenuation. According to Brazilian Standard ABNT NBR 8802:2019, zones of inhomogeneity can be detected from the wave velocity difference calculated in the medium for regions of a structure with similar batch of concrete. Low velocities indicate lower concrete quality.

Despite highly contributing to the non-destructive analysis of concrete structures, the conventional technique is deficient, since it represents what occurs in a three-dimensional section in a one-dimensional graph (Giglio, 2021). In such a context, ultrasound tomography has arisen.

2.2 Ultrasound transmission tomography

According to Kak and Slaney (2001), a tomogram refers to the cross-sectional image of an object whose data have been collected from several different directions due to the transmission of a wave between transducers or reflection of the one emitted and received in a shield. Transmission tomography, the method applied for concrete beams and columns, is the

focus of this study. Reflection tomography is most common for structures whose faces cannot be accessed (e.g., pavements). A transmission ultrasound tomogram can be constructed according to techniques that organize data from different angles towards the visualization of the state of an object's section.

Tomographic image reconstruction methods originated when Radon (1917) first demonstrated an arbitrary function could be recovered from a set of projections at different angles (Mather; Baldock, 2003). The basic idea of Radon Transform is a mathematical representation of an object as a sum of data collected in several directions $g(s,\theta)$. Regarding ultrasound tomography, the sum can be represented by a sum of attenuations $\mu(x,y)$, or a sum of inverse of velocity, slowness $K(x,y)$, as in Equation (1). Figure 2.1 illustrates the basic principle of the Radon domain construction from data of parallel projections around an object.

$$g(s,\theta) = \int_{-\infty}^{\infty} \mu(x,y)dS = \int_{-\infty}^{\infty} K(x,y)dS \tag{1}$$

Figure 2.1 – Construction of Radon domain through the projection of rays onto an image domain

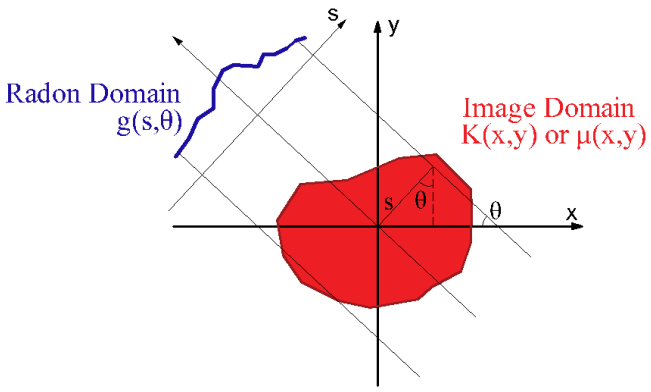

Source: the author.

2.2.1 Velocity tomography

Velocity tomography is the most used tomographic approach for concrete structures due to the easiness of obtaining Time of Flight (TOF) in experimental ultrasound measures. The TOF of an ultrasound wave is the main parameter for the acquisition of velocity tomograms based on kinematics equations (Camassa *et al.*, 2020). A geometrical determination of the path (ΔS_{ij}) of a wave among transducers, or its determination by a ray-tracing algorithm enable the calculation of its velocity (Equation (2)). The inverse of velocity (V_i), called slowness (K_i), is frequently used for facilitating the construction of a problem, as claimed by Radon (Equation

1). Equation 3 provides the manipulated problem so that TOF (Δt_j) data can be dealt with for a discrete number of measurements.

$$V = \frac{\Delta S}{\Delta t} \tag{2}$$

$$\Delta t_j = \sum \Delta S_{ij} K_i \tag{3}$$

The number of measurements creates a system of linear equations that can be expressed in a matrix form (see Equation (4)) and comprises the TOF of each measurement $\{\Delta t_j\}$, the sensitivy matrix $[\Delta S_{ij}]$ which represents the path of the wave on the mesh, and the interest slowness vector $\{K_i\}$.

$$\{\Delta t_j\} = [\Delta S_{ij}]\{K_i\} \tag{4}$$

The solution of the system provides the distribution of the wave slowness, or the wave velocity in a section. As addressed elsewhere, high velocities are correlated to the high stiffness of the concrete. Another significant factor affecting velocity is the presence of voids. Ultrasound waves travel along the fastest paths, and since their velocity is faster in concrete than in air, they must navigate around any voids present. Therefore, with no awareness of the voids presence and considering a straight path for wave propagation, the velocity calculated usually decreases because of the longer TOF. The tomogram as a velocity distribution map provides a representation of the presence of internal damaged areas.

2.2.2 Attenuation tomography

Attenuation tomography is based on the amplitude decay of a wave and has been successfully applied to medical tomography. However, it has not been widely used in concrete structure evaluations due to experimental challenges such as coupling conditions between the transducers and the surface of the structure and pressure exerted on the transducers by the operator, thus hampering the evaluation of the received amplitude, an important parameter for the generation of attenuation tomogram (Camassa *et al.*, 2020).

The equation for the attenuation of ultrasonic waves in a medium is typically expressed by the Beer-Lambert law (see Equation (5)), which relates the wave intensity I to the distance traveled ΔS_{ij} and the attenuation coefficient of the medium μ_i (Chai *et al.*, 2011). The wave intensity is directly proportional to the square of the amplitude (A), and the manipulations of

the formulations are illustrated in Equations (6) to (8). Note the structure of Equation (8) is similar to that of Equation (3); consequently, the algorithm that deals with TOF can also deal with the amplitude variation (A_0 and A_j are emitted and received amplitudes), enabling the generation of two different tomographic maps (velocity and attenuation) with a single signal. The system then has the interest vector $\{K_i\}$ as the attenuation coefficient and $\{\Delta t_j\}$ represents the amplitude decay in Equation (4).

$$I_j = I_0 e^{-\sum \mu_i \Delta S_{ij}} \rightarrow {A_j}^2 = {A_0}^2 e^{-\sum \mu_i \Delta S_{ij}} \tag{5}$$

$$\frac{{A_j}^2}{{A_0}^2} = e^{-\sum \mu_i \Delta S_{ij}} \tag{6}$$

$$ln\left(\frac{{A_j}^2}{{A_0}^2}\right) = ln\left(e^{(-\sum \mu_i \Delta S_{ij})}\right) \tag{7}$$

$$ln\left(\frac{{A_0}^2}{{A_j}^2}\right) = \sum \Delta S_{ij} \mu_i \tag{8}$$

Camassa *et al.* (2020) reported several attenuation phenomena such as material and geometrical attenuation, wave dispersion, scattering, diffraction due to obstacles and voids, characteristic of the receiver, among others that reduce the amplitude of a wave. High attenuation in a section indicates damaged regions. The solution of the system generates an attenuation distribution map of the section and enables concrete internal state inspection.

2.3 Image reconstruction techniques

Image reconstruction for ultrasound tomography is a complex problem due to the number of possible measurements in a test and the computational mesh. In most cases, those factors create a non-square sensitivity matrix $[\Delta S_{ij}]$ which makes it non-invertible, leading to an ill-posed problem of no unique solution for $\{K_i\}$.

Inversion algorithms are applied for solving the aforementioned problem caused by the sensitivity matrix and the measurements of TOF or amplitude decay. Hou *et al.* (2022) proposed inversion algorithms for transmission tomography as projection, algebraic, or regularization ones. Projection algorithms include Backprojection, Fourier transform, Backprojection filtering, and Filtered Backprojection (Asl, 2013), whereas Algebraic methods encompass Algebraic Reconstruction Technique (ART), Simultaneous Iterative Reconstruction Technique

(SIRT), and Ordinary Least Squares (OLS). The regularization methods found in the literature are Tikhonov and L1-regularization.

Figure 2.2 shows the specific image reconstruction techniques for transmission tomography addressed. Backprojection and Algebraic Methods are described in what follows. Regularization and reflection tomography techniques are not in the scope of this research; therefore, some of them will be briefly discussed in subsection 2.3.3.

Figure 2.2 – Image reconstruction techniques studied in this research.

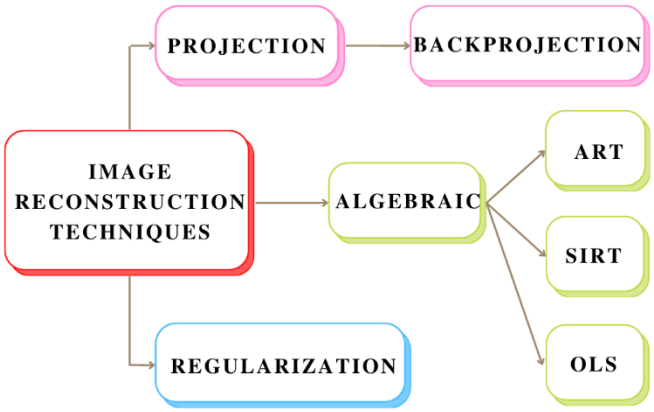

Source: the author.

2.3.1 Backprojection and Filtered Backprojection

Backprojection is the most used and best established technique in medical tomography (Mather; Baldock, 2003). According to Charamba (2013), it redistributes the values of the sum of densities of projections at each point belonging to a trajectory line. The algorithm is the reverse of the projection operation that provided data, hence, the inverse of Radon Transform presented by Kak and Slaney (2001).

Each measurement with the ultrasound test produces results that are projected to the Radon domain. The back-projection of Radon data results in an image of the internal structure of the element. The concept can be understood through the discretization of the image on a mesh and application of Radon Transform and Backprojection, respectively. To contextualize the example, consider Figure 2.3a as a concrete prism with damage in the center, resulting in variations in measurements. The numbers in the figure could correspond to velocity or attenuation coefficients, which are assumed to be constant in each element of the mesh.

Figure 2.3 – Projections at 0 and 90-degree angles of the assumed image (a), projections with the unknown image (b), first back projection (c), and second back projection (d)

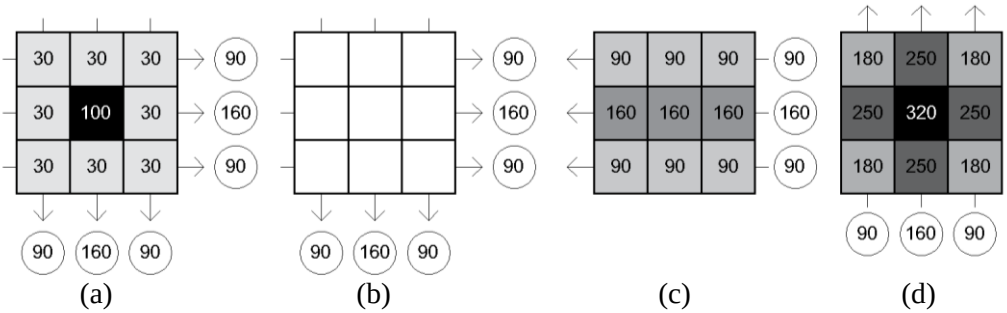

Source: the author.

The information projected in Figure 2.3b represents the data acquired from the ultrasound test, which is a summation of internal information contained within the elements. Backprojection technique subsequently rearranges the ultrasound test data within the image domain, revealing the damage. Figure 2.3c and 2.3d display the first and second back-projections of the data, leading to an image similar to the real one, represented by Figure 2.3a. More parallel projections for each angle and a greater number of angles are expected to provide images closer to the real ones, as in Figure 2.4.

Figure 2.4 – Arrangement with a greater number of projections for a greater number of angles

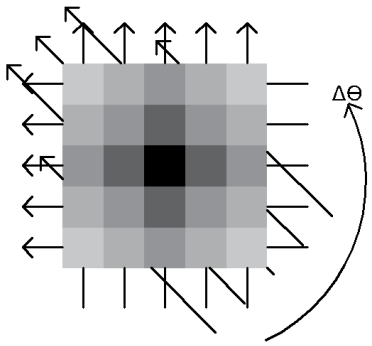

Source: the author.

To enhance the generation of Backprojection images, filtering is widely employed, either in the time or frequency domain. The filtering in frequency domain is a common choice, requiring a 2D Fourier Transform. Within the frequency domain, various filters can be applied to the image, including low-pass, high-pass, and band-pass filters (Vieira, 2019). Subsequently, the inverse Fourier Transform is employed to restore the image, leading to improvement through noise reduction. Another applied filtering method is called convolution, which operates

in the time domain. In this method, a function, often called a kernel or mask, is systematically moved across the input data. This modified technique, called Filtered Backprojection (FBP), allows for targeted modifications and enhancements to the image, contributing to a refined output.

A concern on the use of BP or FBP algorithms for ultrasound tomography of concrete raised by Kwon, Choi and Song (2005) is the wave trajectory is not linear within a heterogeneous medium, which does not match the BP idea of parallel and linear projections. The problem can be currently circumvented by ray-tracing optimization techniques, as reported by Perlin and Pinto (2019). Nevertheless, several authors have assumed straight-line propagation and achieved acceptable results in damage detection in concrete elements (Perlin; Pinto, 2019). The aim of this work is to check the efficiency of the application of Backprojection for the ultrasound tomography of concrete by simple geometrical straight-line projection calculation implemented on TUSom.

2.3.2 Algebraic Methods

According to Kak and Slaney (2001), the methodology related to algebraic algorithms consists of the definition of a mesh superimposed on an object to be imaged with the assembly of a system of equations that, when solved, returns to the tomographic image. The advantage of the methods is their good performance in severely incomplete data problems such as limited angle tomography. However, Gopi (2014) claimed the techniques are susceptible to noise and the reconstruction process is slow.

The algebraic methods presented in this study are ART, SIRT, and OLS, of which the first and second are iterative and OLS finds a solution by minimizing an error, as described in what follows.

ART is the simplest and starts defining an initial guess of K_i^m (slowness or attenuation coefficient vector), which is projected onto the first through the last equation of the system. K_i^{m+1} is actualized by Equation (9) for each projection in different equations (Giglio, 2021). The iteration ends when all equations have been projected by ΔK_i (Equation (10)).

$$K_i^{m+1} = K_i^m + \Delta K_i \tag{9}$$

$$\Delta K_i = \frac{\left(K_i^{(m)} \Delta S_{ij} - \Delta t_j\right)}{\Delta S_{ij} \Delta S_{ij}} \Delta S_{ij} \tag{10}$$

SIRT usually converges into better images than those produced by ART. However, the computational cost is higher due to the actualization process of K_i^{m+1}. Similarly to ART, it works with an initial guess of K_i^m and its actualization. However, the same K_i^m is used in all equations, which calculate the actualized value. Only at the end of each iteration, vector values K_i^{m+1} are actualized by the average of the corrected one (ΔK_i) (Kak; Slaney, 2001). The number of measured data is n, as shown in Equation (11).

$$K_i^{m+1} = K_i^m + \frac{\Delta K_i}{n} \tag{11}$$

OLS minimizes the sum of squared errors (residual) and the residual is calculated as the difference between experimental $\Delta t_{exp,j}$ and theoretical $\Delta t_{teo,j}$ measurements (Haach, 2017). The theoretical measurements are calculated by Equation 4 according to an initial guess of K_i^m. Equation (12) provides the residual K_i. can be estimated by imposing the first derivative of the residual is zero.

$$r^2 = \sum_i \left(\Delta t_{exp,j} - \Delta t_{teo,j}\right)^2 = \sum_i \left(\Delta t_{exp,j} - \Delta S_{ij} \cdot K_i\right)^2 \tag{12}$$

2.3.3 Other important methods

Synthetic Aperture Focusing Tomography (SAFT), a reflection ultrasound tomography, is among the image reconstruction techniques most widely applied to the ultrasound tomography of concrete. Also called delay and sum technique, it integrates signal amplitudes under the assumption the acoustic velocity is constant (Almansouri *et al.*, 2015). According to Hoegh, Khazanovich, and Yu (2012), the method operates on the principle that changes in acoustic impedance (affected by material stiffness changes) will result in high-intensity reflections associated with the location of the anomaly. Furthermore, as noted by Choi, Bittner, and Popovics (2016), this technique becomes necessary due to practical limitations in civil infrastructure, such as the inability to access both sides of an element.

Although SAFT works well for thin concrete specimens, some problems arise for thick-concrete images (Almansouri *et al.*, 2016). Model-Based Reconstruction Technique (MBIR), a powerful probabilistic tool based on probabilistic models, has, therefore, drawn the interest of

current research, since it is highly effective for the reconstruction of inverse problems such as reflection tomography.

In addition to velocity and attenuation tomography, the so-called Full Waveform Inversion (FWI), a high-resolution imaging technique, aims at extracting as much information as possible from recorded waveforms. Kordjazi, Coe and Afanasiev *et al.* (2020) showed it works better than traditional tomography, but it has a higher computational cost. The calculation process was developed in the field of geophysics towards an accurate sound velocity image (Suzuki *et al.*, 2019). The approach involves solving 2D elastic shear-wave equations in the time domain for forward modeling, generating synthetic waveforms.

Regularization techniques are used either in their proper form, or combined with others as a form of optimization, and aim at producing reliable estimates of a solution to ill-posed problems in presence of noisy data (Hou *et al.*, 2022). Tikhonov and L1-regularization are the most used and their convergence depends on a regularization parameter choice.

2.4 TUSom Software

TUSom was developed in Lazarus programming platform by Prof. Dr. Vladimir Guilherme Haach and master students towards handling ultrasonic test data. Its tomographic simulation interface enables image reconstruction. The program encompasses OLS, ART, and SIRT techniques to generate velocity tomography. For image reconstruction, the first step is to define the geometry and measurement trajectories in the main interface (Figure 2.5a). Then, a file with the respective time of flight or amplitude decay of each measurement is inserted in "Analysis 4 - Tomography" (Figure 2.5b). Finally, one of the available image reconstruction techniques is chosen for obtaining an image. Backprojection and Filtered Backprojection are the new tomographic techniques options in the software.

Figure 2.5 – TUSom initial interface, a) sample configuration, and b) available analysis

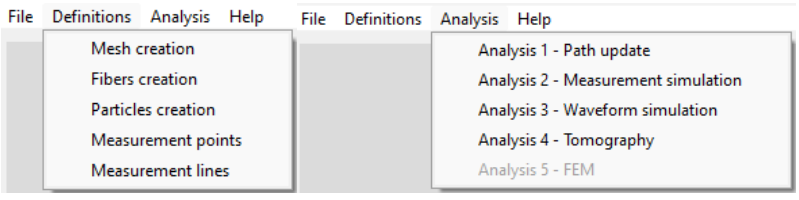

(a) (b)

Source: the author.

Algebraic image reconstruction algorithms in TUSom solve the inverse problem and find K_i considering the imposed mesh and trajectory of the wave. Each equation of the system to be solved represents a datum measured in a path, as shown in Figure 2.6. Equation (13) shows the system for path "$j = 1$" across elements "$i = 1\ to\ n$".

Figure 2.6 – Wave travel and part of the path traveled in one mesh element

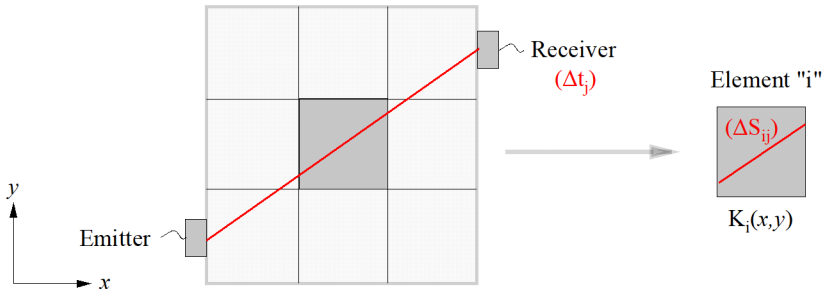

Source: the author.

$$\Delta t_1 = \Delta S_{11} K_1 + \Delta S_{21} K_2 + \cdots + \Delta S_{n1} K_n \tag{13}$$

The field of interest, slowness or attenuation, is calculated in TUSom for each element node of the mesh. Haach (2017) introduced the general formulation according to which the interpolation of the slowness field is assumed linear along the element. For a square element, the slowness field can be written as a polynomial in Equation (14), a function of x and y coordinates of a quadrangular element, as in the finite element method. It is then rearranged in a matrix form in Equation (15).

$$K(x,y) = \alpha_1 + \alpha_2 \mathrm{x} + \alpha_3 \mathrm{y} + \alpha_4 \mathrm{xy} \tag{14}$$

$$K(x,y) = \{1 \quad x \quad y \quad xy\} \begin{Bmatrix} \alpha_1 \\ \alpha_2 \\ \alpha_3 \\ \alpha_4 \end{Bmatrix} = [p(x,y)]^T \{\alpha\} \tag{15}$$

α parameters are defined from the nodal slowness by Equation (16) which, replaced in Equation (15), enables the slowness field to be written as a function of nodal slowness (Equation (17)). Therefore, four shape functions $N(x,y)$ appear, i.e., one for each node of the quadrangular element (Equation (18)).

$$\begin{Bmatrix} K_1 \\ K_2 \\ K_3 \\ K_4 \end{Bmatrix} = \begin{bmatrix} 1 & x_1 & y_1 & x_1y_1 \\ 1 & x_2 & y_2 & x_2y_2 \\ 1 & x_3 & y_3 & x_3y_3 \\ 1 & x_4 & y_4 & x_4y_4 \end{bmatrix} \begin{Bmatrix} \alpha_1 \\ \alpha_2 \\ \alpha_3 \\ \alpha_4 \end{Bmatrix} \rightarrow \{K\} = [A]\{\alpha\} \rightarrow \{\alpha\} = [A]^{-1}\{K\} \quad (16)$$

$$K(x,y) = [p(x,y)]^T[A]^{-1}\{K\} \rightarrow K(x,y) = [N(x,y)]\{K\} \quad (17)$$

$$[N(x,y)] = [N_1(x,y) \quad N_2(x,y) \quad N_3(x,y) \quad N_4(x,y)] \quad (18)$$

Velocity and slowness are opposite magnitudes, thus leading to the obtaining of nodal velocity. Through a linear interpolation of such a velocity, TUSom generates a velocity map of the transversal section and displays the internal state of the structure.

In addition to defining linear paths between transducers for the construction of sensitivity matrix ΔS_{ij}, TUSom has a path update tool that works according to the concept that an ultrasound wave travels the fastest path between transducers, which, depending on the heterogeneity of the medium, does not always lead to a linear trajectory. The tool was implemented by Giglio (2021) and updates ΔS_{ij} according to updated paths. Since ΔS_{ij} is an input for BP and FBP algorithm, them response can also be evaluated with updated paths.

Time Simulation Interface, another feature of TUSom, estimates TOF from a predetermined velocity map (Figure 2.5b, Analysis 2). Therefore, all numerical comparative analyses of techniques are performed in TUSom.

2.5 Chapter overview

This chapter introduced the main concepts related to ultrasound tomography and image reconstruction techniques. The functionalities of TUSom software have been summarized towards the understanding of its adoption for all numerical simulation and its changes during this work.

3 SYSTEMATIC REVIEW (SR)

A systematic review is a rigorous method of literature search for all relevant scientific knowledge in a given area through planning, data collection, and critical analysis. Therefore, a document including protocol, review conduct, data extraction, and data analysis has been produced towards contributing to the planning, action, and summarization of the SR.

3.1 Methods

The methodology of the literature research was divided into three steps, namely planning, action, and summarization, described in what follows.

3.1.1 Planning

Towards an efficient data flow, the objectives, questions to be answered, and other variables of interest were discussed for the creation of a Research Protocol, shown in Table 3.1.

Table 3.1 – Research questions and basic script

Research control	The general ideas about the topic that supported the questions of this SR originated from the reading of dissertations and papers recommended by the supervisor of this research.
Research question	What is the relevance of Backprojection for ultrasound tomography in comparison to the other image reconstruction techniques? What is the overview of techniques for concrete tomography?
Types of documents analyzed	Papers that present techniques of image reconstruction with ultrasound data in their methodology.
Results	State-of-the-art of ultrasound image reconstruction techniques, with a focus on Backprojection in civil engineering.
Applications	Finding of gaps and opportunities for the application of efficient techniques, specially Backprojection, from other areas of knowledge within the field of civil engineering.

Source: the author.

The next step was the selection of research databases available on the web, preferably in scientific ones in the area. Initial keywords tomography, image reconstruction, concrete, Backprojection, and ultrasound were defined towards the construction of a search string according to the analysis of the search control data.

Such a construction was iterative, and the words were combined through modifications in the commands until the results had been satisfactory. The search with the use of all words ((Tomography OR "image reconstruction") AND concrete AND Backprojection AND ultrasound) returned no results.

A new search was then performed modifying the initial string to ((Tomography OR "image reconstruction") AND concrete AND Backprojection), returning 5 results focused on image reconstruction with X-ray data. Since the research topic involves specifically the use of ultrasound, term ultrasound was reincluded and "AND" was changed to "OR" between terms concrete and Backprojection.

After the last search, some recognized papers in the field had not been selected. Therefore, “back projection” and “ultrasonic”, a synonym for ultrasound, were included in the string, which was then defined. Table 3.2 shows the variables.

Table 3.2 – Variables of the systematic review

Keywords	Tomography, image reconstruction, concrete, backprojection, ultrasound, back projection, ultrasonic
Databases	Web of Science, Science Direct, ASCE
Criteria for choosing databases	Exportation of files to EndNote or BibTex format Finding of articles related to civil engineering
Search string: Web of Science	ALL= (Tomography OR "image reconstruction") AND (concrete OR backprojection OR back projection) AND (ultrasound OR ultrasonic)
Search string: Science Direct	TITLE-ABS-KEY (Tomography OR "image reconstruction") AND (concrete OR backprojection OR back projection) AND (ultrasound OR ultrasonic)
Search string: ASCE	(Tomography OR "image reconstruction") AND (concrete OR backprojection OR back projection) AND (ultrasound OR ultrasonic)
Period considered	All
Filters considered	None
Search date	25/10/2022 (reviewed in 06/01/2024)

Source: the author.

After the definition of the search parameters, the strings were submitted to the databases and all papers on the topic were exported to EndNote. Appropriate inclusion and exclusion criteria were then established towards defining papers to be incorporated into the systematic review and those to be excluded. This step is important for avoiding the reading of papers that do not match the research objectives. In what follows are the exclusion criteria:

a. Title and/or abstract do not address image reconstruction;
b. Article published before 2012 with no citation;
c. Article that contains some image reconstruction technique, but does not present it as a methodology of the study;
d. Documents whose viewing is unavailable even with student license;
e. Articles on photoacoustic or thermoacoustic tomography (outside the scope of the paper); and
f. Articles in languages other than English.

3.1.2 Action

After the papers have been exported to EndNote software, the program identifies and deletes those duplicated, and articles can be viewed per number of citations, which helps the understanding of the relevance of each document.

The exclusion criteria were applied in two steps. Initially, titles and keywords were reviewed, followed by reading the abstract for a smaller subset of papers. If a document met any of the exclusion criteria during either step, it was excluded. Conversely, if it satisfied all requirements, it was accepted and subsequently moved to the summarization process. In the event of relevant papers being published during the conclusion of this dissertation, they would be accepted and summarized to contribute additional data to this Systematic Review (SR). The final check was conducted on 06/01/2024.

3.1.3 Summarization

In this step, the paper was subjected to an in-depth analysis. The information considered relevant to the research was recorded according to the questions initially prepared (Table 1). In the present case, the aim was to know the image reconstruction technique presented with the use of ultrasound data, the way the method works, its experimental application and area of

interest of the article, and other information that helped identify the current scenario of ultrasound tomography. A data extraction form was designed towards assisting in the process (Table 3.3).

Table 3.3 – Data extraction form

Title	Write the title of the paper
Authors	Write the authors of the paper
Year	Write the year of paper publication
Personal abstract	Write a summary of the article
Image reconstruction technique	Write the name of the technique
Short explanation of the technique	Write about the technique
Comparative analysis?	Yes or No
What ultrasound data are applied?	Time of flight, amplitude decay, or other
Area of interest	Civil Engineering, Computer Science, Medicine or Others

Source: the author.

After the reading and summarization of the selected papers, a discussion on bibliography was prepared. A quantitative analysis defined the graphics and numbers of the current scenario of ultrasound tomography techniques in civil engineering and the possibility of using Backprojection images for a non-destructive evaluation of concrete.

3.2 Results

The initial search in the three databases resulted in 726 documents, reduced to 66 after the application of the exclusion criteria. Figure 3.1 illustrates the steps and the final number of documents.

6 out of the total number of documents were duplicate ones, which were found and excluded with the help of EndNote. The total of partially read articles (title, abstract, and keywords) was then reduced to 720, which, after reading, were classified according to each criterion as folders "a" to "g". This study also involved the preparation of a synthesis of each document and a brief discussion on their contents.

After a qualitative synthesis of the articles, a quantitative analysis was elaborated. The first point highlighted was the fact that 66 of the 720 documents surveyed dealt with image

reconstruction as a methodology, i.e., 9.17% of the papers were within the scope of this research.

Figure 3.1 – Filtering steps of the systematic review

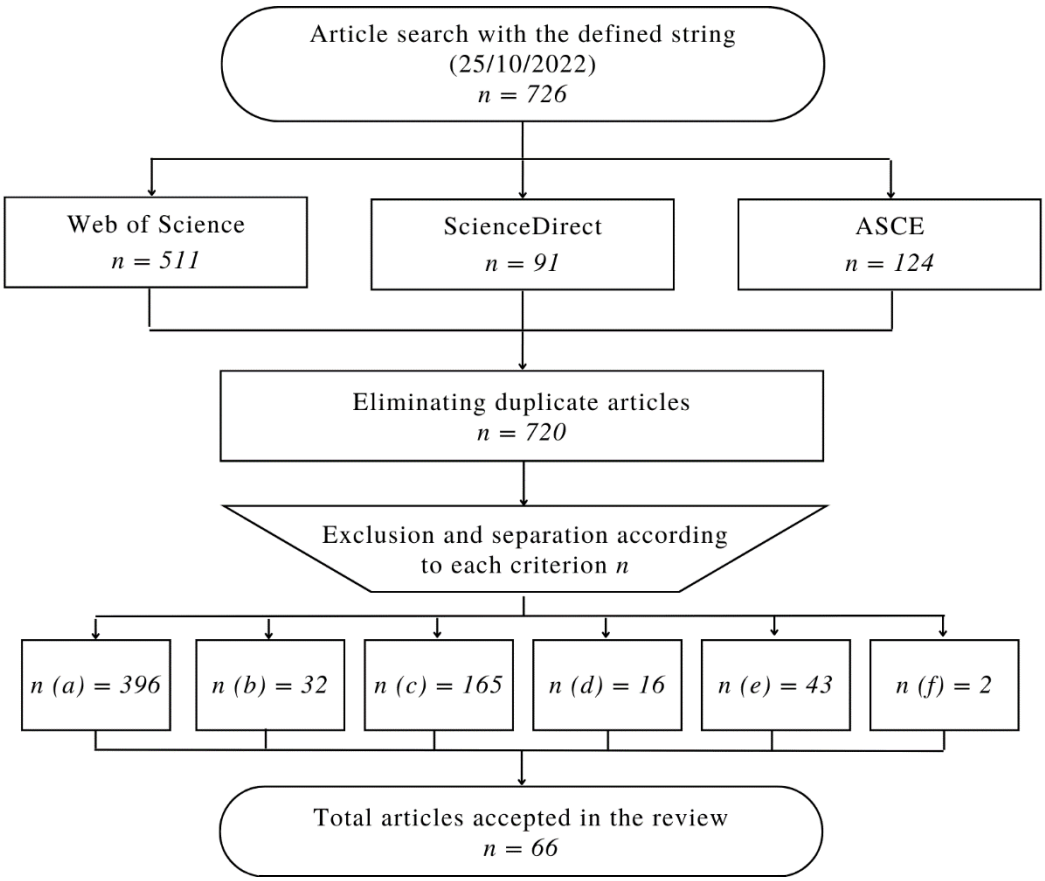

Source: the author.

3.2.1 Backprojection and other image reconstruction methods

The data were analyzed and an overview of the range of image reconstruction techniques used in ultrasound tomography was provided. Although an old method, Backprojection was applied in the analyzed studies (see Figure 3.2) and has been largely adopted in ultrasound tomography. Its both consolidation and easiness of application are noticeable. The studies were divided into two research approaches, i.e., search for improvements in Backprojection and their use as a form of comparison for newly developed methods.

Some relevant topics for the first approach are BP combined with neural networks (Perdios *et al.* (2022) and Abu Anas *et al*. (2019)), a novel method for the construction of a sensitivity matrix (Li *et al.* (2019)), improvements, in spatial resolution by iterative techniques (Rahiman *et al.* (2012) and Li and Chu (2013)), and wave-based technique using more ultrasound data

(Molchanova *et al.* (2022)). The second approach encompasses new image reconstruction techniques compared to BP (Suzuki (2019), Bao *et al.* (2021), and Espinosa *et al.* (2020)).

Considered a relevant Backprojection improvement, Filtered Backprojection (FBP) is derived from an enhancement in the quality of the image generated by simple Backprojection. The filters remove frequency bands from the ultrasound signal and artifacts are eliminated so that the image resolution is improved. A Wahab *et al.* (2017) compared BP and FBP and Mather and Baldock (2003), Kim and Marmarelis (2003), Hansen *et al.* (2007), Cam, Villa and Anastasio (2022), and Wahab *et al.* (2017) discussed FBP. Kai Luo *et al.* (2023) compared several filters towards improving the performance of FBP.

Figure 3.2 – Image reconstruction techniques found in the SR and BP publications over the years

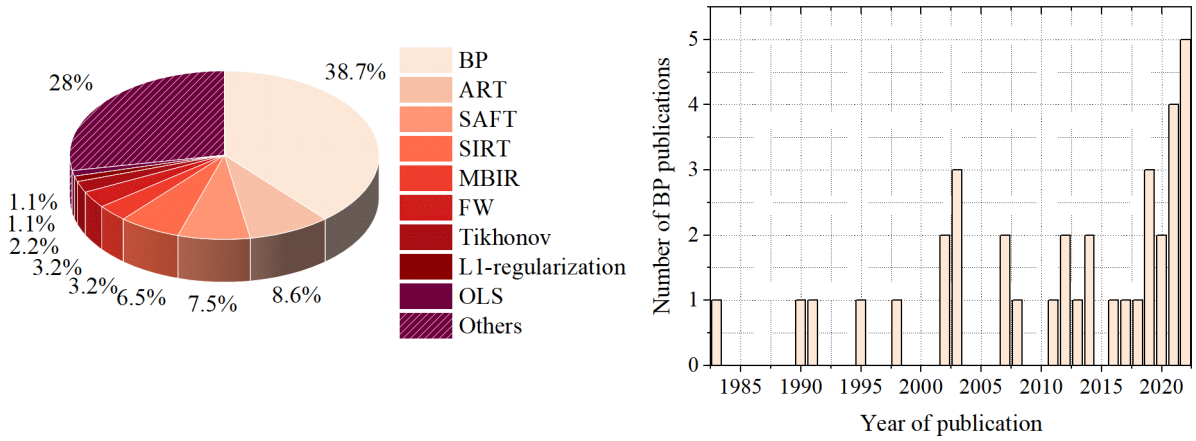

Source: the author.

Apart from BP, several other reconstruction techniques were detected among the data compiled in the SR (see Table 3.4). Furthermore, the percentage of methods inserted within the "other" sector must be highlighted.

The SR revealed several new methods such as the Maximum Likelihood Expectation Maximization (MLEM) algorithm used by Fan *et al.* (2017), Perez-Liva (2020), and Fan and Zhu (2018) and Reverse Time Migration demonstrated by Asadollahi and Khazanovich (2018). Hybrid reconstructions are presented in Rahiman *et al.* (2012) and other iterative methods are discussed mathematically by Aggelis *et al.* (2009), Fang and Li (2009), and Bao *et al.* (2021). All such studies have pointed to the emergence of other techniques.

Table 3.4 – Where to find some image reconstruction techniques information

ART	Yu *et al.* (2021), Basu *et al.* (2021), Haach and Juliani (2014), Zielińska and Rucka (2020), and Kwon, Choi and Song (2005)
SAFT	Schmitz *et al.* (1986), Hoegh, Khazanovich, and Yu (2011, 2012), Hoegh *et al.* (2012), Hoegh and Khazanovich (2015), Almansouri *et al.* (2015), Tseng, Chang and Wang (2018), Ezell *et al.* (2019), and Ghosh *et al.* (2020)
SIRT	Haach and Juliani (2014), Haach and Ramirez (2016), Chai *et al.* (2011), and Niu *et al*. (2021)
MBIR	Almansouri *et al*. (2015), Almansouri *et al*. (2016), and Ezell *et al*. (2019)
FW	Kordjazi, Coe and Afanasiev (2020), Suzuki *et al.* (2019), and Leach *et al*. (2002)
Tikhonov and L1 regularizations	Zhang, Tan and Dong (2020), Hou *et al.* (2022), Zhu *et al.* (2015), and Fang and Li (2009)

Source: the author.

3.2.2 Evolution of image reconstruction methods

The data were organized towards the understanding of the distribution of publications over time (see Figure 3.3). The increase in the number of publications that discuss reconstruction techniques for ultrasound tomography from the year 1983 (with greater interest from the year 2000) is notable. Papers produced before 2000 focused on mathematical discussions on the theme in the computer science area (Hoyle, 1991; Natterer; Wubbeling, 1995; Oristaglio, 1983; Schmitz, 1986; Witten; King, 1990), whereas current research has expanded to the most diverse areas of knowledge.

Figure 3.3 – All 66 documents distributed over the years and analyzed in the SR

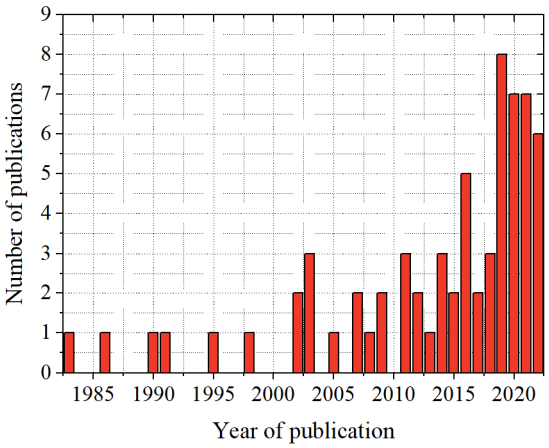

Source: the author.

Due to the advantage of ultrasound tomography as an alternative to X-ray imaging, mainly in relation to its non-ionizing nature and high information content of the measured signals, a concern on improvements in its resolution in medicine has arisen (Peterlik *et al.*, 2008). In comparison to X-rays, the ultrasound accuracy is much lower, i.e., from 0.03 mm to 2 mm (Leach *et al.*, 2002). Therefore, some authors have discussed techniques that can improve it, as shown in Figure 3.4.

Figure 3.4 – Techniques discussed towards ultrasound imaging improvements

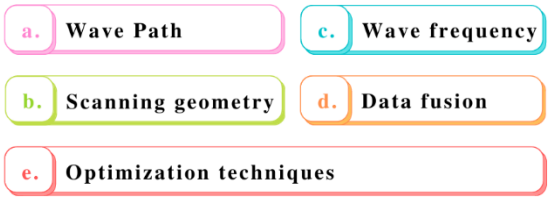

Source: the author.

a. Wave path

New research based on the concern of the wave refraction and consequent deflection of the ray has spread, dealing with the usual and incorrect definition of straight wave path. Ray-tracing methods calculate the wave path and provide the fastest travel path for each ultrasound reading. An initial image is reconstructed assuming straight paths and the algorithm then calculates the paths based on that image, which is used to update the previously calculated paths. (Kwon; Choi; Song, 2005). Anastasio, Kupinski and Pan (1998), Leach *et al*. (2002), Aggarwal and Vasu (2003), and Schröder and Schuster (2016) were concerned with the wave path update in their research.

Zielińska and Rucka (2020) calculated velocity maps using both straight-line paths and curved rays determined by the hybrid network theory/ray bending method. Perez-Liva *et al*. (2020) used quadratic Bézier polynomials to reproduce the paths and Perlin and Pinto (2019) adopted Dijkstra's algorithm, yielding the fastest travel path for each ultrasound reading.

According to Mather and Baldock (2003), if propagation occurs in a non-dispersive material of minimal variations in acoustic impedance, the errors in the reconstructed image are small. Therefore, wood is a material of concern in civil engineering due to property differences between growth rings. Espinosa *et al.* (2020) illustrated the highly positive effect of considering a wave updated path in wood inspection.

b. Scanning geometry

The choice of measurement geometry depends on practical requirements. Some studies have focused on redefinitions of conventional algorithms so that they adapt to new measurement geometries. The three most usual configurations are linear, circular, and spherical. Mensah and Ferriere (2002) were concerned with a numerical development of the techniques that take into account the scanning geometry used in practice.

Another concern is the need to adapt algorithms when the measurement geometry has a limited angle. Tang, Azuma and Sakuma (2019) proposed a new imaging method that enables the use of fewer ultrasound data for the reconstruction of images with high spatial resolution, and Li *et al.* (2021) designed a novel configuration of transducers towards improving ultrasound imaging with a limited diffusion angle. The rearrangement of transducers was also addressed by Hoyle *et al*. (2021).

c. Wave frequency

An important variable in ultrasound testing is the excitation frequency of the waves. Aggelis *et al*. (2011), Chen, Shih and Huang (2011), Huang and Chen (2014), Haach and Ramírez (2016), and Kwon, Joh and Chin (2021) claimed higher frequencies are, in general, more effective.

In civil engineering, tests performed with 250 kHz transducers returned better images than those with 54 kHz transducers (Haach; Ramirez, 2016); however, the attenuation was increased when the frequency increased (Huang; Chen, 2014).

d. Data fusion

Some papers described ways to extract more data from an ultrasound test and improve a reconstructed image. The FW image reconstruction technique can be considered a data fusion one - Kordjazi, Coe and Afanasiev (2020) provide a brief review of its principles.

Niu *et al*. (2021) combined ultrasound data based on Bayesian theory (probability and statistics) to generate images and evaluate the internal defects of concrete structures. In another interpretation, Hou *et al.* (2022) promoted a fusion of images combining two or more images with wavelet fusion into a single image, thus retaining important features from each one.

e. Optimization techniques

According to Niu *et al.* (2021), optimization methods such as artificial neural networks and genetic algorithms have been employed in image reconstruction techniques. As an example,

Bao *et al*. (2021) used an optimized algorithm, since it can greatly reduce irrelevant noise in images.

Neural networks have been employed in most studies. Abu Anas *et al*. (2019) claimed two major approaches, namely end-to-end deep learning and deep learning as an artifact reconstruction, have been adopted. According to the former, raw projection data are taken as input and the reconstructed image is provided as their output. The second approach relies on conventional reconstruction strategies followed by a deep neural network for artifact reduction. Almansouri *et al.* (2018), Perdios *et al*. (2022) and Cam, Villa, and Anastasio (2022) also used the benefits of neural networks in their research.

Wang *et al.* (2019) applied and discussed a genetic algorithm, reporting it offers faster and higher-precision combinatorial optimization calculation for inversion problems. In addition, Wang *et al.* (2022) and Yu *et al.* (2021) pointed out compressed sensing is an optimization method and a new theoretical framework for information acquisition and processing based on matrix analysis.

3.2.3 Image reconstruction methods in Civil Engineering

Among the papers accepted in the review, 45.5% are from the civil engineering area. Advancements in research on ultrasound tomography in civil engineering are more recent, as shown in Figure 3.5. The first register of the use of ultrasound image reconstruction techniques for concrete evaluation is found in Kwon, Choi, and Song (2005), who implemented ART algorithms for concrete imaging.

Figure 3.5 – Classification of articles according to the subject area and distribution of civil engineering papers over the years

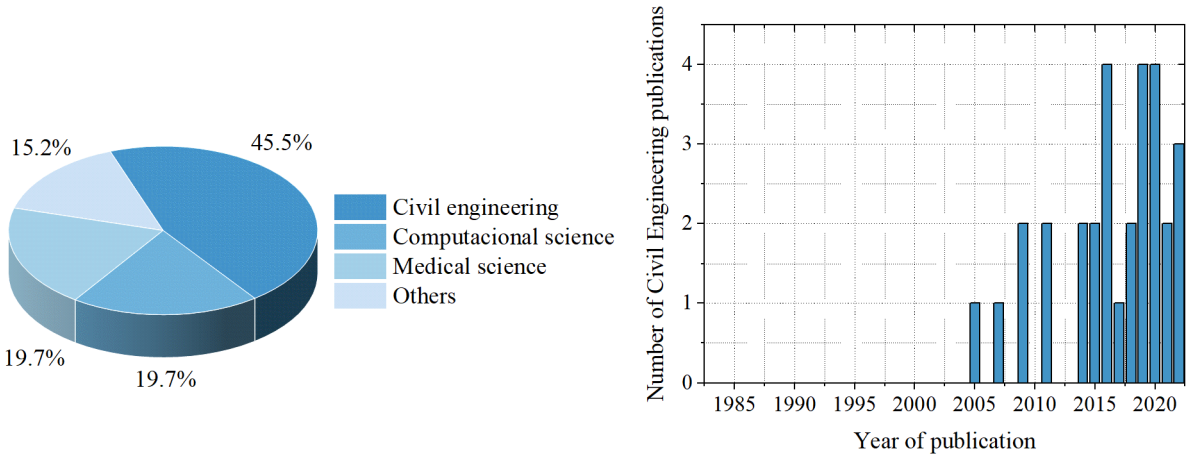

Source: the author.

Image reconstruction techniques are presented in a different scenario in civil engineering. Backprojection is one of the least applied techniques, whereas ART is the most used, as shown in Figure 3.6. Espinosa *et al.* (2020) adopted BP for wood imaging and Yanagida *et al.* (2007) refined its use in wood with data interpolation and trajectory updating. The only recorded application of BP in concrete is found in Fan, Zhu and Han (2014), who used the concept of data interpolation to improve image reconstruction.

Figure 3.6 – Image reconstruction techniques found in civil engineering papers of the SR

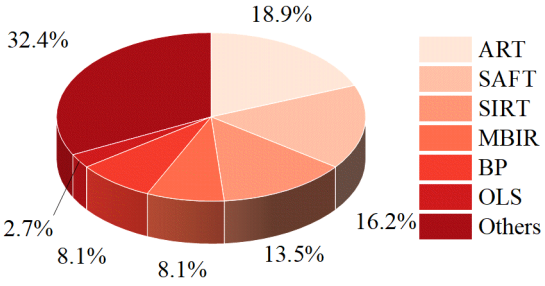

Source: the author.

ART was adopted by Kwon, Choi and Song (2005), Soetomo *et al*. (2016), Zielińska and Rucka (2020), and Basu *et al.* (2021), who were all interested in inspections of concrete structures, namely full-scale testing, reinforced concrete, or damage evolution. Although ART has been largely applied, Haach and Juliani (2014) reported SIRT performed better in comparison to OLS and ART. Moreover, heterogeneities can be more easily detected in images generated from SIRT (Haach; Ramirez, 2016).

SAFT algorithm has been as widely used as ART. The difference is SAFT is adopted for reflection tomography (or one-sided tomography) and ART is used for transmission tomography. Choi, Bittner and Popovics (2016) compared the two techniques for reinforced concrete inspection and Tseng, Chang, and Wang (2018) applied SAFT as an efficient technique. Ghosh *et al*. (2020) also used it for the evaluation of corrosion-induced damage in concrete and introduced a technique that combines P-wave and Rayleigh wave imaging.

MBIR, another image reconstruction algorithm widely used in concrete imaging, was implemented by Almansouri *et al.* (2015) and Almansouri *et al.* (2016) for reconstructing images of thick-concrete structures. More recently, Ezell *et al.* (2019) produced high-quality images of concrete structures with a modified MBIR technique (U-MBIR).

Techniques less adopted in civil engineering are regularization (Zhu *et al*. (2015)), algebraic and iterative ones (Aggelis *et al*. (2009) and Fang and Li (2009)), optimization in signal analysis (Wang *et al.* (2022)), and MLEM (Fan *et al.* (2017)).

3.2.4 Input data for image reconstruction techniques in Civil Engineering

Chai *et al.* (2011) and Basu *et al.* (2021) attempted to evaluate the best input data, namely TOF or amplitude decay for image reconstruction and highlighted a higher sensitivity of the attenuation results, which enabled the generation of higher contrast in the images. This is due to the attenuation of sonic waves being more sensitive to some internal defects and features in comparison to the velocity of the wave (Cam; Villa; Anastasio, 2022). However, care must be taken in heterogeneous samples and experimental setup problems for attenuation tomography. Figure 3.7 shows a classification of papers on such a topic – most authors use TOF.

Figure 3.7 – Input data for civil engineering image reconstruction algorithms

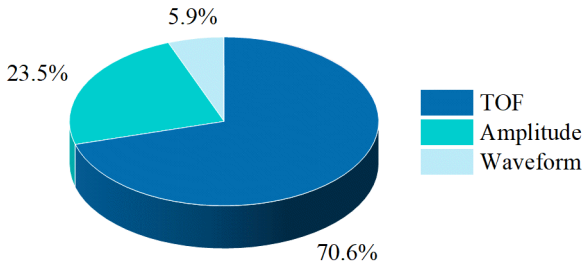

Source: the author.

The TOF measurement is made according to the time at which the first signal appears in the ultrasound readings for each measured pulse. Amplitude decay is a more abstract concept. Peterlik *et al.* (2008) used the ratio of the amplitude of the first pulse received from the studied sample by the amplitude of the pulse in the water. Niu *et al.* (2021), who worked with concrete, considered attenuation the ratio of arrival amplitudes at the receiver and the transducer output amplitudes for each measurement.

Regarding initiatives for the union of data, Niu *et al.* (2021) adopted probabilistic theories to generate images from the combination of time of flight and wave attenuation. Waveform, studied by Zhu *et al.* (2015) and Ghosh *et al.* (2020), has been classified as "other" data to be extracted for input in imaging algorithms (see Figure 3.7).

3.3 Chapter overview

The systematic review addressed in this chapter showed the main image reconstruction techniques discussed in the literature and presented BP as a consolidated one. The scenario is

different for concrete tomography and relatively few studies have focused on BP. Velocity tomography is the most usual, whereas the adoption of attenuation tomography still faces difficulties. A graphical abstract was designed to highlight this SR conclusions (see Figure 3.8).

Figure 3.8 – Graphical abstract of this chapter

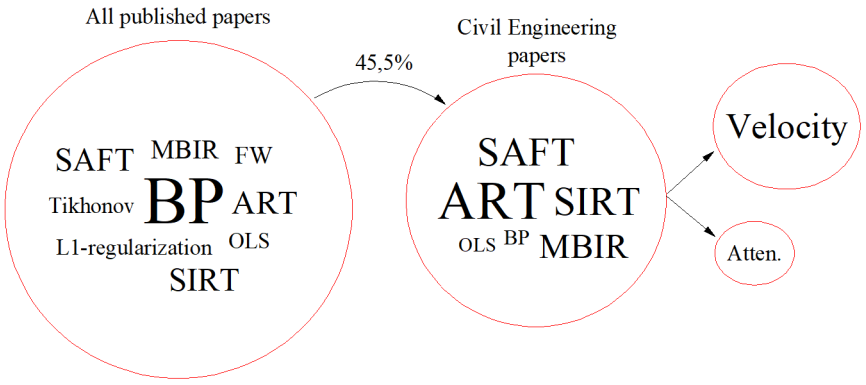

Source: the author.

4 METHODS

This chapter is dedicated to the Methods section, beginning with the implementation of the Backprojection and Filtered Backprojection processes. In conjunction with the implementation of the interpolation processes using Inverse Distance Weighting (IDW) and Artificial Neural Networks (ANN), and the Genetic Algorithm (GA), an initial numerical analysis was conducted. Following the completion of all implementations in TUSom, the final numerical analysis was performed. During the experimental analysis, a study on the adaptation of inputs for tomography generation with time of flight and amplitude decay was developed. Towards the conclusion of this work, two proposals for innovative techniques, based on previous results, were presented, as shown in Figure 4.1.

Figure 4.1 – Method steps

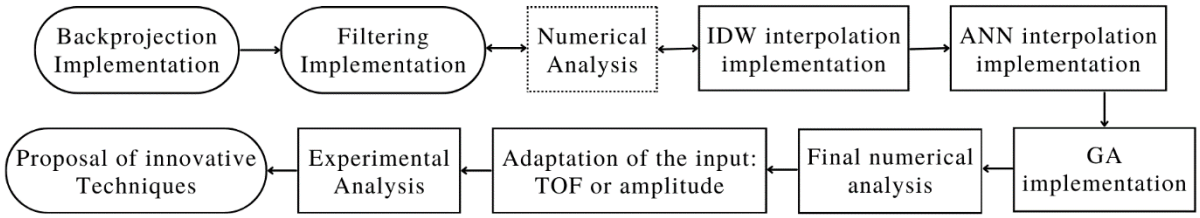

Source: the author.

4.1 Backprojection Implementation

According to Rodriguez (2021), the idea of BP can be used in a simplified method that quantifies errors at each back-projection of data and updates the input data with a redistribution of those errors. This Backprojection version directly finds the image with the overlap of the back-projected values and correction of the errors for any number of measurements.

Whereas algebraic techniques have a geometric interpretation for converging on the best numerical response, BP converges on the image by superimposing measured values, i. e., the numerical response is not the priority. The process starts with an initial guess of the slowness or attenuation coefficient for the nodes K_i and then Equation (19) calculates T_j. The error is calculated by Equation (20) and the K_i^{m+1} values are actualized and projected again in Equation (19).

$$T_j = S_{ij} K_i \tag{19}$$

$$K_i^{m+1} = K_i^m + \frac{K_i^m \, T_{j,calculated}}{T_{j,measured}} \tag{20}$$

Figure 4.2 displays a schematic of the process, where BP reconstructs the image of Figure 2.3a. Initially, the algorithm takes TOF of the ultrasonic wave as input data for the generation of velocity maps. After the modification has been implemented in TUSom for the use of the wave amplitude as input data, attenuation maps are generated.

Figure 4.2 – Representation of Backprojection algorithm

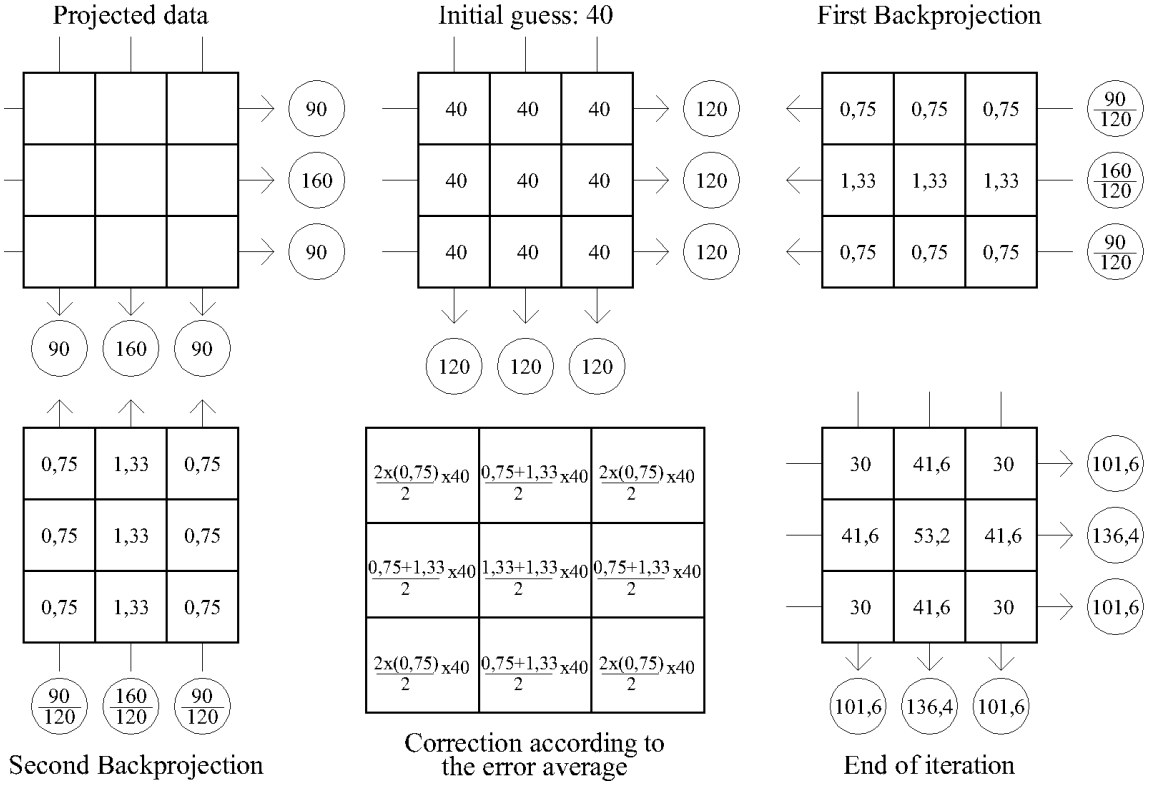

Source: the author.

4.2 Filtered Backprojection Implementation

To apply a filter and improve an image, initially generated with the Backprojection technique in the time domain, it undergoes transformation to the frequency domain through the application of the 2D Fourier Transform. This involves transforming a function into sine and cosine components. Suppose $f(x, y)$ is a continuous function of real variables x and y, the Fourier Transform of $f(x, y)$ is defined by Equation (21) and the inverse is showed by Equation (22).

$$F(u,v) = \int_{-\infty}^{\infty}\int_{-\infty}^{\infty} f(x,y)\exp[-j2\pi\,(ux+vy)]\,dxdy \tag{21}$$

$$f(x,y) = \int_{-\infty}^{\infty}\int_{-\infty}^{\infty} F(u,v)\exp[j2\pi\,(ux+vy)]\,dudv \tag{22}$$

For implementation, the Discrete Fourier Transform (DFT) is used, and direct and inverse calculations are shown in Equations (23) and (24). M and N are the number of pixels in x and y direction, respectively, and u and v are the coordinates in frequency domain.

$$F(u,v) = \sum_{x=0}^{M-1}\sum_{y=0}^{N-1} f(x,y)\exp\left[-j2\pi\,\left(\frac{ux}{M}+\frac{vy}{N}\right)\right] \tag{23}$$
$$for\ u = 0,\dots,M-1\ and\ v = 0,\dots,N-1$$

$$f(x,y) = \sum_{u=0}^{M-1}\sum_{v=0}^{N-1} F(u,v)\exp\left[j2\pi\,\left(\frac{ux}{M}+\frac{vy}{N}\right)\right] \tag{24}$$
$$for\ x = 0,\dots,M-1\ and\ y = 0,\dots,N-1$$

By employing Euler's formula, the exponential term within the sum can be expressed as shown in Equation (25). Subsequently, for direct DFT, the signal magnitude and phase are computed using Equations (26) and (27), where the real and imaginary values are determined by Equations (28) and (29), respectively.

$$\exp\left[-j2\pi\,\left(\frac{ux}{M}+\frac{vy}{N}\right)\right] = \cos\left(2\pi\,\left(\frac{ux}{M}+\frac{vy}{N}\right)\right) - jsin\left(2\pi\,\left(\frac{ux}{M}+\frac{vy}{N}\right)\right) \tag{25}$$

$$\text{Magnitude(u,v)} = (Real(u,v)^2 + Imag(u,v)^2)^{1/2} \tag{26}$$

$$\text{Phase(u,v)} = \tan^{-1}(Imag(u,v)/Real(u,v)) \tag{27}$$

$$\text{Real(u,v)} = \sum_{x=0}^{M-1}\sum_{y=0}^{N-1} f(x,y)\cos\left(2\pi\,\left(\frac{ux}{M}+\frac{vy}{N}\right)\right) \tag{28}$$

$$\mathrm{Imag(u,v)} = \sum_{x=0}^{M-1}\sum_{y=0}^{N-1} -f(x,y)\sin\left(2\pi\left(\frac{ux}{M}+\frac{vy}{N}\right)\right) \tag{29}$$

After direct DFT, a filter function multiplies the magnitude function in frequency domain in order to remove higher frequencies and eliminate noise. In this work, the so-called Butterworth low-pass filter was applied in the frequency domain 2D signal. According to Pinto (2021), a Butterworth low-pass filter is a filter that maintains the amplitude of the output signal fixed until a critical frequency value is reached. At this frequency and for all higher frequencies, the output is attenuated. This filter function is presented by Equation (30), where $D(u,v)$ is the distance between each point from the center of the image function in frequency domain (called spatial frequency). D_0 is the cut-off frequency, that was defined as 80% of the largest distance and n represents the order of the low-pass filter, defined as 2, that governs how quickly the filter attenuates higher-frequency components in the signal and was defined as four after some previous simulations. Figure 4.3 depicts the applied Butterworth filter with an order of 2 and a cut-off frequency of 0.8.

$$\mathrm{H(u,v)} = \frac{1}{1+(D(u,v)/D_0)^{2n}} \tag{30}$$

Figure 4.3 – Butterworth low-pass filter

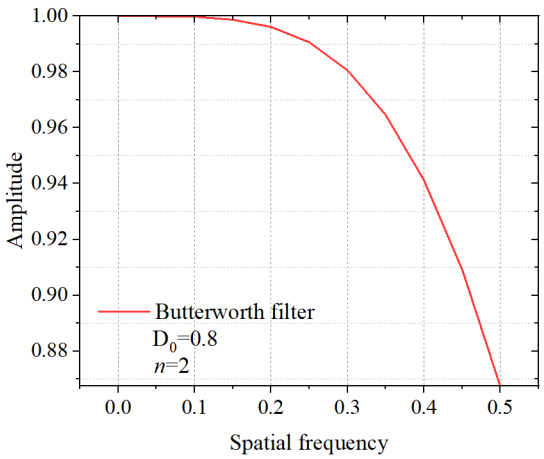

Source: the author.

To have the Filtered Backprojection reconstructed image, after the filtering, the inverse DFT is computed with Equation (24). An overview of the filtering process is explained in Figure 4.4.

Figure 4.4 – Overview of filtering process

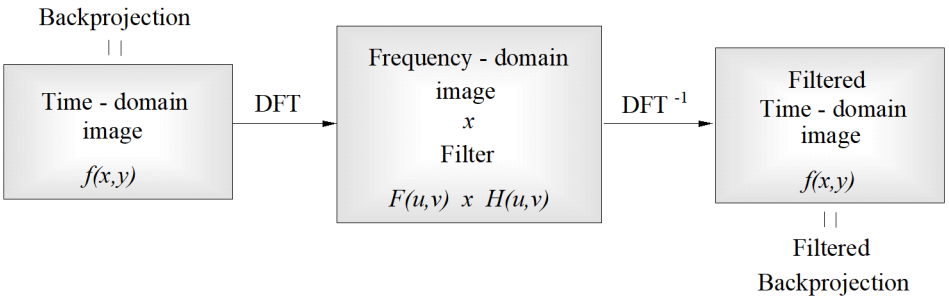

Source: the author.

4.3 Image evaluation with simulated examples

Cross sections of homogeneous concrete elements with controlled damage were numerically simulated with TUSom software. By simulating, the efficiency of imaging algorithms can be tested excluding the concrete heterogeneity factor during the evaluation of the method. Cubes of 150x150 mm² and rectangular prisms of 150x500 mm² were adopted for the study. The damage is represented by low-velocity zones (330 m/s – ultrasound wave velocity in air), whereas sound concrete is represented by high velocity (4500 m/s – average ultrasound wave velocity in sound concrete). The damaged area was represented by particles of different sizes or shapes (see Figure 4.5) by using the Particles Creation tool available in TUSom (Figure 2.5a).

Figure 4.5 – Simulated examples

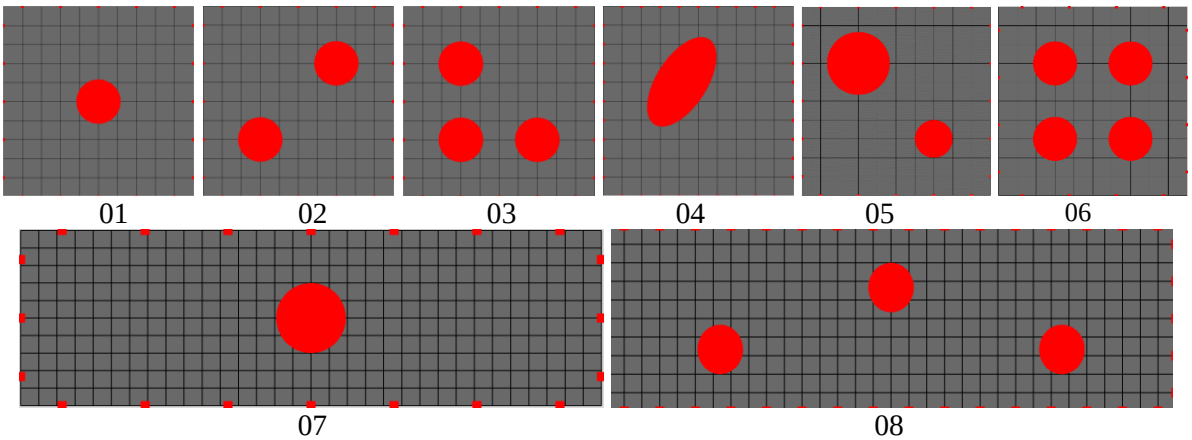

Source: the author.

For each model with an initial mesh defined as 10x10 for square models and 10x32 for rectangular models, a set of measurement lines is established. As depicted in Figure 4.6, the number of measurements varied: 54, 96, and 150 were studied in cube specimens, while 142,

208, and 601 measurements were examined in rectangular prism specimens. After defining velocity in the mesh and particles, TUSom Analysis 1 (Figure 2.5b) was employed to update the path of each measurement based on the fastest wave path between transducers. This approach ensures a more accurate simulation in accordance with a real ultrasound problem (Giglio, 2021). Subsequently, TUSom Analysis 2 was utilized to obtain simulated TOF for each measurement.

Figure 4.6 also illustrates the procedures post simulating TOF. To enhance image quality, the mesh configuration was studied as a parameter. The mesh was defined as 5x5, 10x10, and 20x20 in cube specimens and 5x16, 8x20, and 10x32 in rectangular prism specimens. The simulated TOF enable the production of tomographic images using Analysis 3 (Figure 2.5b) by selecting a specific technique (OLS, SIRT, ART, BP, or FBP) and specifying the number of iterations. Following a comparative analysis between BP and FBP image reconstructions, it was determined that FBP outperformed, leading to the presented comparison between OLS, SIRT, ART, and FBP. As shown in Figure 4.6, the total number of reconstructed and compared images was 1728, with 216 per model.

For image reconstruction, constraints values should be set in order to algebraic techniques to converge. Minimum and maximum nodal velocities were set as 100 m/s and 5500 m/s, and minimum and maximum nodal attenuation were set as 0 m^{-1} and 1 m^{-1}.

Figure 4.6 – Numerical methodology for image reconstruction comparison: variables of the analysis are highlighted in gray

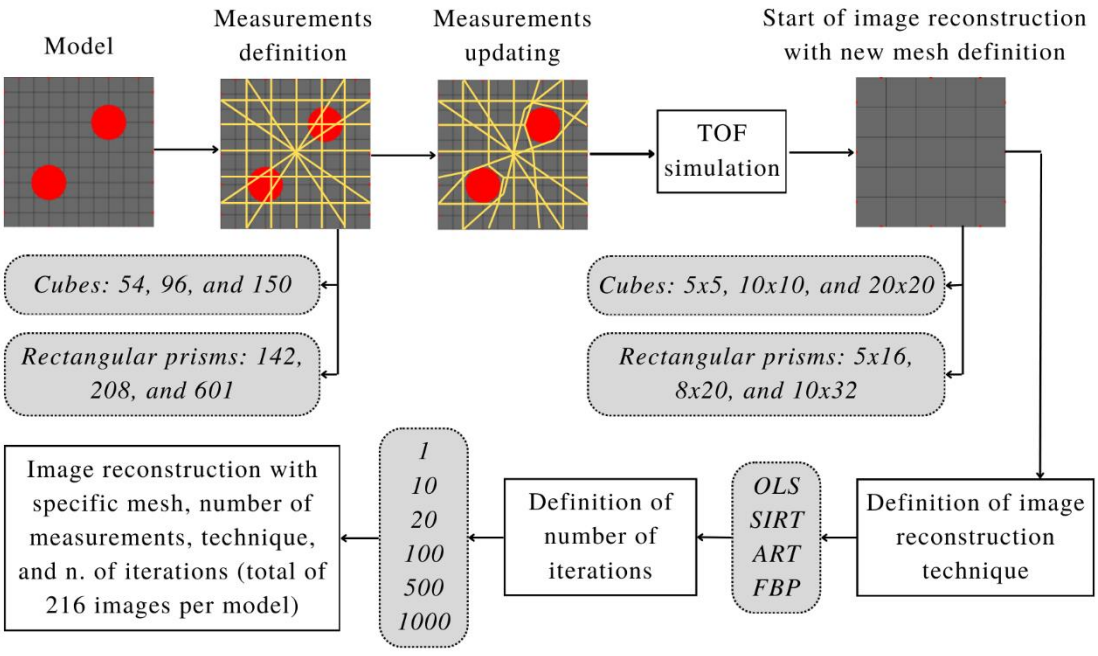

Source: the author.

Images generated with FBP were compared with those with ART, SIRT, and OLS regarding Image Correlation Coefficient (ICC) which, according to Li *et al.* (2021), is commonly used for comparative image analyses. As presented in Equation (31), ICC compares the nodal slowness of the reconstructed image (X_i) with the real image (x_i). The results are expressed as values ranging from 0 to 1, where 1 indicates a situation in which the nodal coefficients (velocity or attenuation) of the reconstructed image perfectly match the model's nodal coefficients.

$$ICC = \frac{\sum_{i=1}^{n}(X_i - \bar{X})(x_i - \bar{x})}{\sqrt{\sum_{i=1}^{n}(X_i - \bar{X})^2 \sum_{i=1}^{n}(x_i - \bar{x})^2}} \tag{31}$$

4.4 Input data from experimental tests: time of flight and amplitude

As mentioned earlier, TUSom is capable of processing TOF data to generate velocity tomography. In an ultrasound test, obtaining the TOF corresponds to recording the arrival time of the first p-wave of each measurement. In order to obtain the exact arrival time, a methodology developed by Schiavon (2015) was employed. The methodology consists on the application of Equations (32), (33), and (34) in the time-domain ultrasound signal $f(x)$. Equation (34) represents a function that reveals the exact arrival time, identifying the first point where it differs from zero.

$$h(x) = |f(x)| \tag{32}$$

$$g(z) = \max_{0 \le x \le z}\{|h(x)|\} \tag{33}$$

$$w(z) = \lim_{\xi \to 0^+} \frac{g(z+\xi) - g(z)}{\xi} \tag{34}$$

To generate attenuation topography from the same recorder signals, the amplitude decay between transducers was calculated using the Hilbert Transform on the time-domain signal. This transform, according to Freeseman, Hoegh and Khazanovich (2016), allows to find the signal's instantaneous amplitudes, building an amplitude envelope that eliminates the signal's negative phases. After calculating the transformed function, proposed in Equation (35) by Zayed (1998), an offset of 10 μs from the arrival time is applied to obtain the amplitude (see Figure 4.7). The establishment of the offset aims to standardize the procedure while eliminating signal noise.

$$H[f(x)] = \tilde{f}(t) = \frac{1}{\pi}\int_{-\infty}^{\infty} \frac{f(x)}{t-x}dx \tag{35}$$

The data entry procedure in TUSom was adjusted for the generation of attenuation maps, allowing the user to choose the type of input data, namely TOF or amplitude. Since Equations (3) and (8) are the same, the image reconstruction procedure is not changed. The actualized process of image generation in TUSom is displayed in Figure 4.7.

Figure 4.7 – Flowchart of possible numerical analysis for tomography in TUSom

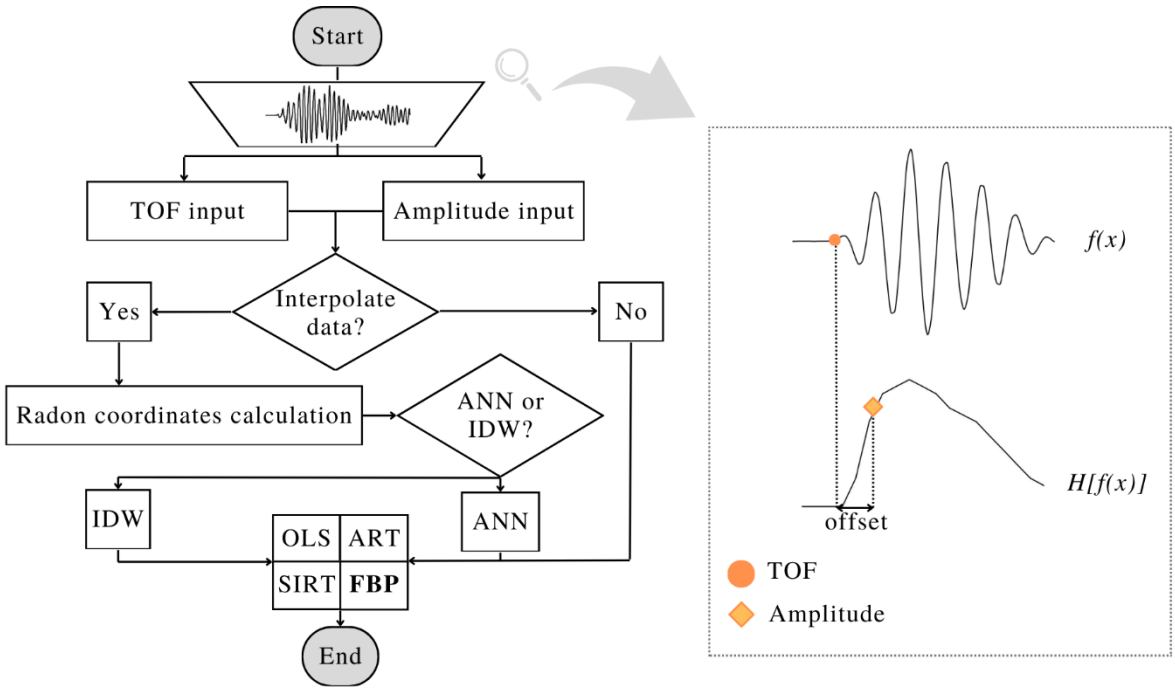

Source: the author.

4.5 Image evaluation with experimental examples

Concrete cubes and prisms of 15x15x15 cm³ and 15x15x50 cm³, respectively, were molded for the experimental analysis. The mix proportion of concrete was based on IPT/EPUSP dosage diagrams adopted at the Building Materials Laboratory of the São Carlos School of Engineering of the University of São Paulo (USP). With a cement consumption of 438.96 kg/m³, the mix adopted for Brazilian strength class C30 was 1:1.756:2.444:0.4 (cement: fine aggregate: coarse aggregate: water/cement ratio). Additionally, a superplasticizer was incorporated at a rate of 1% of the cement mass. High initial resistance Portland cement (CPV ARI) was employed, along with natural quartz sand (classified as medium, with a fineness

modulus of 2.94, maximum characteristic dimension of 2.36 mm, and specific mass of 2.59 g/cm^3), and basaltic coarse aggregate (with a maximum characteristic dimension of 9.5 mm, and specific mass of 3.00 g/cm^3).

Three 5x10 cm³ cylinder specimens were molded from each concrete mixing batch for the purpose of compressive strength control. The concrete mixture and specimen's preparation occurred in three stages because only one mold of steel and wood was developed (see Figure 4.8). Each concreting was performed on consecutive days.

Figure 4.8 – Developed mold for concreting cubes of 15x15x15 cm³ within the standard mold of 15x15x50 cm³

Source: the author.

During mixture, Polyvinyl Chloride pipes and Styrofoam were embedded to simulate artificial defects. Seven experimental specimens, namely six cubes and one rectangular prism were molded. Figure 4.9 displays the configuration of pipes and Styrofoam inside the concrete. Pipes of 5 cm of diameter were used in models 01 and 04; of 2.5 cm in model 02; of 3.2 cm in models 03, 05 and 06; and of 2.8 cm in models 04, 05 and 06. The Styrofoam in model 07 has 6 cm of diameter.

Figure 4.9 – Experimental models

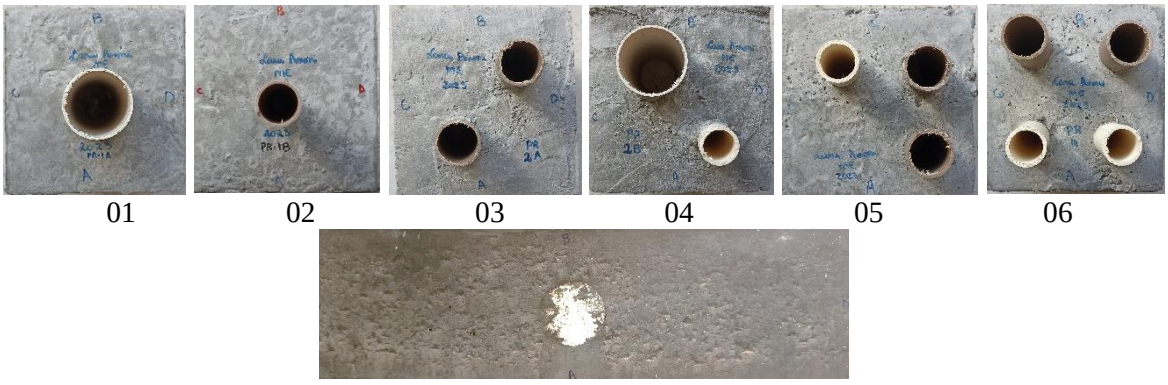

01 02 03 04 05 06

07

Source: the author.

Ultrasonic testing on prisms was carried out through transmission tomography, employing longitudinal (or pressure p-) waves with a frequency of 250 kHz. The ultrasound equipment employed in this study was the Pundit Lab+ by Proceq®. In each tested measurement line, ten pulsed signals were emitted and received to obtain the signal average and minimize errors. The measurement geometry adheres to the configuration depicted in Figure 4.10. The 250 kHz transducer, with a diameter of 3 centimeters, influenced the number of defined measurement points. For the 15x15 cm² transversal section, there were 5 measurement points on each surface, totaling 150 measurements. The rectangular section of 15x50 cm² featured 5 measurement points on the 15 cm surface and 15 measurement points on the 50 cm surface, resulting in a total of 550 measurement lines.

Figure 4.10 – Measurement lines in experimental tests

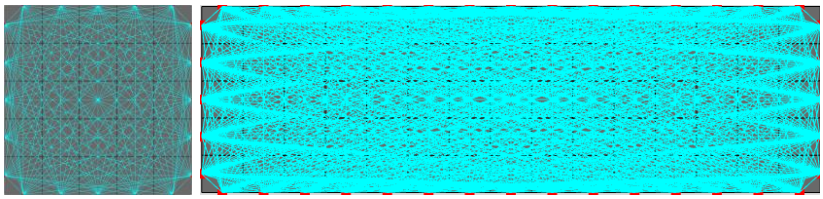

Source: the author.

During the ultrasonic tests, a method for improving the standardization of measurements was developed. Before initiating the tests, the entire region designated for measurement points was wetted with coupling gel. This ensured that the concrete retained moisture, guaranteeing uniformity in measurements during the test. The preparation and ultrasonic tests on the cubes each took 40 minutes (see the test in Figure 4.11). However, for the rectangular prism, the time spent was more extensive, totaling 3 hours to be completed.

Figure 4.11 – Ultrasonic test in the experimental Model 04

Source: the author.

For image reconstruction, constraints values should be set in order to algebraic techniques to converge. As specified for numerical simulation, minimum and maximum nodal velocities were set as 100 m/s and 5500 m/s, and minimum and maximum nodal attenuation were set as 0 m^{-1} and 1 m^{-1}.

The Confusion Matrix methodology was adopted for the similarity analysis between real and reconstructed images for avoiding biased comparisons and interpretations. The Confusion Matrix concept is the superposition of real and reconstructed images and their subdivision in pixels, thus defining false positive (FP), false negative (FN), true positive (TP), and true negative (TN) regions. Figure 4.12 illustrates the superposition process.

The methodology enables calculations of the accuracy of results (Equation (36)), which provides the percentage of examples correctly classified. Equation (37) calculates the precision (reliability in positive and negative predictions) (Urure, 2020). With this methodology, implemented in MATLAB®, all images generated with FBP were compared with those generated with SIRT, ART, and OLS.

Figure 4.12 – Matrix superposition process. a) the real image; b) the reconstructed image; c) the comparison between the model and the result

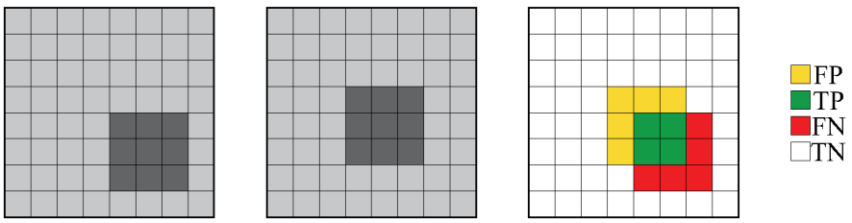

(a) (b) (c)

Source: the author.

$$A = \frac{TP + TN}{TP + FN + FP + TN} \tag{36}$$

$$P_{prediction} = \frac{TP}{TP + FP} \qquad N_{prediction} = \frac{TN}{TN + FN} \tag{37}$$

4.6 IDW for measurements interpolation

The number of data obtained in the ultrasound test of concrete structures is smaller than that of the widely recognized data acquired in medical tomography. An interpolation technique called Inverse Distance Weight (IDW), largely adopted in geography studies for maps

generation, is employed for increasing the amount of collected data according to studies from Dreifke (2019) and Neris (2019). Nearby points establish a stronger correlation, enabling the estimation of data from unknown points through sampled points.

IDW was adopted for interpolating the TOF values for each new measurement added in an initial set of regular measurements (Figure 4.13). The data related to this initial set can be obtained by performing ultrasonic test or by simulating the test. The interpolated TOF (Z_p) is calculated by Equation (38). The inverse of distance (d_i) of each point with known TOF (z_i) from the new point to be generated is weighted according to the influence to be obtained from the nearby points. The higher the weight (p), the greater the influence of nearby points.

Figure 4.13 – Measurement interpolation with IDW: (a) regular number of measurements with known TOF; (b) regular + interpolated measurements and new TOF obtained with IDW

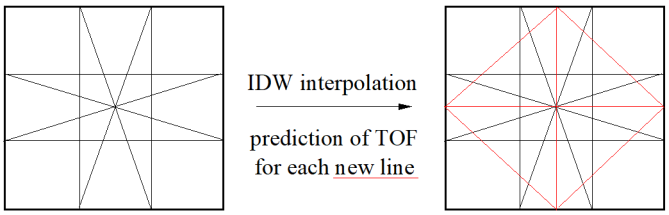

(a) (b)

Source: the author.

$$Z_p = \frac{\sum_{i=1}^{n}\left(\frac{1}{d_i^p} \times z_i\right)}{\sum_{i=1}^{n}\left(\frac{1}{d_i^p}\right)} \tag{38}$$

To establish the coordinates of points to be interpolated, the same concept of Radon domain, i.e., each ultrasound reading is a projection of data and has certain coordinates s and θ, is used. In TUSom, the mesh generated and the definition of the measurement paths have a reference of origin on the lower left corner. Therefore, s and θ can be determined from that origin for each projection. The orthogonal distance between the center and the projection (s) and the angle of measurement (θ) are geometrically found and calculated, as shown in Figure 4.14.

Figure 4.14 – Finding of the Radon coordinate of a projection by geometrical approach

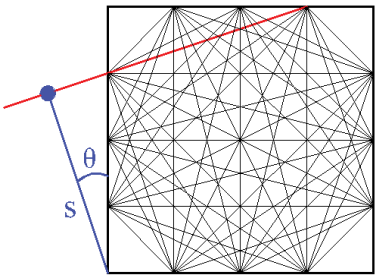

Source: the author.

Towards facilitating the calculation of the distance between the points, Polar Coordinates can be converted to Cartesian Coordinates, as shown in Equations (39) and (40).

$$x = s \times \sin(\theta) \tag{39}$$

$$y = s \times \cos(\theta) \tag{40}$$

Coordinates x and y represent each measurement which saves the data collected by ultrasound test, namely time of flight or amplitude decay. Such ultrasound data must be normalized by distance because of the difference in each measurement. Therefore, the interpolated data will be the velocity of the wave, in the case of TOF, since velocity is already related to distance traveled. After interpolation in terms of velocity, Equation (2) calculates the TOF of each new interpolated measurement.

Equation (38) provides the IDW interpolation, since the distance between points in Radon domain (d_i) can be calculated and each point has its normalized data (z_i). The number of new points created between the existing ones is defined by the TUSom user.

Both weight (p) and number of points that will enter the interpolation for the creation of a new point are a user´s choice. The interference radius is also defined by the user so that any point within the defined radius participates in the interpolation. Another option is to choose the number of points (n) – those closest to the point to be interpolated participate in the interpolation.

4.7 Artificial Neural Networks for measurements interpolation

In addition to utilizing IDW interpolation, Artificial Neural Networks (ANN) were also adopted for predicting TOF values for each new measurement interpolated from an initial set of regular measurements (same idea presented in Figure 4.13). ANN algorithm was

implemented in TUSom and the structure of the ANN is showed in Figure 4.15. The structure consists in 4 neurons in input layer, which one representing the coordinates of emitter and receiver transducer's location for a measurement and one neuron as output layer that represents the TOF of the wave. Inputs and outputs were normalized between -0.75 and 0.75 with min-max normalization.

Figure 4.15 – Artificial Neural Network Architecture

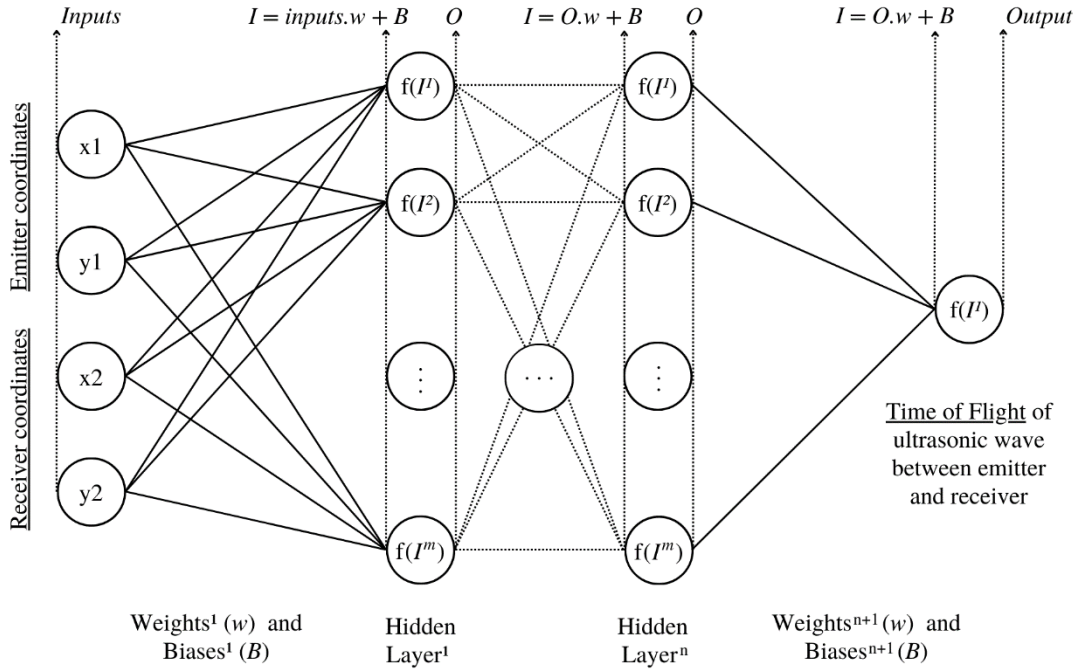

Source: the author.

Concerning the number of hidden layers (n) and the number of neurons in each layer (m), the code was implemented to allow for flexibility in adjusting these parameters to enhance ANN performance. Weights and biases are initialized using Xavier initialization. The goal of Xavier Initialization is to initialize the weights so that the variance of the activations remains consistent across every layer. This uniform variance helps prevent issues like the gradient exploding or vanishing (Ng, 2022). According to this initialization, the adopted values have an average equal to 0 and fall within the range $[-limit, limit]$ (Equation (41)). Na corresponds to the number of neurons in the current layer, and Nn in the next layer.

$$limit = \sqrt{\frac{6}{Na + Nn}} \tag{41}$$

The updating of weights and biases is achieved through a backpropagation algorithm, and the hyperbolic tangent function serves as the activation function (Equation (42)).

$$F(x) = \tanh(x) \tag{42}$$

The learning rate during the backpropagation process is dynamically adjusted for each layer and neuron according to the gradient response. If the gradient has the same direction in consecutive epochs, the learning rate is increased; conversely, if they have different directions, the learning rate is decreased to achieve the best solution. The termination criteria were set as the Mean Squared Error (MSE) reaching 10^{-5} or the maximum number of epochs for training, which is a variable in the analysis.

In a general context, the initial procedure for ANN algorithms involves dividing data into training and testing sets. However, in the context of ultrasonic testing, a specific challenge arises. The dataset is limited due to labor-intensive efforts, and the architecture, as well as the final weights and biases, must be customized for each unique geometry and internal structure of the analyzed object. This renders it inefficient to attain a single set of weights and biases capable of addressing all interpolation challenges. Consequently, all available data for a specific problem was utilized for training (150 measurement lines), and more simulated data was used for testing (96 new measurement lines). The numerical models presented in Figure 4.5 were adopted for training and testing the ANN efficiency in TOF prediction for image reconstruction.

4.8 Genetic Algorithm for ANN and IDW parameters optimization

The concept of incorporating optimization algorithms with bioinspired characteristics emerged as a means to achieve the objective of predicting the optimal parameters for IDW interpolation computation and ANN structure. The Genetic Algorithm (GA) is an adaptive algorithm proposed by Professor Holland in 1975 inspired by natural selection processes (Giglio, 2021). It operates on a population of potential solutions, aiming to evolve and enhance these solutions over multiple generations to identify an optimal or near-optimal solution for a given problem. In its core structure, a GA begins with the random creation of a population consisting of potential solutions, often referred to as individuals (or chromosomes). Each individual embodies a candidate solution, represented in a genetic format. In this work, binary encoding (0 and 1) was used to denote the specific analyzed parameters.

For IDW interpolation, each individual is composed by 12 bits, two bits for number of generated points between existing ones, four bits for weight parameter of IDW interpolation and six bits for interpolation ratio. For ANN interpolation, each individual is composed primary by 17 bits, fourteen bits for number of epochs, three bits for number of hidden layers and more six bits are extrapolated for each number of hidden layers, to represent the number of neurons in each hidden layer.

After population generation, the fitness of each individual is calculated. The fitness refers to a measure of how well an individual solution performs with respect to the problem's objective. In IDW parameter optimization, the objective function is tied to the accuracy of the generated image. Therefore, this fitness is computed after image generation with interpolated data from IDW, representing the coefficient of variation (CV) between the generated velocity/attenuation map and all recorded measurements along a path. Conversely, in ANN parameter optimization, the fitness function is the training mean squared error (MSE). Here, the aim is to minimize the training error to enhance the neural network's performance.

The selection phase follows, where individuals from the current population are chosen to form a mating pool. The selection process is based on elitism, where a certain number of individuals with the best fitness scores are preserved in next generation. The number of selected individuals is a variable and can be changed.

Next, the crossover (recombination) stage is performed. In IDW case, where number of bits is constant, uniform crossover is employed. In ANN case, where number of bits changes during the process because changings in number of hidden layers, one point crossover is employed. This approach was chosen in order to avoid errors during the crossover processing. Subsequently, random changes in genetic information, known as mutation, is performed in some of the newly generated individuals. The mutation process involves the random flipping of bits in the binary representation.

After selection, crossover and mutation, the fitness of each new individual within the new population is assessed. The genetic algorithm iteratively repeats these processes for a predetermined number of generations or until specific best fitness (IDW: 1%, ANN: 10^{-5}) is achieved.

A representation of the genetic algorithm is presented in Figure 4.16. All analyses involving IDW interpolation, as well as ANN interpolation, were conducted with the assistance of this implemented GA for parameter optimization. During each analysis, the code was run three times to compute the average accuracy and determine the location of the global minimum using the optimization method. In all tests, the crossover probability was set at 90%, the

mutation probability at 10%, and two elite individuals were maintained. Some authors claim that the sum of the percentages of crossover and mutation should equal 100% (Linden, 2006). For IDW parameters optimization, the number of epochs was set as 10 with 6 individuals. For ANN parameters optimization, the number of epochs was 20 with 10 individuals.

Figure 4.16 – Genetic Algorithm implementation

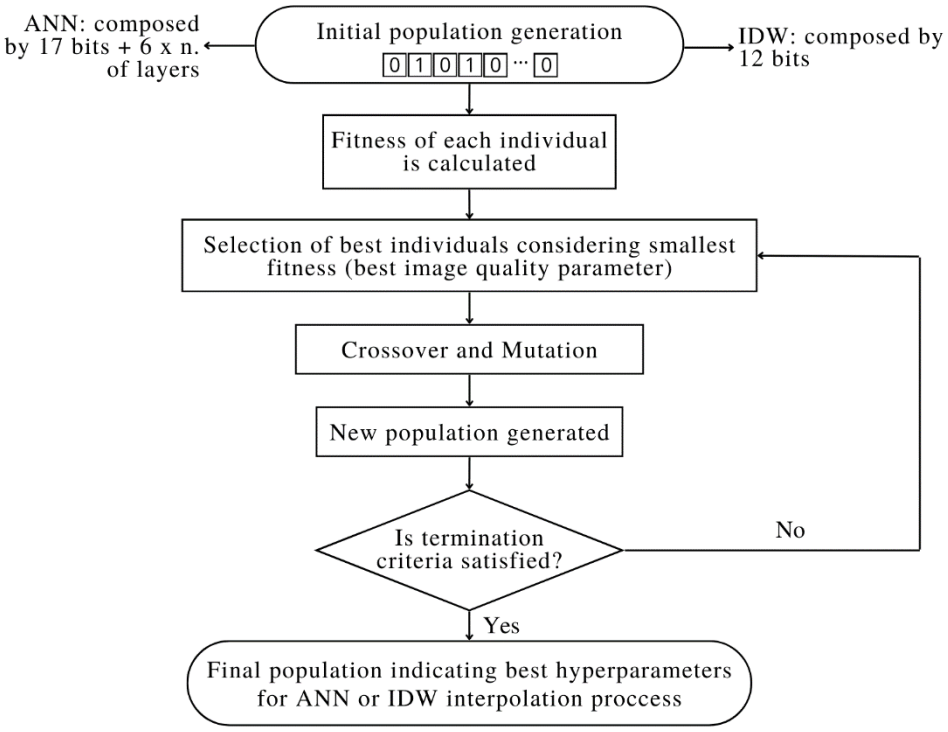

Source: the author.

4.9 Proposed innovative techniques

Throughout the course of the research, novel ideas emerged from the integration of all implemented tools and potential analyses with ultrasound data. Consequently, this subsection is divided to describe two proposed methodologies based on innovative ideas.

4.9.1 Proposed approach for reduction of time-intensive structural inspections

This approach was developed with the aim of alleviating the laborious workload associated with a high number of required measurements for image reconstruction while maintaining high image quality. To achieve this goal, due to previous studies, IDW was adopted as the interpolation tool, gradually increasing the number of measurements from an initial set

of 4 measurements with simulated TOF. The implemented genetic algorithm was employed to determine the best parameters for IDW before each interpolation. The number of new measurements generated by interpolation depends on the number of emitter and receiver points defined in the mesh. New points are added between the existing ones, and measurement lines between them are generated with interpolated TOF data. Following this process, an image with interpolated TOF is reconstructed and compared with the model.

After completing the first iteration of IDW interpolation and image reconstruction, a new iteration is initiated by selecting a new location for ultrasonic test simulation to insert additional data. The location of the new necessary training points is determined by the area where TOF exhibits the most variation. In each iteration, 4 new measurements TOF are simulated and introduced as new points for IDW interpolation calculation. This methodology was applied in order to generate velocity tomography with FBP of simulated models 01 and 02. Also, experimental model 03 will be reconstructed by nodal velocities and attenuations calculation in order to evaluate the methodology in laborious tests.

4.9.2 Proposed approach for coupling techniques

A study on the coupling of Filtered Backprojection with algebraic techniques implemented in TUSom was conducted to evaluate the reconstruction techniques within the software, aiming to generate images with higher accuracy and quality. This study utilizes the FBP response as an initial guess for algebraic reconstructions. Given that FBP demonstrates favorable results with a fine mesh (20x20), while OLS, SIRT, and ART face challenges in generating images in these situations, the coupling of FBP with these techniques will be investigated in these configurations to enhance resolution. Using FBP initial nodal coefficients guess, images of simulated models 01 to 06 were reconstructed with OLS, SIRT, and ART by changing the number of iterations (1, 10, 20, 100, 500, 1000), and a comparative analysis was conducted based on the Image Correlation Coefficient. To establish a reference, images with a constant initial guess of 500 m/s were also reconstructed using OLS, SIRT, and ART.

4.10 Chapter overview

This chapter details the implementation procedures for Backprojection, Filtered Backprojection, IDW interpolation, ANN interpolation, and Genetic Algorithm utilized in this

research. It encompasses discussions on obtaining time of flight and amplitude decay as input data for image reconstruction, presents experimental and numerical proposed analyses, and describes two innovative methodologies proposed using generated data during the course of this work.

5 RESULTS AND DISCUSSIONS

This section explores the implementation of BP and FBP, the results of IDW and ANN interpolation processes, and the efficiency of the Genetic Algorithm. Subsequently, reconstructions using FBP, BP, ART, SIRT, and OLS for both simulations and experimental models involving various test profiles were discussed. In the conclusion, the outcomes of the proposed innovative methodologies are presented.

5.1 BP and FBP reconstructions with simulated TOF

The new BP and FBP techniques were implemented in the same usual tomography interface of TUSom. A comparison between the techniques was conducted by reconstructing images from simulated models 01 to 08 (Figure 4.5) and calculating the Image Correlation Coefficient. Reconstructed images using BP and FBP are presented in Figure 5.1. Remarkably, highly accurate images were yielded by the simple BP algorithm. With only one iteration, damaged areas could be effectively highlighted.

The impact of the filter on reducing noise and enhancing the contour shape of the damaged region is demonstrated in FBP images. For both square and rectangle reconstructions of models 01 to 08, FBP visually outperformed BP. This observation is supported by numerical results, as FBP yields higher nodal velocities in sound concrete, which are closer to 4500 m/s.

Figure 5.1 – Image reconstruction of proposed numerical models with 1, 5, and 20 iterations respectively with BP (a), and with FBP (b)

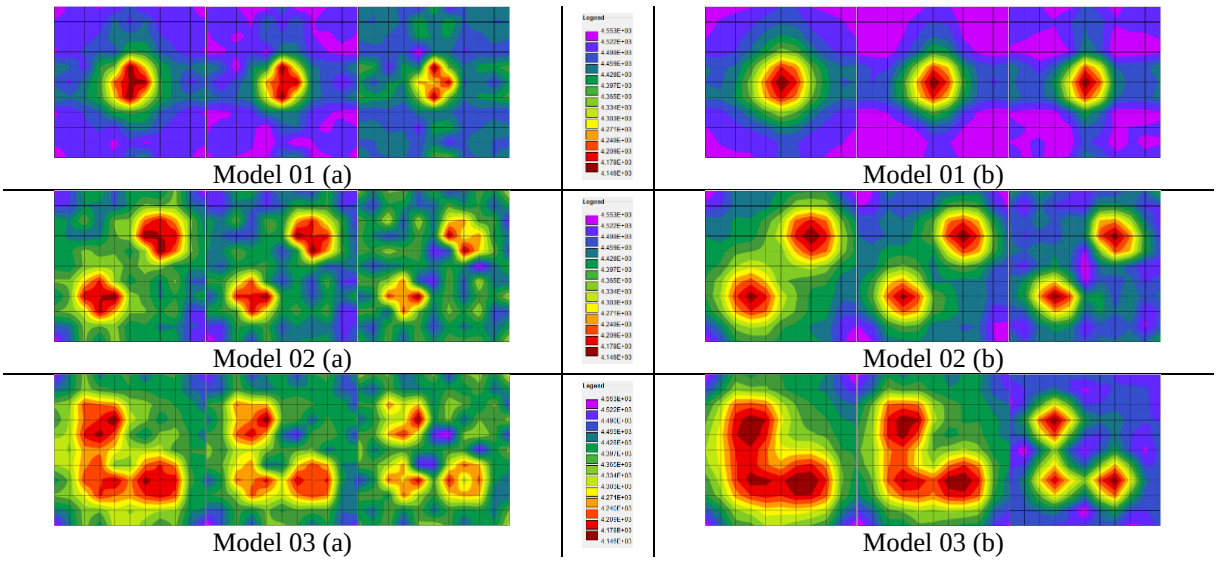

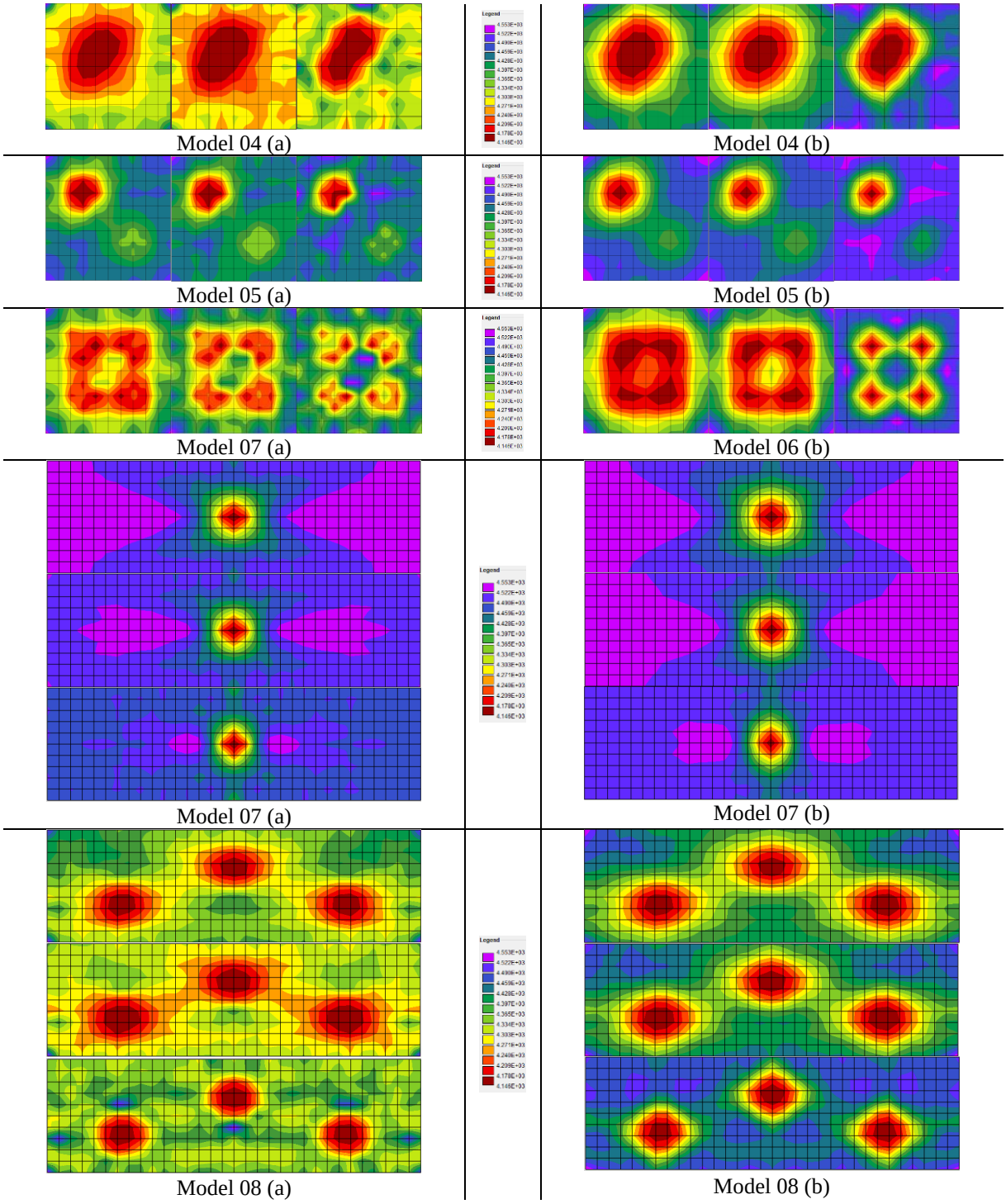

Source: the author.

To provide a comprehensive discussion of the results, the ICC was calculated for each model at 1, 10, 20, 50, 100, and 200 iterations and they are presented in Figure 5.2. The numerical analysis involving the ICC is representative in terms of nodal velocities when comparing real and reconstructed data. The significance of the maximum number of iterations becomes evident, as there is a decrease in ICC with higher iteration numbers. Generally, BP

tends to perform better with iterations ranging from 1 to 10, while FBP shows improved results between 10 and 20 iterations for square images and between 20 and 50 for rectangular images. Models 02 to 08 exhibit higher ICC with FBP, whereas only Model 01 demonstrate superior performance with BP. In a broader context, variations in ICC between BP and FBP are consistently observed, with an exception in model 01, where BP exhibited ICC. Given the advantageous noise reduction provided by filtering and the comparable ICC performance between the two techniques, FBP emerges as the overall more effective method. Consequently, the subsequent analyses of this work will employ the FBP technique for all models.

Figure 5.2 – ICC of Models 01 to 08 reconstructed with BP and FBP for different number of iterations

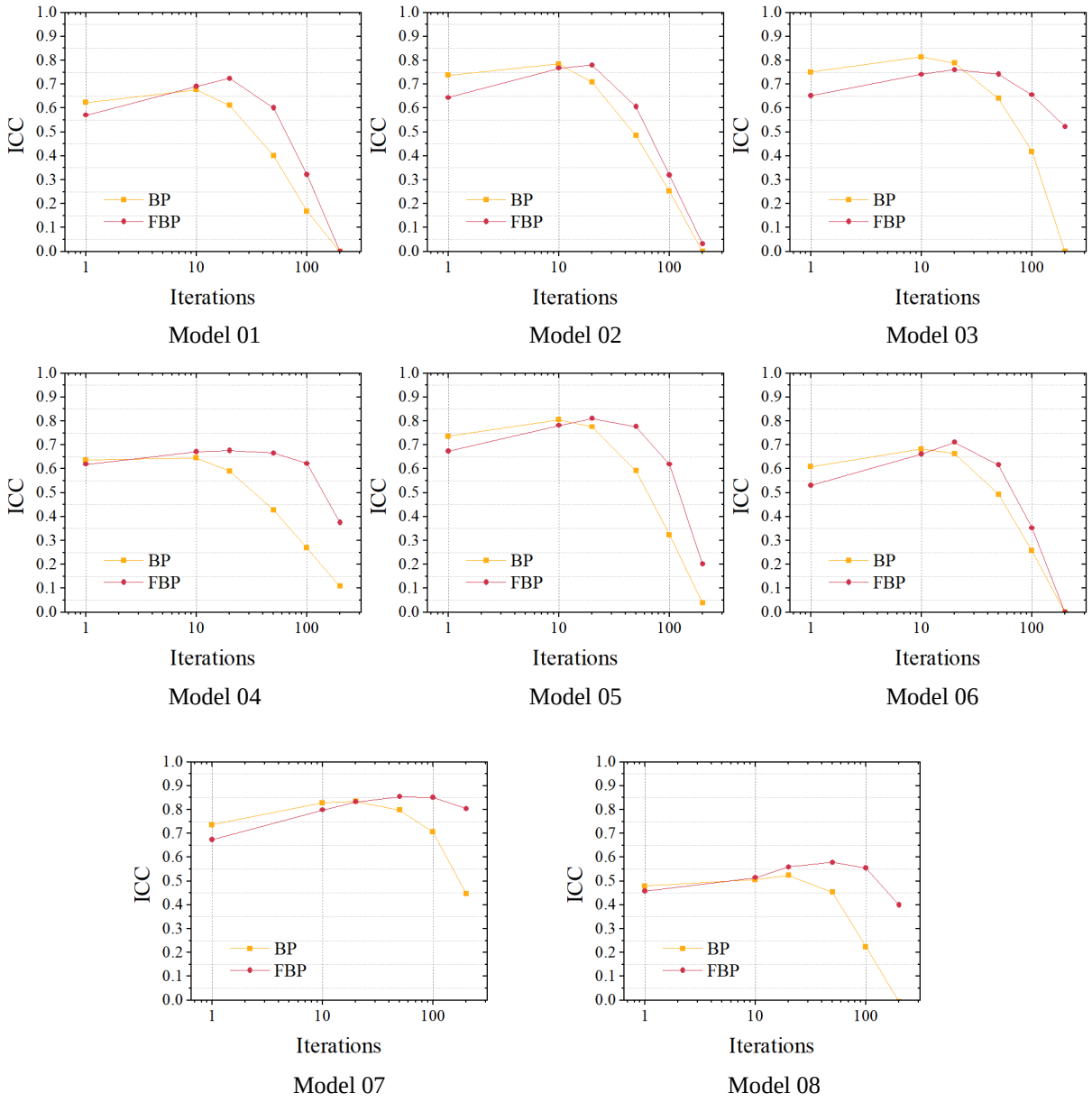

Source: the author.

5.2 Comparison between FBP and algebraic methods: simulated models

A comparison involving OLS, SIRT, ART, and FBP is presented through images reconstructed from simulated models 01 to 08 and ICC calculations. Different mesh definitions, numbers of measurement lines, iterations, and techniques were employed for each reconstructed image. In Figure 5.3, the ICC calculated for changes in parameters during Model 01 reconstruction is showcased.

One key observation from these graphics is that FBP consistently demonstrates superior performance across all combinations of definitions for Model 01, and this trend is also observed for other models. Additionally, it becomes evident that optimal results are achieved when the number of iterations falls between 10 and 20. Beyond this range, the technique experiences a decrease in performance. Conversely, other algebraic techniques, OLS, SIRT, and ART, exhibit improved performance with a larger number of iterations. OLS performs well with a poor mesh (5x5) and an increased number of measurement lines, particularly with 96 and 150 lines. SIRT and ART also show improved performance with a 5x5 mesh, although their ICC values are less than half of those for OLS and FBP. For denser meshes, such as 10x10 and 20x20, none of the algebraic techniques can generate accurate results with the proposed number of measurement lines, and ICC values do not exceed 0.2.

A correlation between the number of nodes in the mesh and the number of lines can be discussed to explain the performance of algebraic techniques. In a 5x5 mesh, with 36 nodes, having 54 measurement lines creates a problem with more equations than unknowns, allowing for multiple solutions. In this scenario, the ratio between measurement lines and nodes is 1.5. With the same mesh but 96 measurement lines, the ratio increases to 2.67, presenting a similar problem with multiple solutions. The higher number of lines could increase the likelihood of the solution converging to the correct one.

When the mesh is denser, as in a 10x10 mesh with 121 nodes, having 54 or 96 measurement lines results in a system with no solution. Only with 150 lines does it become a system with infinite solutions. In this case, the ratio between measurement lines and nodes is 1.24. However, even in this situation, the solution generates images with poor performance. This analysis suggests that only when the ratio of measurement lines to nodes is higher, as in cases like a 5x5 mesh with 96 lines (ratio: 2.67) or a 5x5 mesh with 150 lines (ratio: 4.17), can OLS, SIRT, and ART reconstruct images with good accuracy.

Figure 5.3 – ICC of Model 01 reconstructed with OLS, SIRT, ART, and FBP for different number of iterations, defined mesh and measurement lines

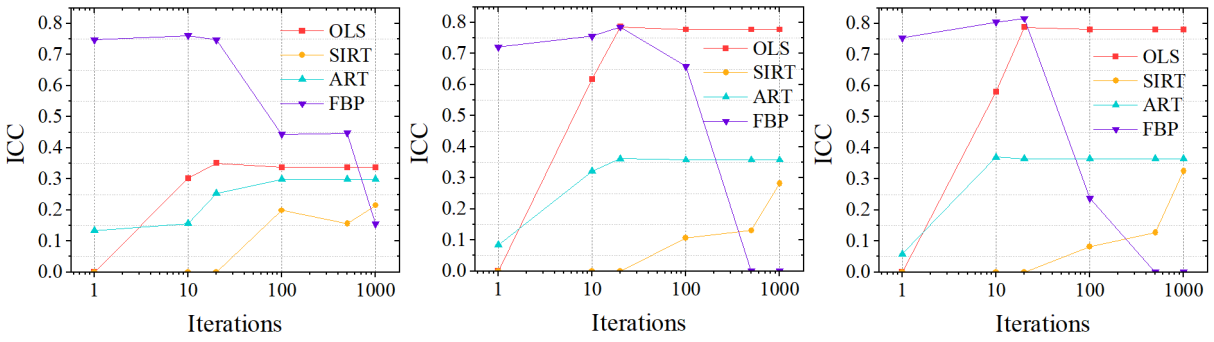

5x5 mesh and 54 lines | 5x5 mesh and 96 lines | 5x5 mesh and 150 lines

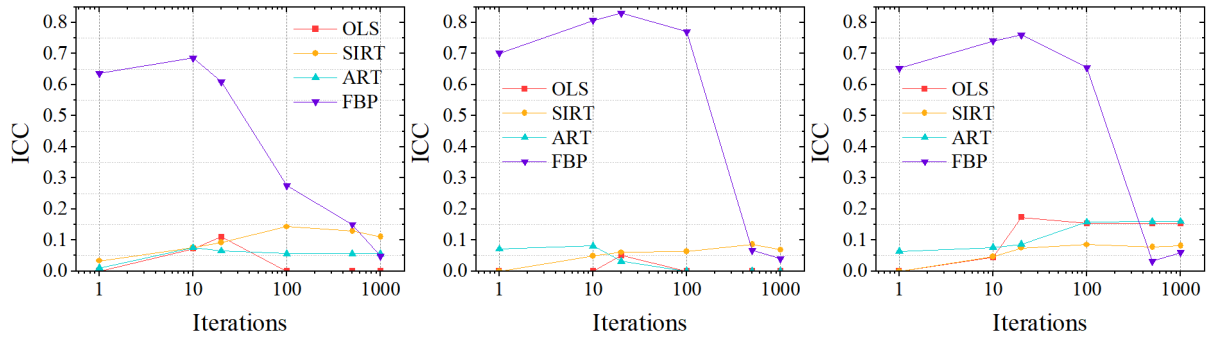

10x10 mesh and 54 lines | 10x10 mesh and 96 lines | 10x10 mesh and 150 lines

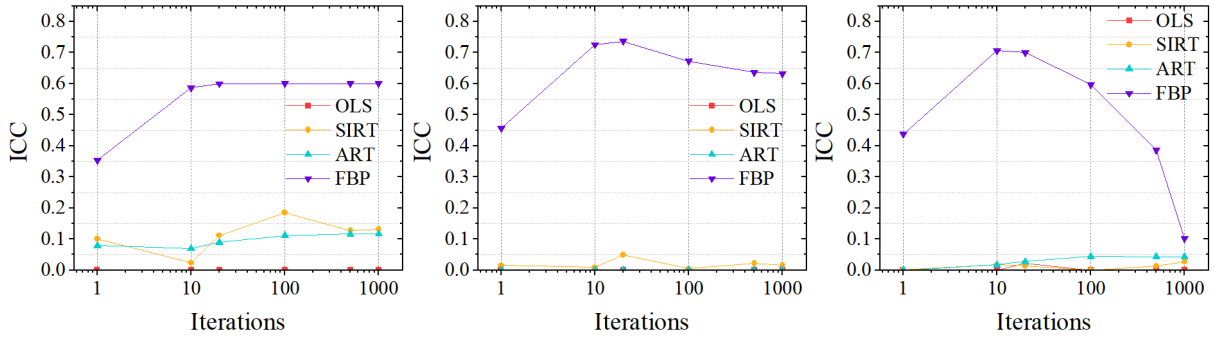

20x20 mesh and 54 lines | 20x20 mesh and 96 lines | 20x20 mesh and 150 lines

Source: the author.

To summarize the ICC values from all 1728 reconstructed images in this analysis, Table 5.1 was developed. The table outlines the optimal combinations of mesh, number of measurement lines, and iterations for each technique to achieve the highest ICC. Additionally, it presents the corresponding ICC achieved. Notably, all models, except for model 08 (rectangular prism with three damages), were better reconstructed with FBP. This is because the FBP reconstructed image of Model 08 portrayed sound concrete with a lower nodal velocity

than the values achieved with algebraic techniques, leading to a decrease in its ICC. However, ICC values for FBP reconstruction exceeded 0.8 in models 01, 02, 03, 05, 06, and 07. The second-best performance was observed with the OLS technique. While SIRT and ART exhibited divergent results for each model, overall, the performance was better with SIRT.

In general, the most effective parameters for FBP image reconstruction were a 10x10 mesh with 96 measurement lines (results with 150 lines were almost identical, but considering time-test resources, 96 is the optimum value) and 20 iterations. The fact that the best results were achieved with a moderate number of measurement lines indicates the practical applicability of FBP, catering to scenarios where a reduction of time and workload is crucial. OLS demonstrated the necessity of a 5x5 mesh and a higher number of measurements, with the required number of iterations varying across models. SIRT also performed optimally with a 5x5 mesh and 150 lines, with the number of iterations consistently improving with higher values. ART yielded better results with a 5x5 mesh, varying the number of measurement lines between medium and high, and setting iterations as 100 in most cases.

In the subsequent section, where images of experimental models are presented, the parameter configurations are determined based on the results of these numerical analyses summarized in Table 5.1.

Table 5.1 – Best combination of Mesh-Number of Measurements-Number of Iterations for each model and image reconstruction technique and ICC values

	Model 01	Model 02	Model 03	Model 04	Model 05	Model 06	Model 07	Model 08
OLS	5-150-1000	5-150-20	5-150-20	10-150-100	5-150-20	5-96-20	5-601-20	**5-601-1000**
ICC	0.781	0.730	0.486	0.678	0.728	0.410	0.617	**0.769**
SIRT	5-150-1000	5-150-1000	5-150-1000	10-150-1000	5-96-1000	5-150-1000	5-601-1000	5-601-1000
ICC	0.325	0.451	0.418	0.620	0.498	0.407	0.646	0.738
ART	5-150-10	5-96-100	5-54-100	5-150-20	5-96-100	5-96-1000	5-601-20	5-207-100
ICC	0.370	0.484	0.396	0.397	0.674	0.371	0.612	0.581
FBP	**10-96-20**	**10-96-20**	**10-96-20**	**10-96-10**	**10-96-20**	**10-96-20**	**10-601-10**	10-601-20
ICC	**0.830**	**0.841**	**0.862**	**0.679**	**0.829**	**0.831**	**0.854**	0.579

Source: the author.

Images reconstructed from simulated models using the best parameter combinations presented in Table 5.1 are shown in Figure 5.4. A noteworthy observation in all images is that

almost all of them accurately depict the damage with precise location. However, FBP achieves better size and shape definition. Mesh definition contributes to shaping, but since OLS, SIRT, and ART encounter challenges in generating images with denser meshes, they exhibit shape-related issues in their reconstructions. An essential consideration is that the selection of an appropriate mesh is contingent upon the number of measurement lines, and algebraic techniques may fail to reconstruct images if this choice is not suitable.

Figure 5.4 – Models (a) and images reconstructed with best combination of mesh and number of measurements: OLS (b), SIRT (c), ART (d), and FBP (e)

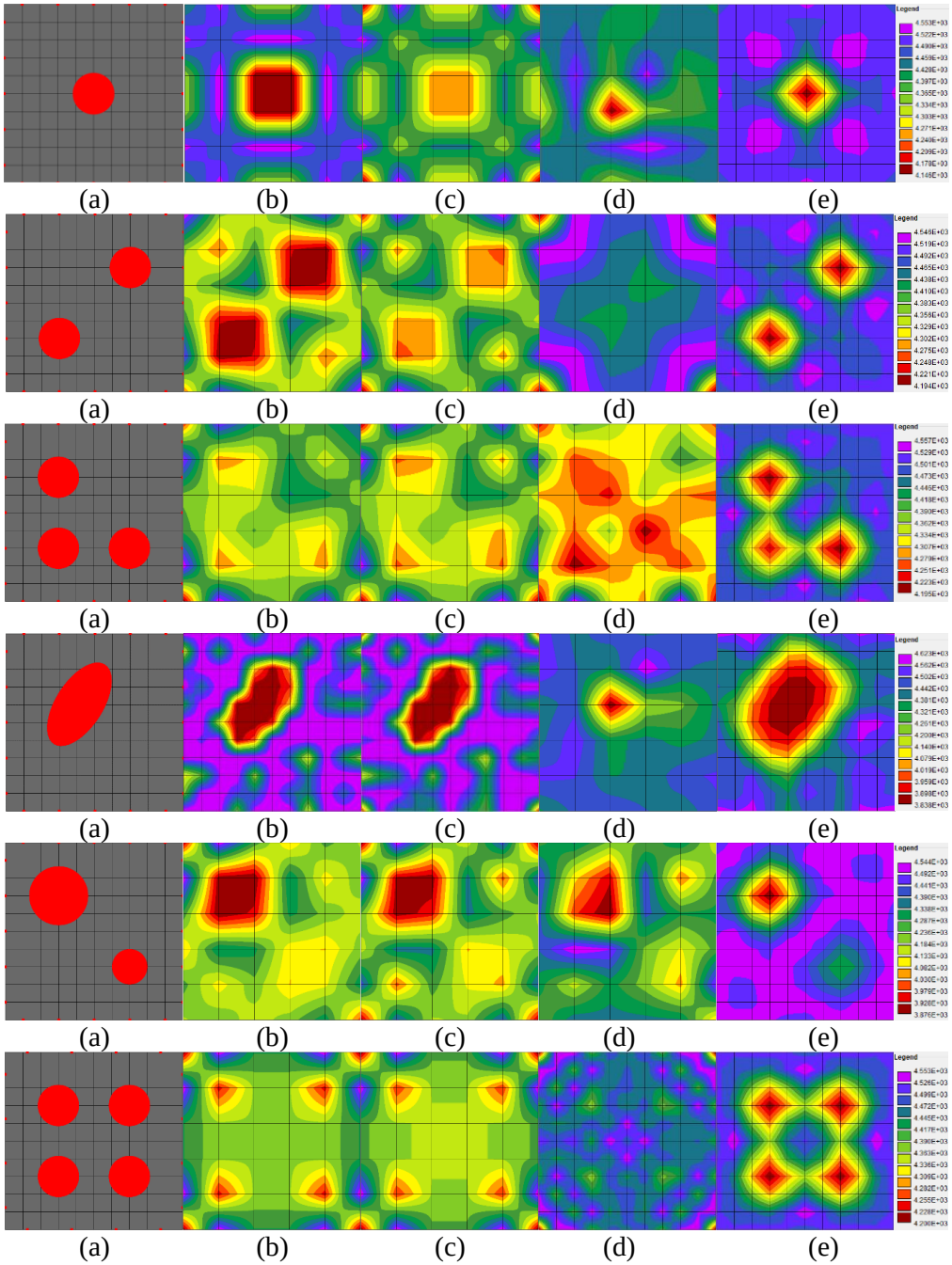

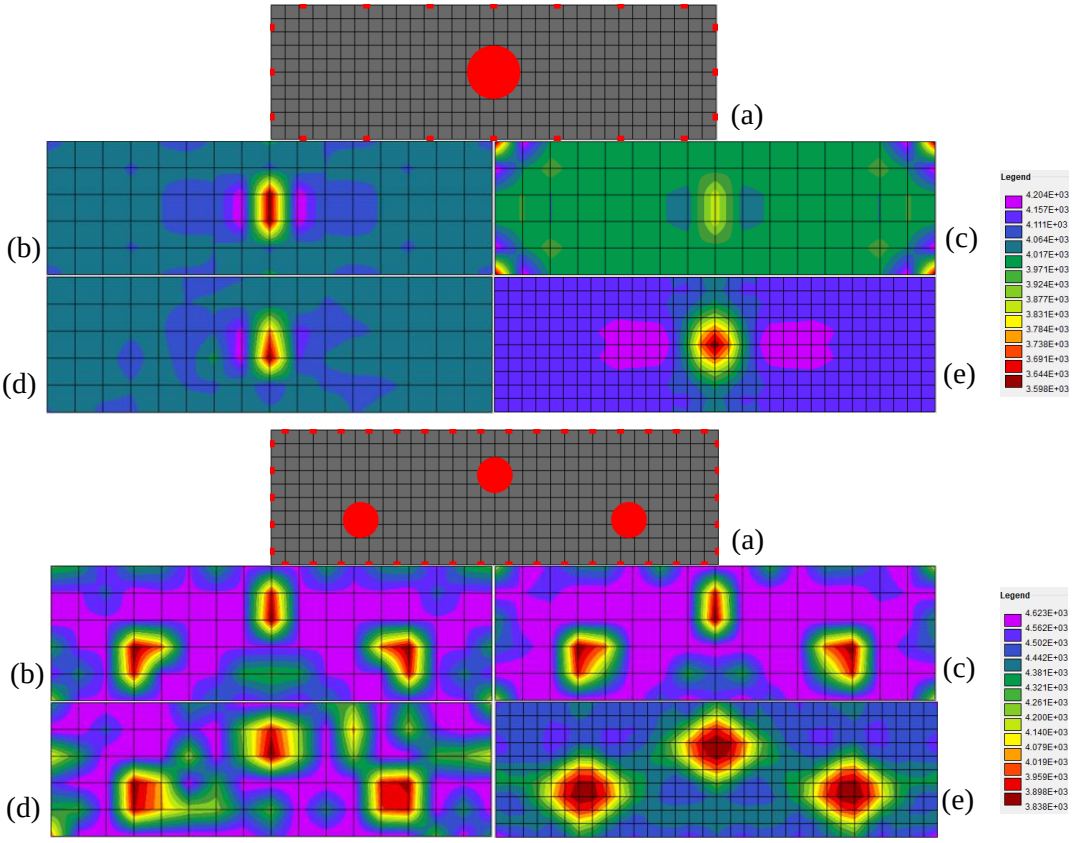

Source: the author.

Figure 5.5 is presented to showcase the performance of FBP for a 20x20 mesh, where ICC values were not the highest. Surprisingly, even with lower ICC values compared to images generated with a 10x10 mesh, visually, the images were more accurate.

Figure 5.5 – Image reconstruction with FBP, mesh defined as 20x20 and 150 measurement lines

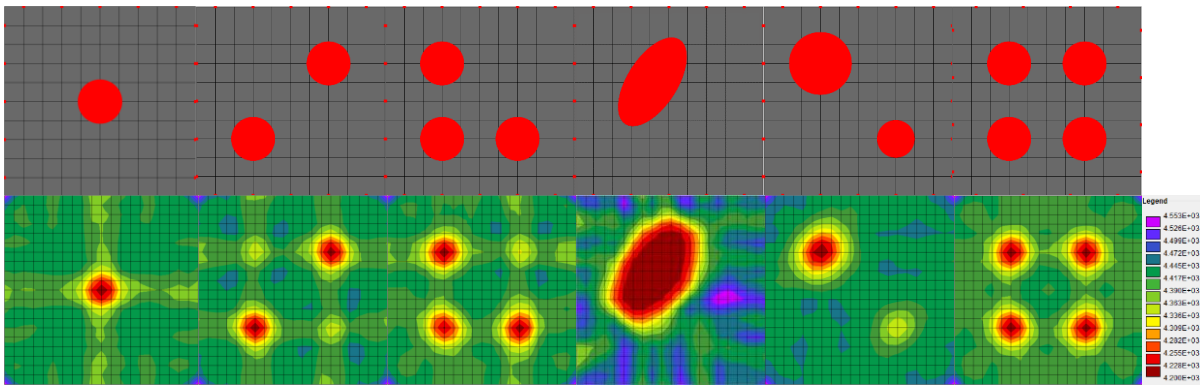

Source: the author.

This FBP performance can be explained by the properties of ICC formula, which compares image parameters such as attenuation or velocity coefficients calculated by the technique. With a 20x20 mesh, the FBP reconstruction depicted sound concrete with nodal velocities deviating

from the model-defined 4500 m/s, resulting in a decline in ICC. However, it is evident that FBP can produce highly accurate images, even when the ratio between measurement lines and nodes is less than 1 (150 lines and 441 nodes, resulting in a ratio of 0.34).

5.3 IDW interpolation of measurement lines with GA optimization

IDW interpolation was adopted to augment the number of measurement lines and incorporate additional data for image reconstruction. The parameters of this interpolation technique – specifically, the number of new points to generate new lines, weight, and the number of known measurement lines to add data during interpolation – were optimized using the implemented genetic algorithm. The use of GA enabled the identification of the best parameter combination, resulting in images with minimal variance between calculated nodal velocity and velocity at every measurement line near the node. Figure 5.6 illustrates the performance of GA across generations. It is evident that the most accurate interpolation was achieved for Model 01 (variation coefficient: 0.37), followed by Model 07 (variation coefficient: 0.43) – both being the simplest examples of a cube with central damage and rectangular prisms with central damage. Notably, the interpolation of measurements in Model 08 did not exhibit high accuracy, as the variation coefficient remained higher than 10 even after optimization. However, it is evident that the GA optimization successfully decreased the variance, thus efficiently optimizing the IDW parameters and reducing the error associated with interpolating measurements using IDW.

Figure 5.6 – GA average performance for IDW parameters optimization in each model

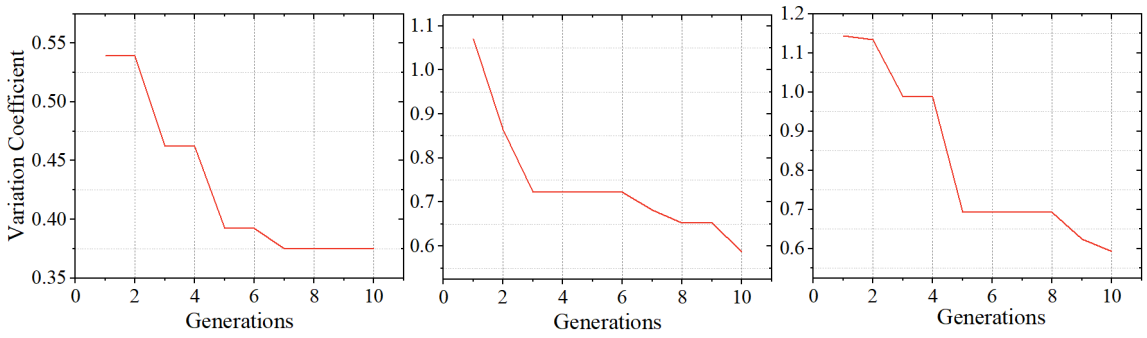

Model 01 Model 02 Model 03

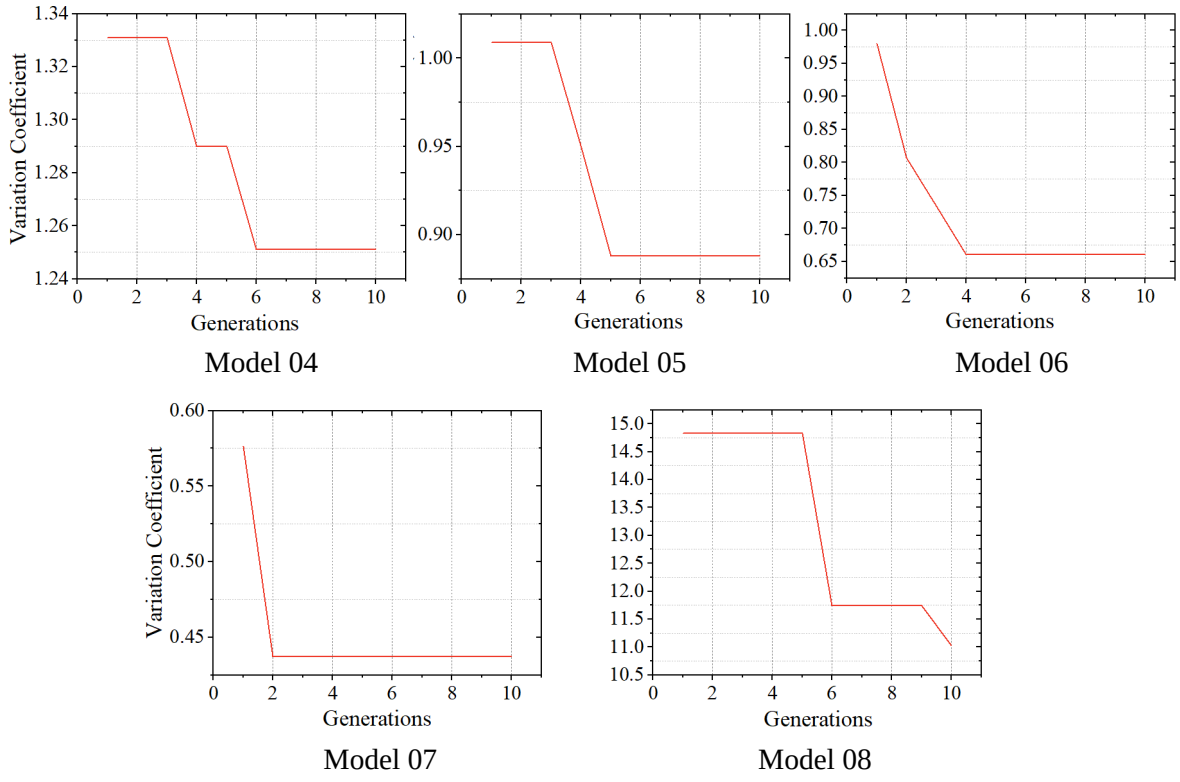

Source: the author.

After configuring the parameters as determined by the genetic algorithm, new measurement lines are created, and this updated set of measurement lines is utilized for image generation. Figure 5.7 displays the before-and-after comparison of measurements in Models 01 and 07, respectively. It is crucial to note that, as demonstrated for Models 01 and 07, all interpolations were executed from the maximum number of measurements proposed for each specimen geometry (150 lines for cubes and 601 for rectangular prisms).

Figure 5.7 – Measurement interpolation: a) real 150 measures; b) real + 864 interpolated measures; c) real 601 measures; d) real + 4329 interpolated measures

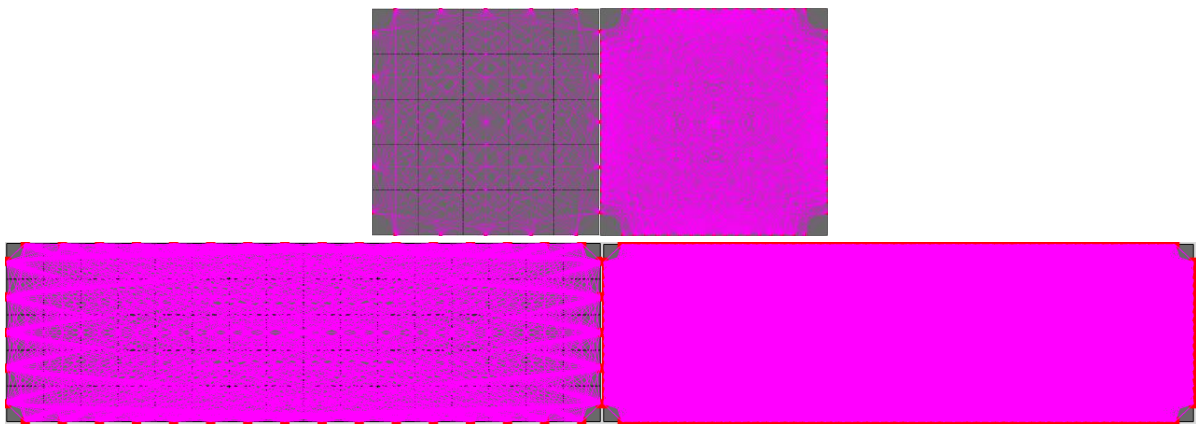

Source: the author.

To assess the precision of the IDW response after interpolating TOF for each new measurement line, graphs were generated for the interpolation of measurements of models 01 and 02 (see Figure 5.8). These graphs illustrate the expected TOF after interpolation by presenting the simulated TOF values for the same new interpolated measurements. A strong correlation is observed between the expected and obtained TOF. In Model 01, some issues begin to arise for TOF values greater than 30 µs, and in Model 02, issues emerge for TOF values exceeding 25 µs. The error in higher TOF values can be attributed to voids, which increase the TOF of an ultrasound wave. This also explains the greater error in Model 02, which has a larger void area. The MSE for the interpolation of Model 01 is 0.12, while for Model 02 is 0.29.

Figure 5.8 – Performance of IDW interpolation of 864 new measurement lines in Models 01 (left) and 02 (right)

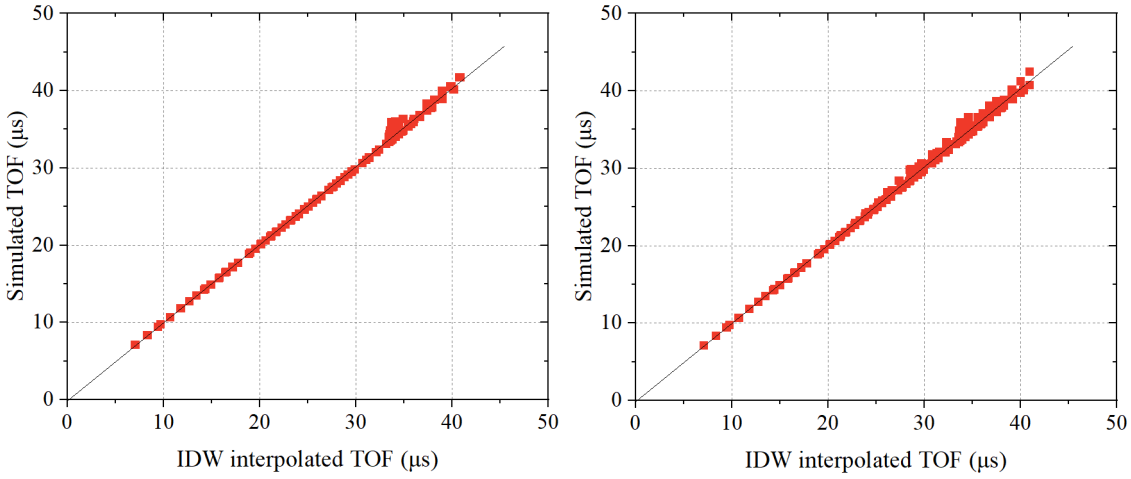

Source: the author.

After interpolating measurements, images were reconstructed using OLS, SIRT, ART, BP, and FBP, and then compared with images generated with the regular number of measurements. It is important to note that for image reconstruction, the best parameter combination (such as mesh, technique, and the number of iterations) was determined based on the analysis presented in section 5.2. The mesh was set as 5x5 for OLS, SIRT, and ART, and as 10x10 for FBP and BP. The number of iterations was set at 1000 for OLS and SIRT, 100 for ART, and 1 for FBP and BP. Figure 5.9 displays the ICC for images reconstructed for models 01 and 02 with regular and interpolated measurement lines. It is evident that, in all cases, the interpolation of measurements reduced the accuracy of images by decreasing the ICC. Additionally, it can be observed that the reduction in ICC is more significant with interpolated data in Model 02, which has a larger MSE when interpolating data.

Figure 5.9 – Comparison of ICC results of images reconstructed of Model 01 (left) and Model 02 (right) with regular lines and with IDW interpolated lines

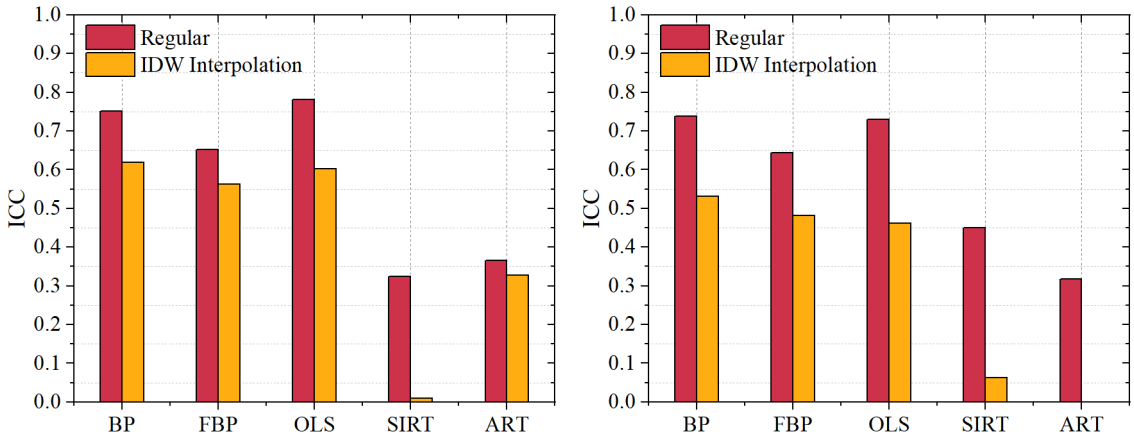

Source: the author.

Figure 5.10 – Reconstructions of Model 01 with OLS, SIRT, ART, and FBP before and after IDW measurement lines interpolation and comparison with total simulated lines

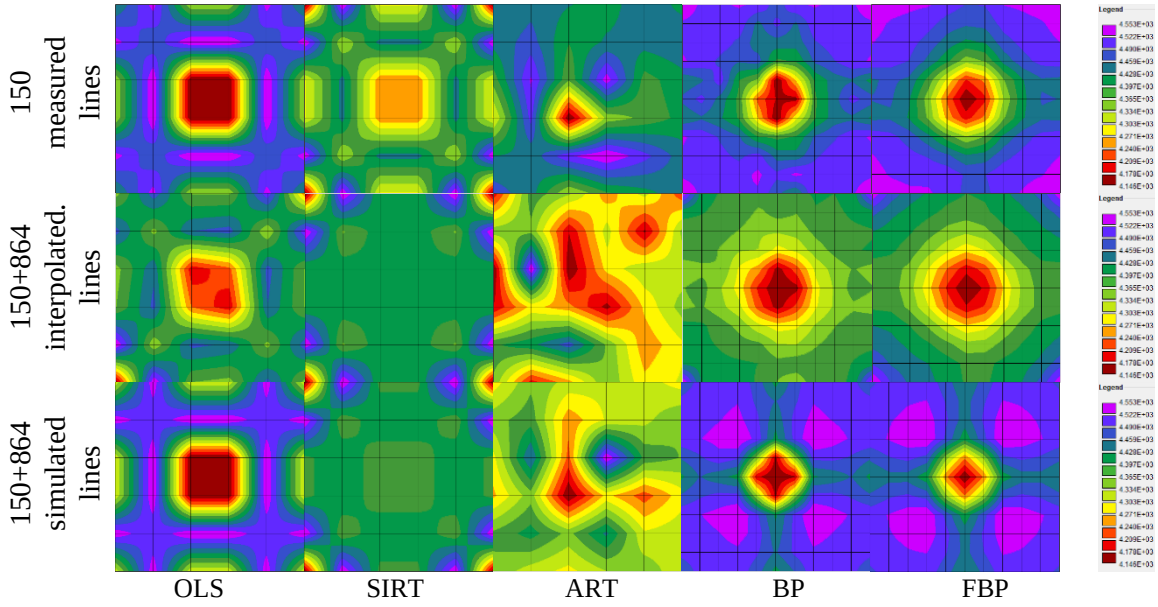

Source: the author.

Upon examining the images presented in Figure 5.10 and Figure 5.11, it becomes evident that the images least affected by interpolation were those reconstructed using the FBP and BP techniques. A notable observation arises when comparing the images generated with 150 simulated + 896 interpolated data points against those generated with 150 + 896 simulated data points in Figure 5.10. It appears that an increase in the number of data points does not necessarily lead to convergence to a better image, and this phenomenon is likely attributed to

the mesh configuration. Thus, it is apparent that the issue does not solely stem from the IDW interpolation method. Interestingly, both BP and FBP benefit from an increased set of measurement lines, as evidenced by an 12% increase in the ICC when reconstructing model 01 with an additional 896 simulated data points using BP and an 19% increase using FBP. In contrast, incorporating more simulated data reduced the image ICC by 13% with OLS, 75% with SIRT, and 61% with ART. Consequently, the IDW interpolation analysis will be extended to other simulated models exclusively for BP and FBP reconstructions.

Figure 5.11 – Reconstructions of Model 02 with OLS, SIRT, ART, and FBP before and after IDW measurement lines interpolation

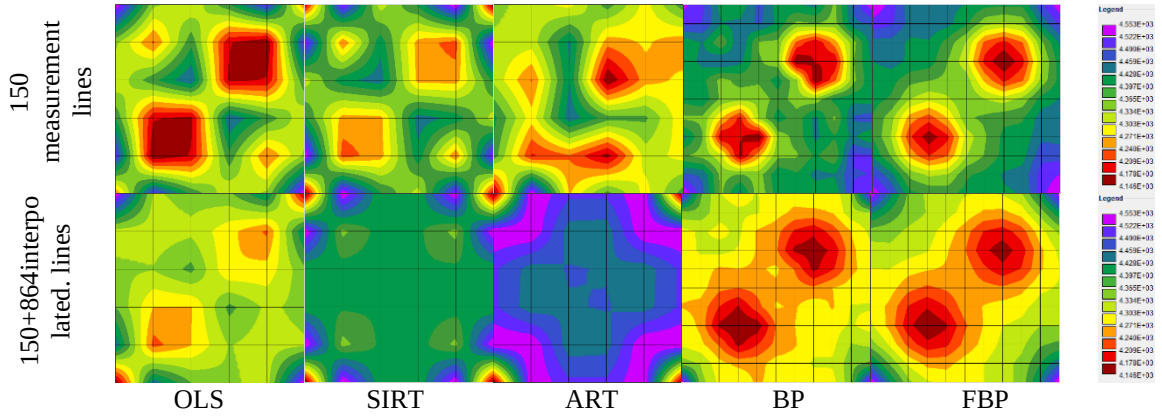

Source: the author.

Figure 5.12 – Comparison of ICC results of images reconstructed of Models 03 to 08 with and without IDW measurement lines interpolation

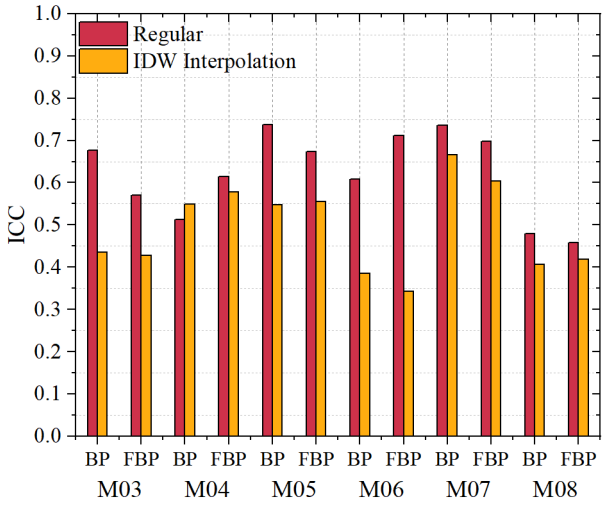

Source: the author.

Models 03 to 08 were reconstructed using FBP and BP techniques after measurement interpolation and compared with images generated with the regular number of measurements (Figure 5.12). The parameter configuration for image reconstruction was consistent: 10x10 mesh and 1 iteration. After completing all the tests, the only model that exhibited an enhancement in the image with interpolated measurements was Model 04, employing BP as the reconstruction technique (see images at Figure 5.13). Models 07 and 08 were the least impacted, experiencing an average decrease in ICC of 12% for BP reconstructions and 9% for FBP reconstructions. In all other instances, interpolation resulted in a higher average decrease in ICC (24% for BP reconstructions and 21% for FBP reconstructions).

Despite not achieving higher ICC, IDW interpolation performed well in terms of maintaining the characteristics of images. By examining Figure 5.13, featuring all images reconstructed with BP, and Figure 5.14, displaying images reconstructed with FBP, it is evident that the damaged area can still be identified even after interpolation. This suggests that IDW interpolation can be adopted in other circumstances where increased number of data is necessary for reconstructing images. In the next subsection 5.6, an approach to reconstruct images with a reduced number of measurement lines is presented, and IDW interpolation is adopted.

Figure 5.13 – BP reconstructions of models 03 to 08 with a standard number of measurement lines (top) and IDW-interpolated measurement lines (bottom)

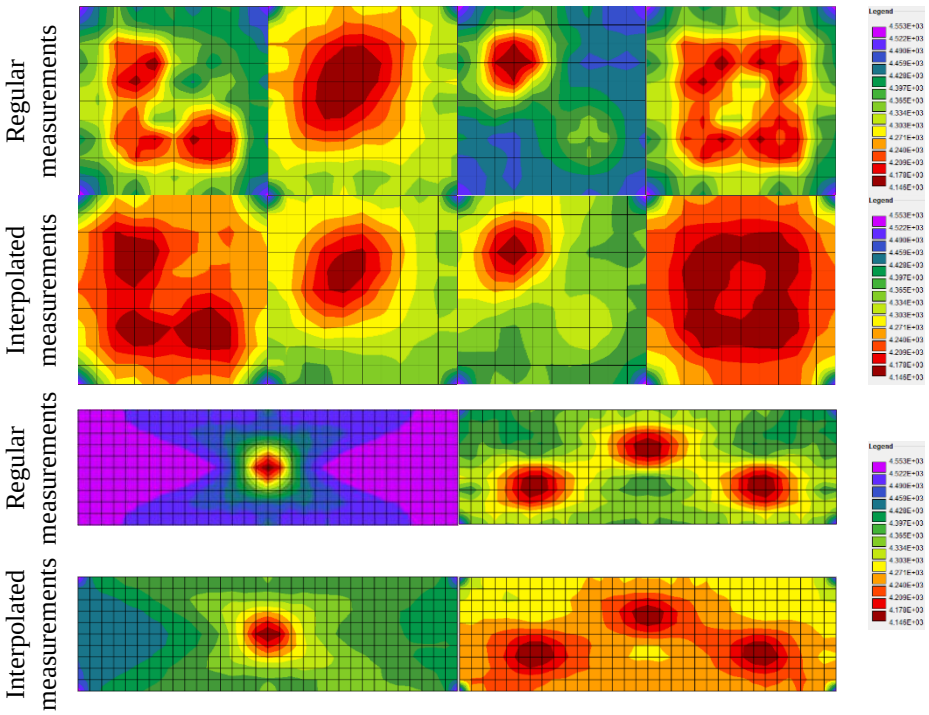

Source: the author.

Figure 5.14 – FBP reconstructions of models 03 to 08 with a standard number of measurement lines (top) and IDW-interpolated measurement lines (bottom)

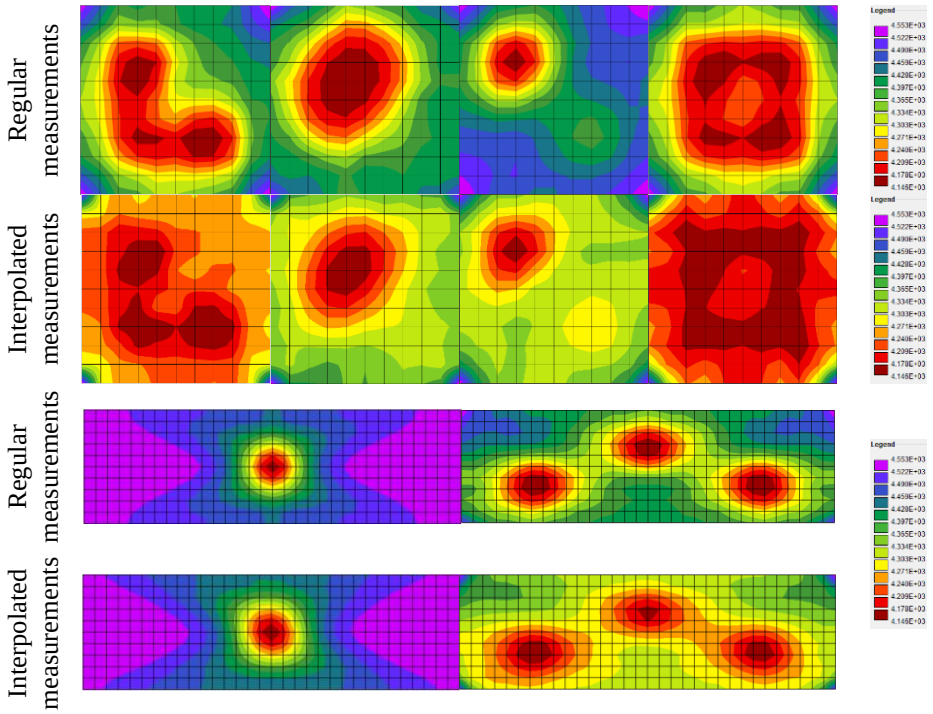

Source: the author.

5.4 ANN interpolation of measurement lines with GA optimization

ANN interpolation was adopted to increase the number of measurement lines and incorporate more data for image reconstruction, similar to IDW interpolation. The training dataset consisted of TOF values from 150 measurement lines. The ANN structure, including the number of layers, nodes per layer, and the number of epochs, was optimized using the implemented genetic algorithm. Initially, the study focused on two models due to the processing time required for GA+ANN. If satisfactory results were achieved, the analysis would be expanded to other models.

Figure 5.15 illustrates the GA performance across generations for the studied models 01 and 02. With the optimization of ANN parameters, the achieved minimum MSE for both models was similar. An important observation is that the fitness function did not exhibit a consistently descending behavior across generations. The training MSE increased at certain points, which may be attributed to the random initialization of weights and biases in each run, potentially rendering unnecessary the maintenance of two elite individuals across GA epochs. Nevertheless, with GA, it was possible to find the global minimum for ANN parameters to achieve the best results in the reconstructed images with interpolated measurements. This

optimal combination, with the minimum variation coefficient, had weights and biases saved after training for measurements interpolation. Model 01 was configured with 2 hidden layers of 17 and 20 nodes and 5802 epochs, while Model 02 was configured with 1 hidden layer of 15 nodes and 9000 epochs. The MSE achieved after training with the best parameters were 4.99×10^{-4} for Model 01 and 5.23×10^{-4} for Model 02, as shown in Figure 5.16. Even with the best parameters, it was not possible to achieve an MSE lower than 10^{-5}.

Figure 5.15 – GA average performance for ANN parameters optimization for Models 01 (left) and 02 (right)

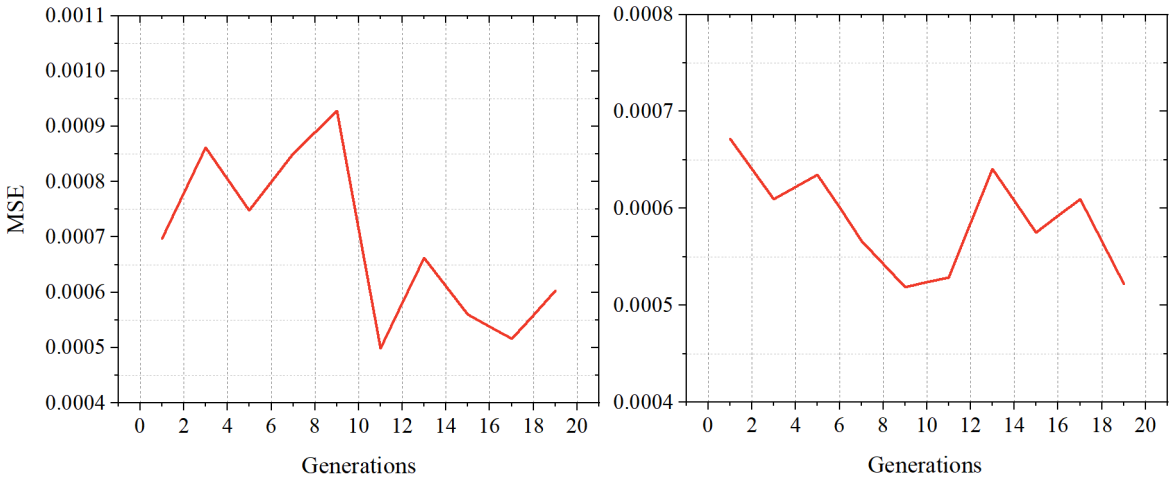

Source: the author.

Figure 5.16 – MSE during ANN training of Model 01 (left) and Model 02 (right)

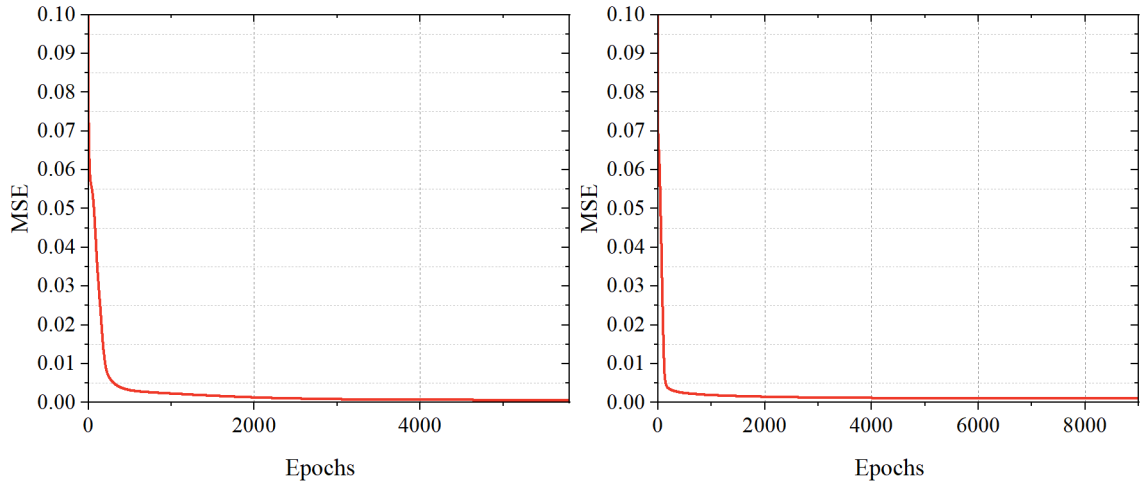

Source: the author.

To provide a clearer visualization of the training and testing data for this ANN interpolation on models 01 and 02, graphics illustrating the relationship between expected and predicted values were developed and are presented in Figure 5.17 and Figure 5.18. When comparing the

results with ANN (Figure 5.17 and Figure 5.18) to those with IDW (Figure 5.8), it is noticeable that ANN interpolated results have higher variance between simulated and interpolated values, possibly introducing a significant impact on the images. The standard deviation of regular training data (considering the known TOF of 150 measurement lines) is 8.01 in Model 01 and 8.11 in Model 02. During ANN testing stage, the maximum error between a new interpolated measurement line and the expected value is 4.19 in Model 01 and 4.25 in Model 02. This implies that this error is more than half of the deviation existing between regular data. Consequently, this error can significantly impact the final reconstructed image and, in some cases, alter the image completely. This can be observed in Figure 5.19 and Figure 5.20.

Figure 5.17 – Training performance of ANN with 150 measurement lines as input from Models 01 (left) and 02 (right)

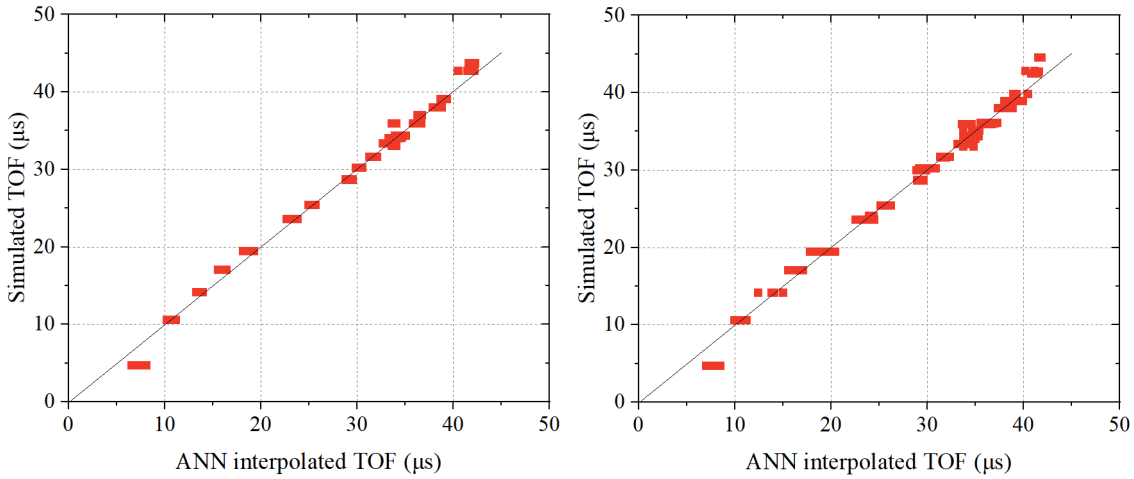

Source: the author.

Figure 5.18 – Testing performance of 96 interpolated measurement lines with ANN for Models 01 (left) and 02 (right)

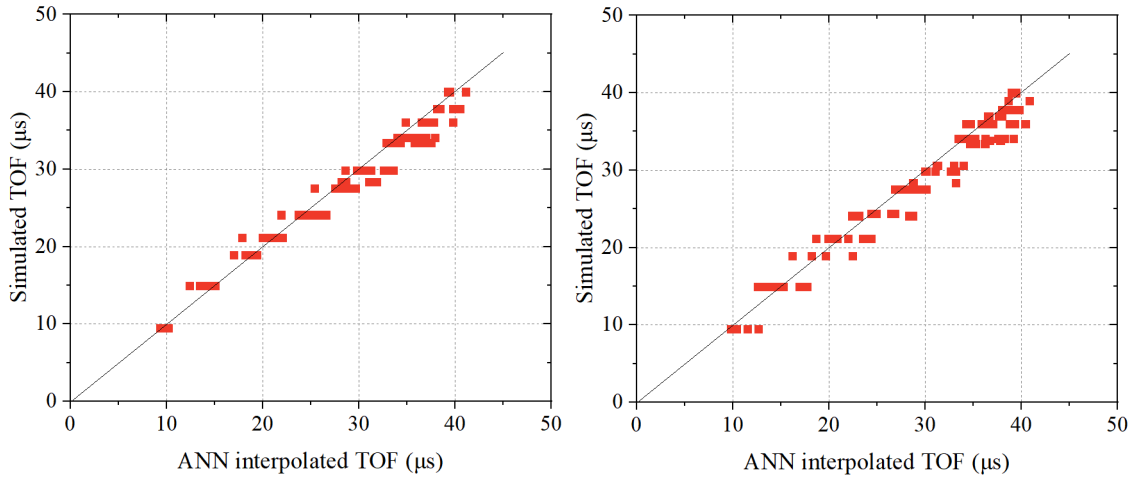

Source: the author.

Although the ANN interpolation did not yield favorable results in this study, it is important to highlight the potential predictive capabilities of the neural network, even with a limited dataset of 150 measurement lines. This suggests that, with further improvements such as a more sophisticated network architecture, new training parameters, and implementation in a more advanced programming language (since it was programmed in Pascal), there is potential for successfully employing the proposed idea.

Figure 5.19 – Reconstructions of Model 01 with OLS, SIRT, ART, and FBP before and after ANN measurement lines interpolation

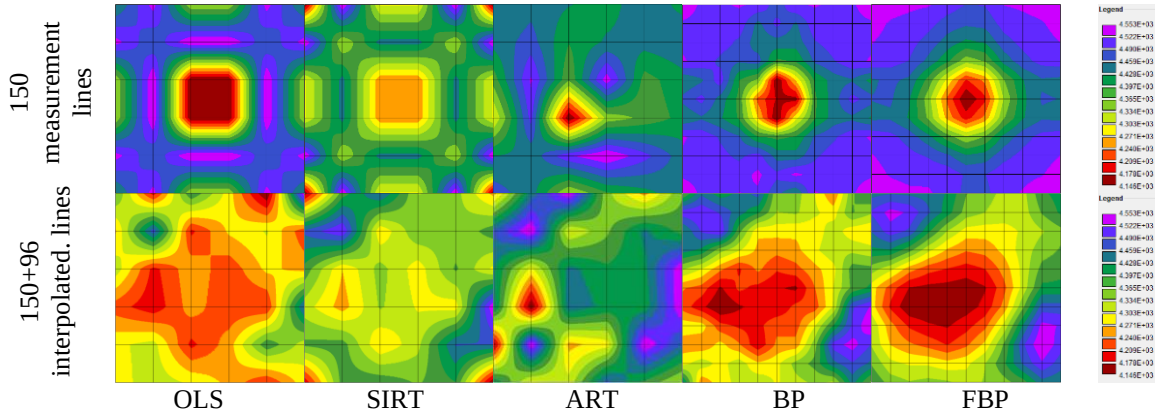

Figure 5.20 – Reconstructions of Model 02 with OLS, SIRT, ART, and FBP before and after ANN measurement lines interpolation

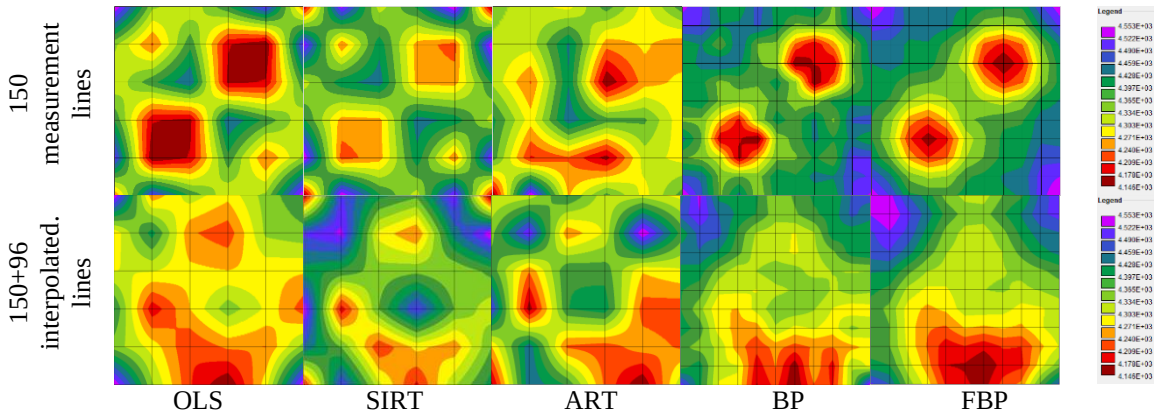

Source: the author.

5.5 Comparison between TOF and attenuation tomography: experimental models

After a wet cure for 28 days, the 5x10 cm³ cylinder specimens achieved compressive resistance values of 42.89 MPa for concrete batch of models 01 and 02, 29.08 MPa for models 03 and 04, and 35.82 MPa for models 05, 06, and 07. The consecutive p-wave velocities were

5006.80 m/s, 4868.57 m/s, and 4973.96 m/s and attenuation coefficients were 3.47 m^{-1}, 4.77 m^{-1}, and 4.75 m^{-1}. These attenuation values are below what was found by Chai *et al.* (2011), where it was reported that the attenuation coefficient of homogeneous concrete with a compressive strength of 29.1 MPa is 5.2316 m^{-1}. In the work of Camassa *et al.* (2020), however, the average attenuation coefficient of concrete was noted to be 4.17 m^{-1}.

All reconstructed images from experimental specimens were evaluated using the methodology of confusion matrix. Figure 5.21 illustrates how the true and false damaged areas are highlighted with the code written in MATLAB® to compare areas between the real expected image and the reconstructed one for Model 01. Table 5.2 presents the accuracy, positive, and negative precision for the reconstructions of Model 01. It can be observed that positive prediction shows no significant difference, indicating that all methods could classify positive regions very precisely. This behavior was consistent across all other models and for this reason positive prediction values will not be used for comparative purposes. On the other hand, accuracy achieved with all reconstructions exhibits slight differences, which can be utilized to classify image reconstruction techniques. For Model 01, FBP achieved the best accuracy, indicating that the position and shape of reconstructed damages were closer to the real damage in the model.

Figure 5.21 – Matrix confusion analysis of Model 01 reconstructed with FBP

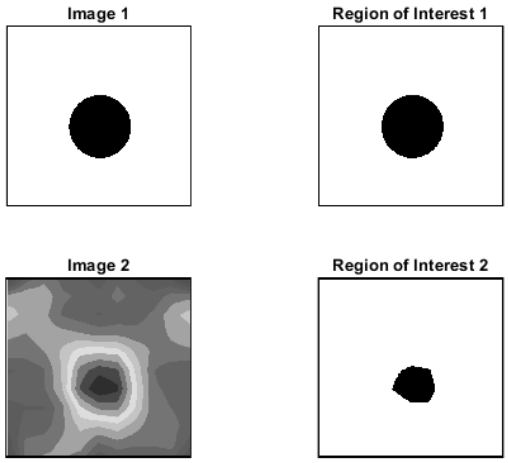

Source: the author.

The accuracy of reconstruction for all other models is presented in Figure 5.22 as “Acc” for attenuation and velocity reconstructed tomograms. The best accuracy is generally achieved with FBP in most models, and the behavior is similar for attenuation and velocity tomograms. However, in Model 07, the best accuracy is achieved with algebraic methods (OLS, SIRT, and

ART), which correlates with the findings in the numerical analysis: FBP achieves poor resolution when dealing with rectangular specimens.

Table 5.2 – Model 01 confusion matrix results

	OLS		SIRT		ART		FBP	
	Velocity	Attenuation	Velocity	Attenuation	Velocity	Attenuation	Velocity	Attenuation
Accuracy	0.8747	0.8841	0.8779	0.8863	0.8755	0.8908	0.9498	0.9541
Positive precision	0.9913	0.9929	0.9907	0.9928	0.9917	0.993	1	0.9984
Negative precision	0.1734	0.2306	0.1996	0.167	0.177	0.2763	0.6481	0.6882

Source: the author.

Negative precision (Np) is the confusion matrix result that revealed the most significant difference between values. In general, Np did not achieve high values, indicating that areas were reconstructed as non-damaged when, in fact, they were damaged, for all image reconstruction techniques. Very low results were obtained with algebraic techniques, with the highest values being achieved by SIRT in Model 03 (Np = 0.32). On the other hand, FBP achieved significantly higher values compared to those achieved with algebraic methods, with the average percentage difference being FBP achieving Np 36% higher than algebraic methods.

Another important analysis is correlated to the comparison between attenuation and velocity tomograms. In models 01, 05, and 07, the attenuation tomogram exhibited a better behavior with higher Np, while in models 02, 03, 04, and 06, velocity tomograms had the best Np. It is noteworthy that in the rectangular specimen (Model 07), attenuation tomography was sensitive enough to achieve an Np of 0.79, while velocity tomography presented an Np of 0.2.

Figure 5.22 – Accuracy and Negative Prediction results for OLS, SIRT, ART, and FBP reconstructions of Models 01 to 07

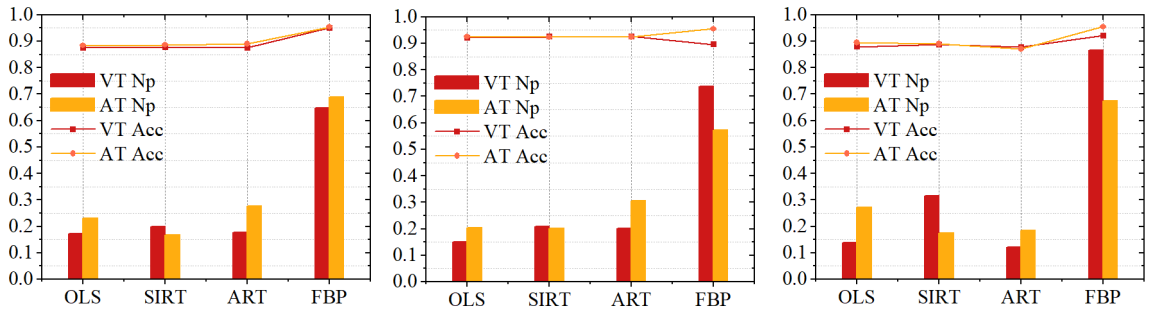

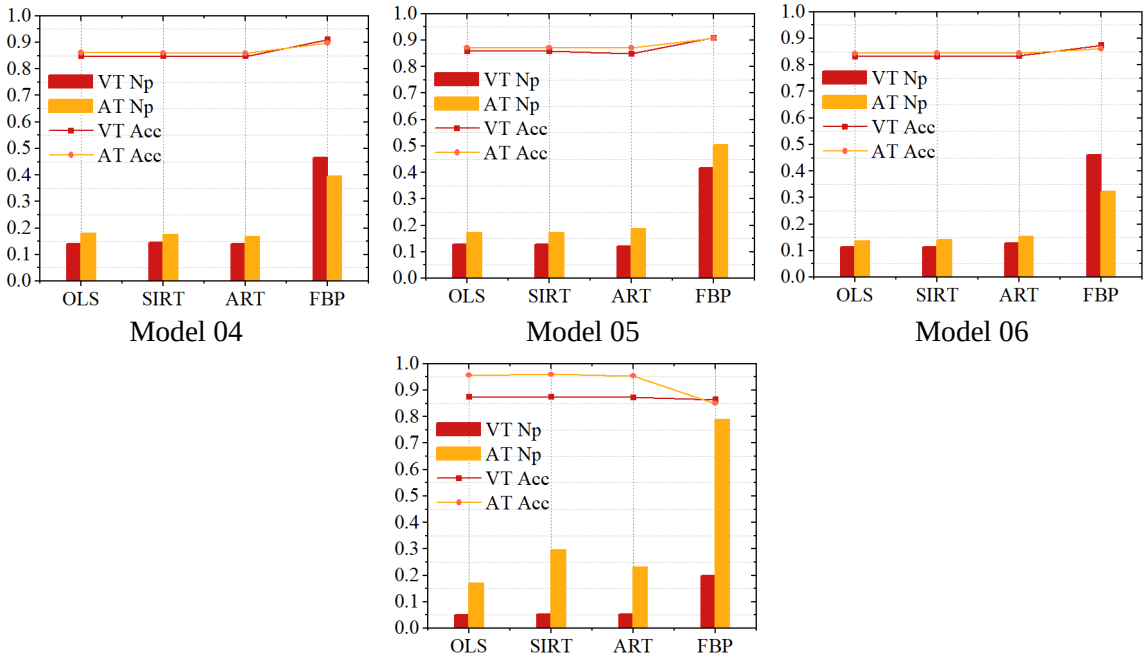

Source: the author.

Considering that the behavior between attenuation and velocity tomography varied in cube specimens, it is not possible to definitively say which one is better. However, what can be observed is that they can complement each other in cases where it is not possible to be confident in the achieved response. In Model 07, for example, only the attenuation tomogram was able to show the exact location of the damage. This can be seen in Figure 5.23, where the reconstructed images from all models are displayed. Upon reviewing all images, it is evident that FBP consistently outperformed other techniques, as concluded from the matrix confusion results. FBP stands out in accurately identifying the location of damage through visual analysis (images represented by letter (e)). Images reconstructed from models 04 and 06, for instance, exhibit remarkable precision even with a mixed pattern of damage. Notably, these results are achieved despite the inherent challenges posed by experimental tests, which are susceptible to various errors related to natural heterogeneity of concrete, transducer coupling and location precision during the testing process.

Figure 5.23 – Models 01 to 07 (a) and images reconstructed (velocity and attenuation tomograms) with best combination of mesh and number of measurements: OLS (b), SIRT (c), ART (d), and FBP (e)

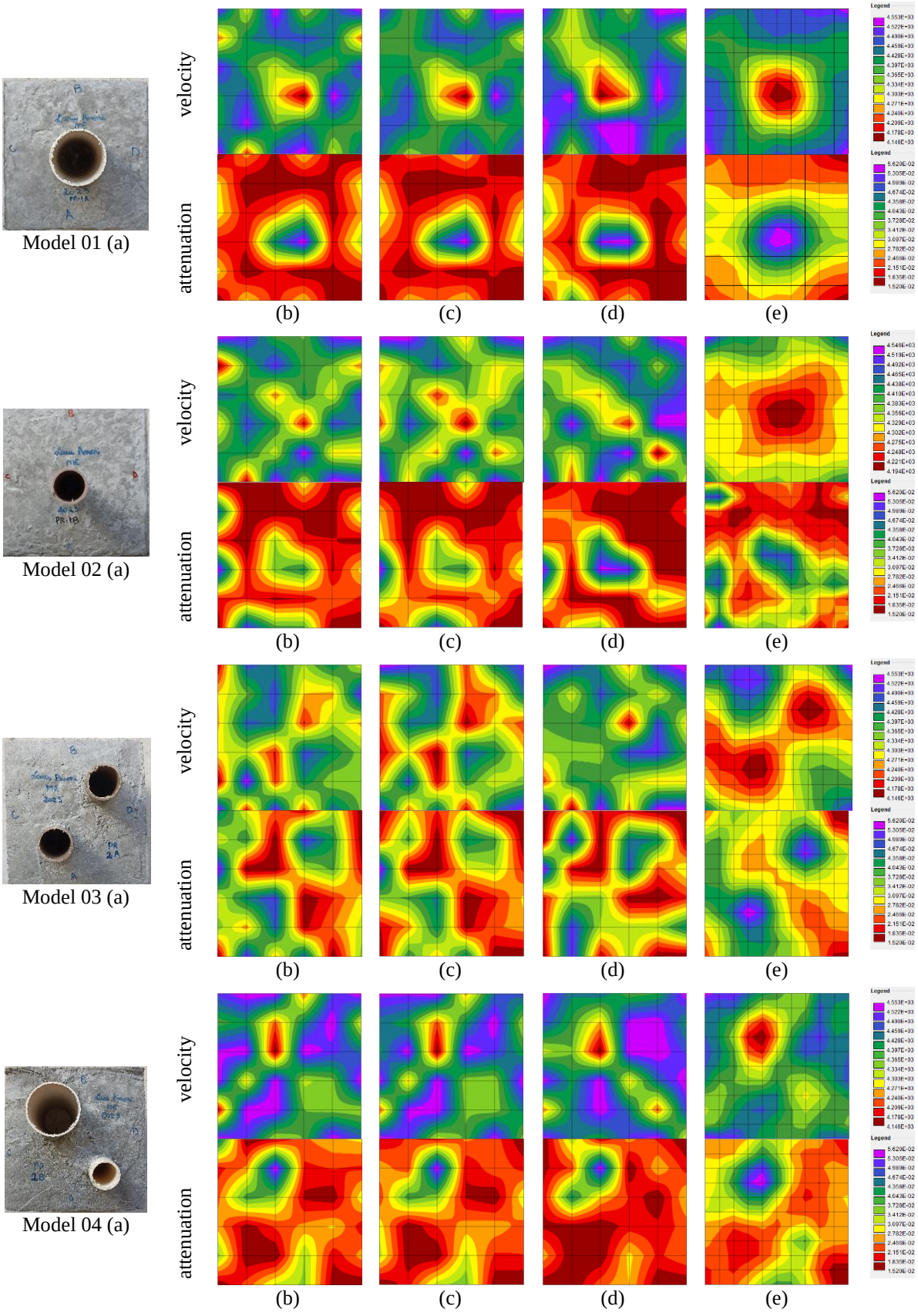

Model 05 (a)

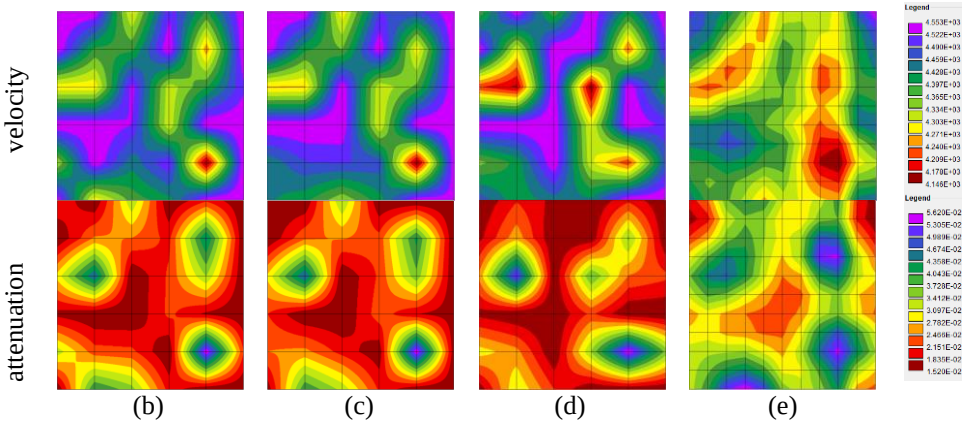

Model 06 (a)

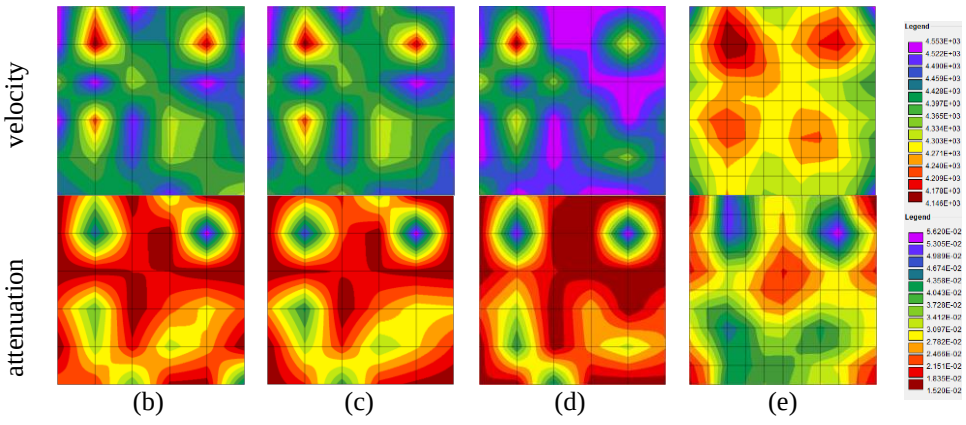

Model 07 (a)

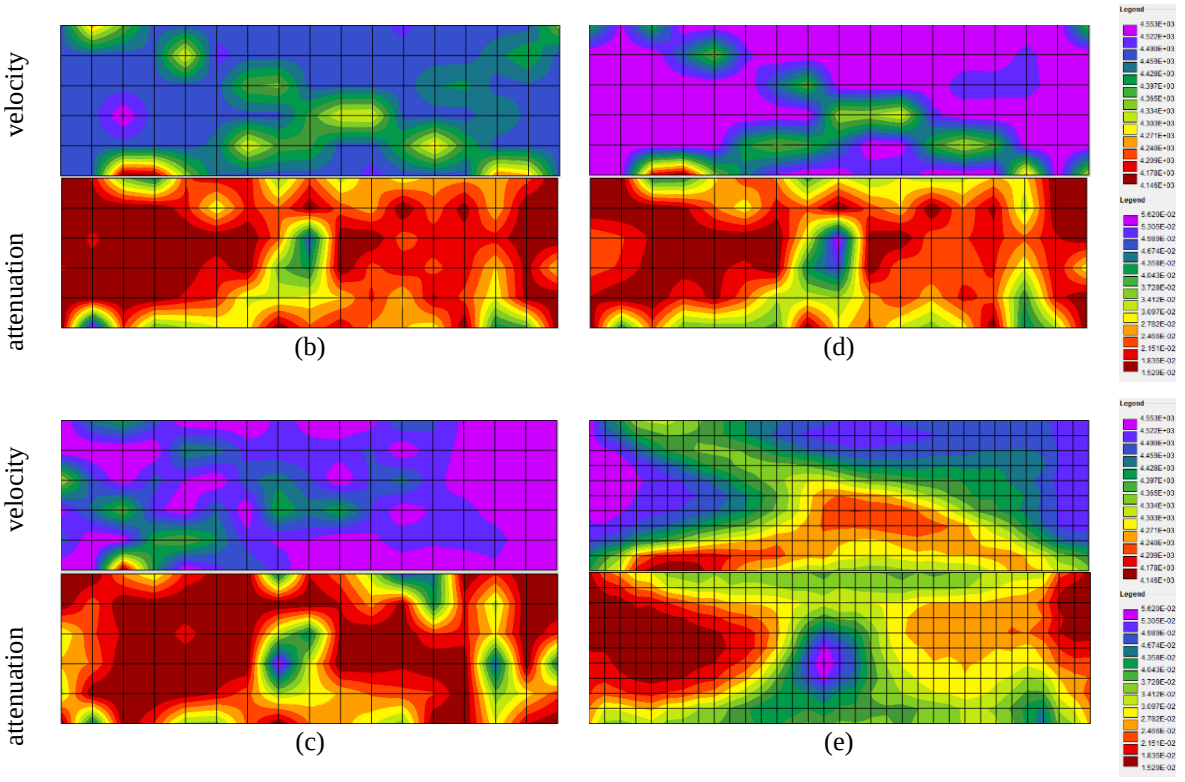

Source: the author.

After image reconstruction, the maximum and minimum range of nodal attenuation and velocity calculated with each reconstruction method were recorded. In theory, maximum velocity as well as minimum attenuation should represent areas of sound concrete. Conversely, minimum velocity as well as maximum attenuation should represent damages. However, due to physical reasons, voids are not represented as air velocity because the wave goes through the fastest path. This means the wave will only experience decreased velocity when encountering a void. Another factor is related to the reconstruction's parameters. Algebraic methods need constraints to converge, and these constraints affect the minimum and maximum values. For example, the minimum attenuation achieved was always 0 m^{-1} with algebraic methods, and the maximum velocity was always 5500 m/s, following the defined constraints. Consequently, the subsequent analysis of minimum and maximum nodal coefficients will specifically focus on FBP results.

Considering the p-wave velocity of produced concrete for models 01 and 02 (5006.80 m/s), the maximum velocity calculated with FBP after image reconstruction is 4874.58 m/s, and it is close to the expected value (see Table 5.4) with a deviation of ±2.6%. The maximum velocity of reconstructed models 03 and 04 shows a larger deviation, with more than 8.5%, and of models 05, 06, and 07, a deviation of more than 11.27%.

Table 5.3 – Maximum and minimum velocity results from reconstructed images (m/s)

	Model 01	Model 02	Model 03	Model 04	Model 05	Model 06	Model 07
OLS max. velocity	5500	5500	5500	5500	5500	5500	5500
OLS min. velocity	3431.5477	4176.2226	3802.7318	2361.15	3233.7668	3810.7667	1935.0224
SIRT max. velocity	5500	5500	5500	5500	5500	5500	5500
SIRT min. velocity	3443.5485	4344.3335	3994.2589	2404.4198	3174.4611	3830.3519	2591.6395
ART max. velocity	5500	5500	5500	5500	5500	5500	5500
ART min. velocity	3299.378	3944.0428	3566.5272	2245.2588	2970.9363	3512.9593	1422.4119
FBP max. velocity	4874.5788	5136.5808	4812.0215	5292.8539	5426.7908	5534.924	5486.694
FBP min. velocity	4447.8362	4857.0264	4530.0214	2950.9828	4168.5639	4509.1502	3845.1191

Source: the author.

To examine nodal attenuation values after image reconstruction, Table 5.4 was prepared. FBP attenuation's minimum value in Model 01 was 15.2 m^{-1} and in Model 02 was 0.9 m^{-1}. This represents a significant deviation from the attenuation of prepared cylinder specimens (3.47 m^{-}

[1]). Despite poor results for models 01 and 02, the reconstruction of other models achieved more precise values according to expectations. Models 03 and 04 had minimum attenuation of 5.70 m^{-1} and 8.80 m^{-1}, which is closer to the expected value of 4.77 m^{-1}. Also, models 05, 06, and 07 presented minimum attenuation as 4.00 m^{-1}, 6.10 m^{-1}, and 4.40 m^{-1}, respectively, and in this case, they are even closer to the expected attenuation of 4.75 m^{-1}.

It is interesting to note the maximum attenuation, which increases significantly in comparison to minimum values. In model 04, for example, the maximum attenuation is almost 14 times bigger than the minimum, which is caused by energy loss when reflecting in damages. The maximum attenuation values are higher than those found in Camassa et al. (2020), where the maximum was 6.4 m^{-1} and minimum was 2 m^{-1}, even in the cases the authors studied concrete specimens with voids. This can be related to the area of damage in proportion to the area of the studied object. In the studied concrete specimens presented in this work, the damaged area is larger. Additionally, the implementation of image reconstruction techniques and defined parameters in image reconstruction can influence the results.

Table 5.4 – Maximum and minimum attenuation results from reconstructed images (m^{-1})

	Model 01	Model 02	Model 03	Model 04	Model 05	Model 06	Model 07
OLS max. attenuation	163.10	95.80	89.80	185.10	141.40	137.50	95.70
OLS min. attenuation	0.00	0.00	0.00	0.00	0.00	0.00	0.00
SIRT max. attenuation	163.30	91.30	108.10	190.50	142.00	123.30	87.20
SIRT min. attenuation	0.00	0.00	0.00	0.00	0.00	0.00	0.00
ART max. attenuation	174.10	95.50	97.10	218.80	177.20	128.90	80.20
ART min. attenuation	0.00	0.00	0.00	0.00	0.00	0.00	0.00
FBP max. attenuation	56.20	71.80	68.20	123.10	65.90	61.40	41.50
FBP min. attenuation	15.20	0.90	5.70	8.80	4.00	6.10	4.40

Source: the author.

5.6 Proposed approach for reduction of time-intensive structural inspections

From a set of 4 measurements, as defined in Figure 5.24, a velocity tomogram of Model 01 was reconstructed using FBP. Subsequently, new points were added between the existing ones, and new measurement lines between them were generated with interpolated data. A new image with more data was then generated and compared to the previous one. It is observed that

interpolation did not improve the location of damages; in fact, it had the opposite effect, making the image further from reality.

Figure 5.24 – Strategic reconstruction of simulated Model 01 with the proposed approach

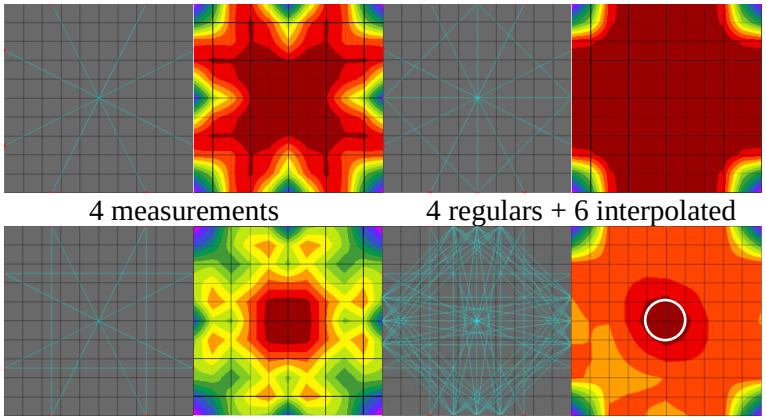

Source: the author.

After this initial iteration, a new iteration was performed by selecting new measurement lines with simulated TOF. Once again, an image was generated with this new regular number of measurements and with interpolated measurements, as depicted in Figure 5.24. In this instance, it became evident that after interpolation, the image was generated with the correct damage location (boundaries of damage outlined in white). This approach enabled image reconstruction with only 8 measurements around the object.

Figure 5.25 – Strategic reconstruction of simulated Model 02 with the proposed approach

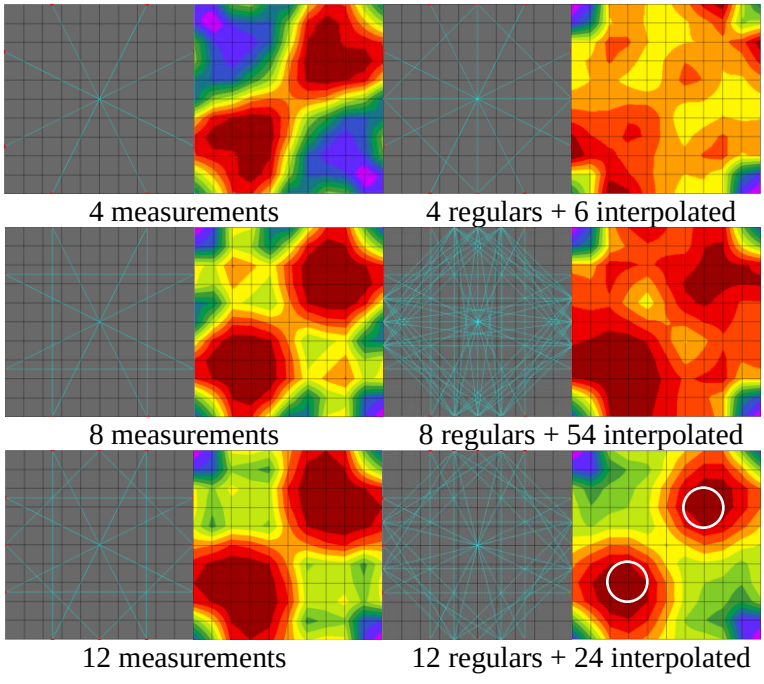

Source: the author.

Following the same idea demonstrated for simulated Model 01, Model 02 was studied. In this case, the number of iterations was set to 3, and IDW interpolation aided in the third one. By utilizing only 12 measurements around the section, it became feasible to create an image with reduced noise and enhanced precision (see Figure 5.25). This improvement can also be attributed to the efficacy of the genetic algorithm optimization in tuning the IDW parameters.

Figure 5.26 – Strategic velocity reconstruction of experimental Model 03 with the proposed approach

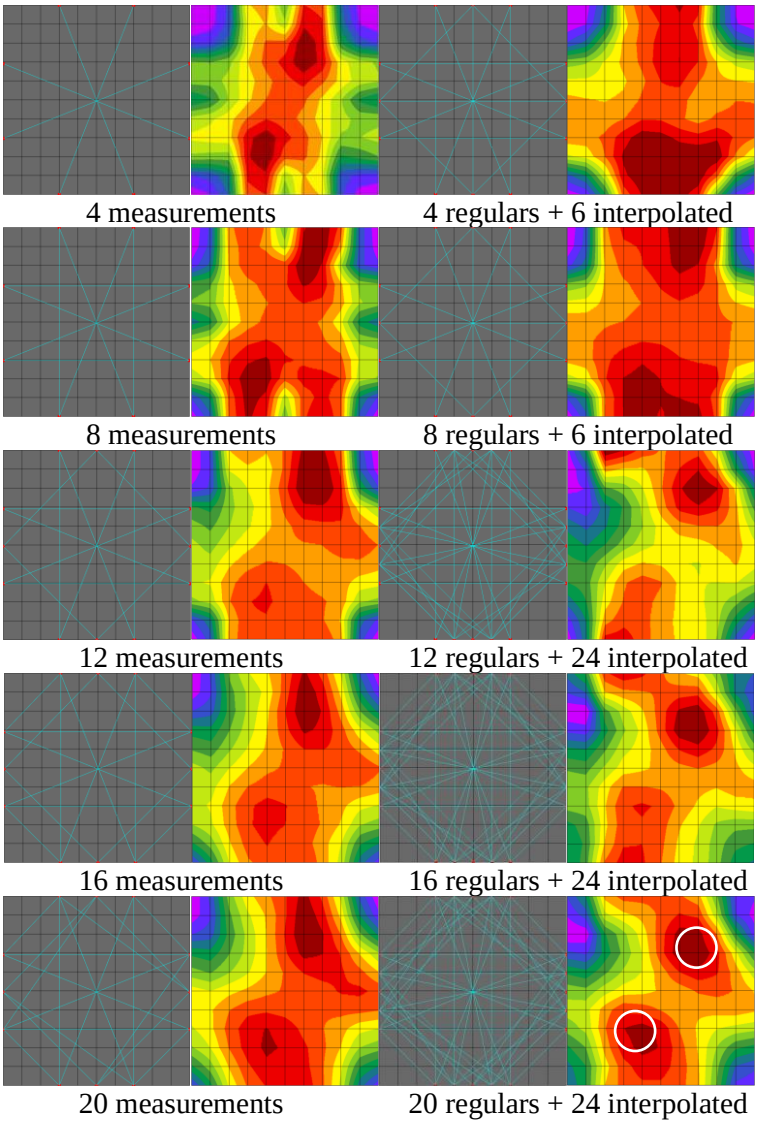

Source: the author.

The study was extended to experimental Model 03, which has the same damage shape as simulated Model 02. The necessary number of iterations was 5, and this increased number, compared to the previous example, is likely related to natural heterogeneity of concrete or test precision problems. Even with a higher number of iterations, only 20 measurements around the

section were necessary to generate a velocity tomogram with reduced noise and enhanced precision (see Figure 5.26). The same approach was employed to generate the attenuation tomography of experimental Model 03. The reconstructed images are presented in Figure 5.27. It is noticeable that after 3 iterations, the generated images bear little resemblance to the model, and this is probably due to the sensitivity of attenuation values. Thus, only a large number of lines with amplitude decay data can generate images. As this approach aims to demonstrate a way to reconstruct images with the lowest number of measurements, velocity tomograms are recommended.

Figure 5.27 – Strategic attenuation reconstruction of experimental Model 03 with the proposed approach

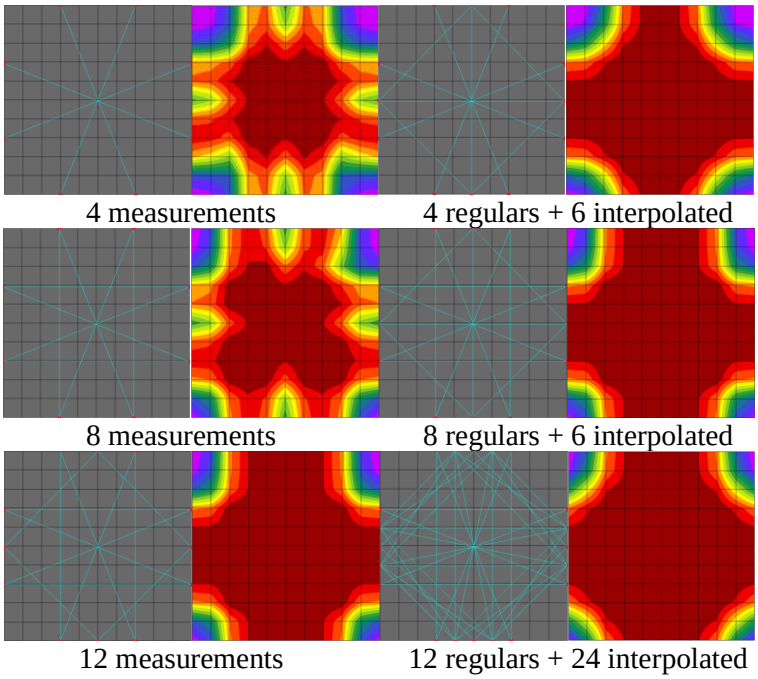

Source: the author.

5.7 Proposed approach for coupling techniques

In the previous section 5.2, it was shown that when the ratio between measurement lines and the number of mesh nodes was only equal to 2.67 or higher, it was possible to generate images with algebraic methods OLS, SIRT, and ART. On the other hand, FBP was able to reconstruct images with the number of measurement lines equal to 150 and mesh nodes equal to 441, which means a ratio equal to 0.34. Thus, FBP was used as an initial guess for algebraic methods in order to determine the correct solution for systems that have infinite solutions (150

linear equations and 441 variables). After the FBP initial guess, images of simulated models 01 to 06 were reconstructed with OLS, SIRT, and ART by changing the number of iterations (1, 10, 20, 100, 500, 1000). For the number of iterations that generated the best ICC values for each model, graphics were generated and are presented in Figure 5.28. It is possible to see that the most efficient combination was FBP + SIRT. Also, in some model reconstructions, FBP + SIRT showed better ICC compared to FBP ICC, which means this is a solution to improve accuracy.

Figure 5.28 – Comparative ICC achieved by algebraic techniques with FBP as initial guess

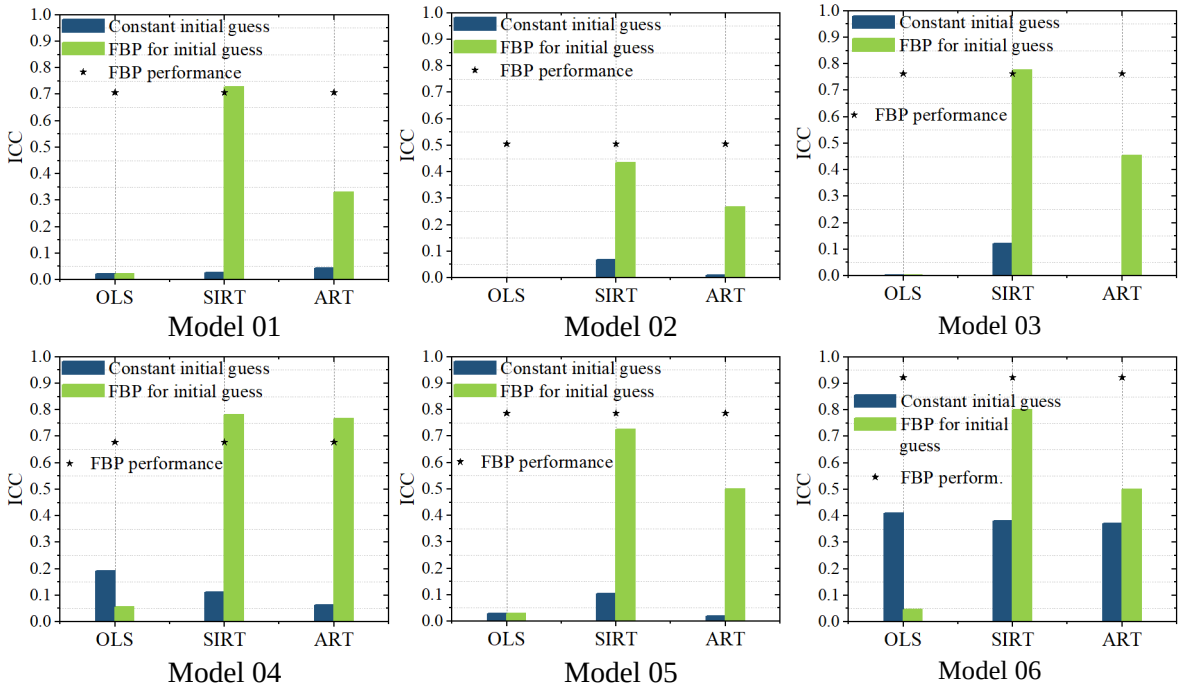

Source: the author.

Model 06 reconstructions are illustrated in Figure 5.29. As shown with ICC results, FBP + SIRT was the best solution to reconstruct images. OLS did not benefit from the FBP initial guess, and ART had performance increased significantly but not as much as SIRT. What is interesting is that only 20 iterations of FBP and 1 of SIRT were applied as image reconstruction parameters; no constraints were used in these simulations. For comparative analysis, images reconstructed with constant initial guess, a higher number of iterations, and constraints of minimum and maximum nodal velocities (100 m/s and 5500 m/s) are also presented in Figure 5.29. Due to positive results, this same approach was used to reconstruct experimental Model 06, which has the same number of voids. SIRT has successfully identified the correct solution for this system of infinite solutions with remarkable accuracy. The positive outcomes, even in the case of the experimental problem (see Figure 5.30), suggest that this approach holds promise

for more challenging scenarios. Additionally, this methodology has demonstrated the potential for FBP to serve as an effective initial guess for other techniques. There is a prospect of extending this approach to various image reconstruction methods, where combining FBP with other methods may lead to even more accurate images than those achieved with FBP+SIRT.

Figure 5.29 – Reconstructed images of simulated Model 06 by using FBP initial guess approach

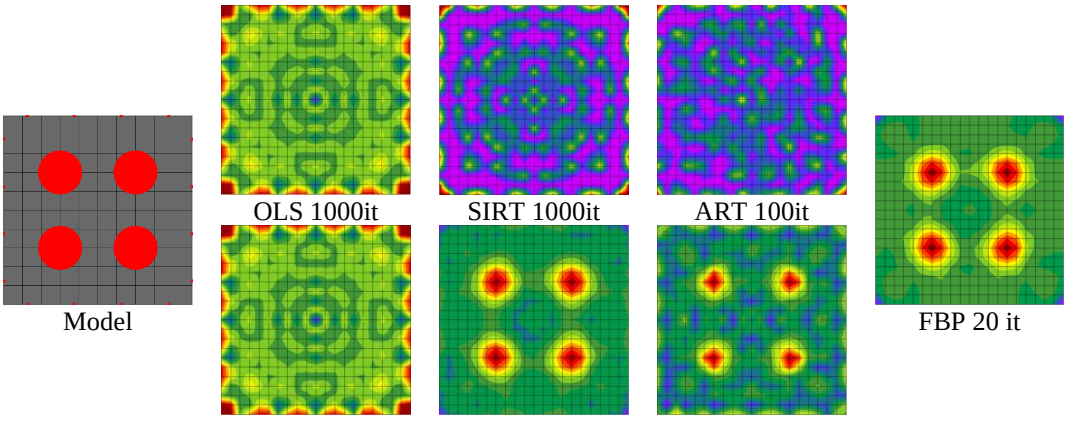

Source: the author.

Figure 5.30 – Reconstructed images of experimental Model 06 by using FBP initial guess approach

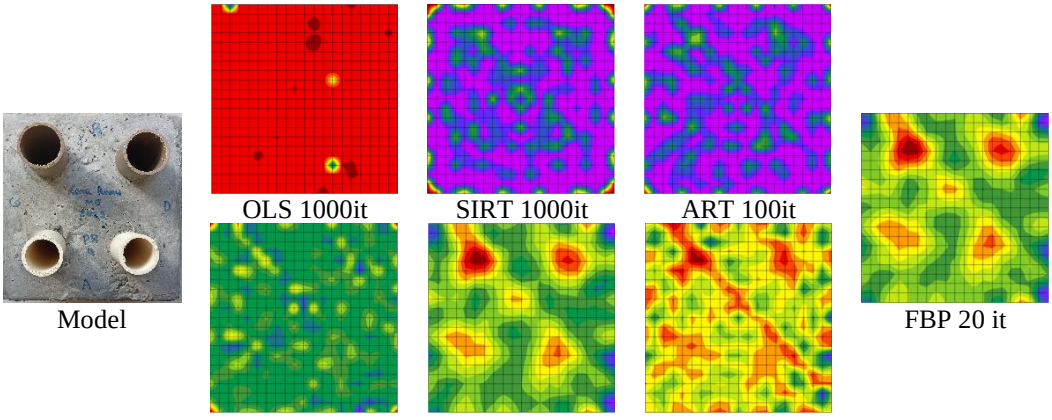

Source: the author.

6 CONCLUSIONS

The utilization of ultrasonic test results for image generation and drawing conclusions about the internal state of concrete structures represents a significant and challenging accomplishment. In summary, the findings from this study offer valuable insights into the effectiveness of various image reconstruction techniques in generating accurate images. The implementation of FBP and BP has proven promising, showcasing the ability to generate precise images with a relatively low number of acquired data and iterations.

The comparison between algebraic-based techniques (OLS, SIRT, and ART) and Backprojection approach revealed the importance of carefully considering the geometry of the studied element and the available data when choosing the reconstruction approach, along with the adopted mesh. OLS, SIRT, and ART showed they need a ratio between number of measurements and mesh nodes equal or bigger than 2.67, which means more data is necessary in order to increase the mesh and achieve best resolution. However, even for different studied geometry models (square or rectangular sections), mesh, and the number of measurement lines, BP demonstrated the capability to achieve high precision and accuracy in damage detection. FBP helped reduce BP images noise, and all square and rectangular sections reconstructed with this technique exhibited great improvements in resolution, which avoids human-based errors while visualizing the results. The most important achievement with FBP was the reconstruction of simulated models 01 to 06 with 20x20 mesh and 150 measurement lines with a very high accuracy, shape precision, and reduced noise. In contrast to algebraic techniques, which require constraints on maximum and minimum nodal coefficients and a large number of iterations to reconstruct images, FBP and BP reconstructed images without constraints and with only 1 iteration. Additional iterations were added to enhance accuracy, with 10 iterations proving sufficient for BP and 20 iterations for FBP.

Furthermore, the application of IDW interpolation, optimized by genetic algorithms, demonstrated the possibility of increasing the number of measurement lines with interpolated TOF values that were very accurate compared to simulated ones. However, it is crucial to recognize that the small error in interpolating TOF resulted in a decrease in ICC in images, which challenges the notion of using data interpolation to increase image accuracy. Despite this, the accurate results of IDW interpolation allowed the successful application of the idea of using data interpolation to reconstruct images with reduced data. With the help of IDW interpolation, it was possible to reconstruct images with FBP using only 12 measurement lines.

This proposed iterative approach to reduce the number of measurements in structural inspections stands out as a significant contribution to this study.

The use of ANN as interpolation tool for increase data was not successful. It was not possible to reach MSE lower than 10^{-5} for training and the error in predicting TOF caused changes in all reconstructed images. Despite the less-than-optimal outcomes observed in the current study, the analysis of ANN interpolation provides valuable insights into its predictive capabilities. The neural network demonstrated its potential, leveraging a limited dataset of 150 measurement lines to approximate ultrasound wave TOF values. The modest performance observed in terms of MSE suggests room for improvement. This could be achieved through refinements to the neural network's architecture, fine-tuning of parameters, and the exploration of more advanced programming languages, given the original implementation in Pascal.

The application of these methodologies to experimental models allowed for a comprehensive assessment of their robustness in build-structure scenarios. The comparative analysis involving algebraic techniques, BP, and FBP yielded consistent conclusions with the findings from the analysis of simulated models. However, a critical aspect emerged in the possibility of a comparative evaluation of velocity and attenuation tomography. These reconstructions demonstrated the feasibility of deriving two distinct images from a single set of ultrasound signals, providing complementary information. This capability proves instrumental in verifying the precise location and existence of damaged areas within structures.

Additionally, the study facilitated the determination of average velocity and attenuation values of p-waves in concrete. It highlighted discernible differences in these values attributable to the presence of damage. For instance, in the case of experimental Model 04, the attenuation exhibited a 14-fold increase due to the presence of voids. This sensibility underscores the diagnostic potential of ultrasound attenuation tomography in characterizing the internal condition of concrete structures, offering nuanced insights into their structural integrity.

The research successfully validated the two proposed innovative ideas, leveraging advancements in the field. The first idea, involving iterative measurements and IDW interpolation, proved effective. Starting with just 4 measurement lines and gradually increasing by 4 at each iteration, the methodology, aided by IDW interpolation, reconstructed simulated Model 01 with only 8 measurement lines and simulated Model 02 with only 12 measurement lines. Experimental Model 03 was also successfully reconstructed with a mere 20 measurement lines for velocity tomography, showcasing the potential for more efficient engineering inspections. The second innovative approach, which involves coupling techniques, utilizes an initial velocity FBP tomogram refined with algebraic methods. This approach showcased

significant enhancements in image accuracy specially adopting FBP+SIRT, indicating that FBP can be an effective starting point for other image reconstruction techniques. Furthermore, it underscores the importance of a non-constant initial guess for algebraic techniques to achieve convergence, highlighting the advantages of coupling techniques.

This study not only contributes to the enhancement of ultrasound tomography by showing these two new possible techniques BP and FBP but also underscores the importance of adapting approaches according to the complexity and specific characteristics of the objects under investigation. The results presented here show the possibilities of using ultrasound test to generate good quality images with reduced data in order to avoid workload and guarantee more productive and objective analysis of concrete structures.

6.1 Future work recommendations

- Study involving reinforcement: Extend the scope of the study to include experimental models with a combination of reinforcements and voids. This expanded investigation would provide valuable insights into the effectiveness of ultrasound tomography techniques in scenarios more closely resembling build structures.
- Advancements in Artificial Neural Network (ANN) interpolation: Address the limitations observed in the ANN interpolation technique. Explore and implement improvements in the ANN structure, training parameters, or alternative machine learning approaches to enhance the accuracy of interpolated measurements and subsequently improve image reconstruction quality.
- Intelligent point selection for proposed innovative data reduction approach: Develop intelligent algorithms or methodologies for selecting points in the innovative data reduction approach. Investigate strategies to optimize the selection process, ensuring that the chosen points contribute most effectively to accurate image reconstruction while minimizing the overall number of measurements.
- Comparative analysis of FBP against alternative methods: Conduct a comprehensive comparative study between FBP and alternative image reconstruction methods, including but not limited to Tikhonov regularization. Evaluate their respective strengths and weaknesses in various experimental and simulated models, shedding light on the most suitable method for different scenarios.

- FBP as initial guess for other reconstruction methods: Explore the application of FBP as an initial guess for other image reconstruction methods. Assess the impact of using FBP-derived initial conditions on convergence and accuracy in different scenarios.

These future work recommendations aim to refine and extend the current study, providing a basis for further advancements in ultrasound tomography techniques for concrete structural inspections. Each suggestion opens avenues for exploration, addressing specific aspects to enhance accuracy and applicability of the proposed methodologies.

REFERENCES

ABU ANAS, E. M.; CHENG, A.; SEIFABADI, R.; WU, Y. X. *et al.*, 2019, English, San Diego, CA. **CNN plus Back-projection: Limited Angle Ultrasound Tomography for Speed of Sound Estimation**. BELLINGHAM: Spie-Int Soc Optical Engineering, 2019.

AGGARWAL, A.; VASU, R. M., 2003, San Diego, Ca. **Imaging in turbid media by modified filtered back projection method using data from Monte Carlo simulation**. 2003. 314-324. Disponível em: <Go to ISI>://WOS:000185330600031.

AGGELIS, D. G.; SHIOTANI, T.; MOMOKI, S.; HIRAMA, A. Acoustic Emission and Ultrasound for Damage Characterization of Concrete Elements. **Aci Materials Journal**, 106, n. 6, p. 509-514, Nov-Dec 2009.

AGGELIS, D. G.; TSIMPRIS, N.; CHAI, H. K.; SHIOTANI, T. *et al.* Numerical simulation of elastic waves for visualization of defects. **Construction and Building Materials**, 25, n. 4, p. 1503-1512, Apr 2011.

ALMANSOURI, H.; CLAYTON, D.; KISNER, R.; POLSKY, Y. *et al.*, 2015, Minneapolis, MN. **Development of Acoustic Model-Based Iterative Reconstruction Technique for Thick-Concrete Imaging**. 2016.

ALMANSOURI, H.; JOHNSON, C.; CLAYTON, D.; POLSKY, Y. *et al.*, 2016, Atlanta, GA. **Progress Implementing a Model-Based Iterative Reconstruction Algorithm for Ultrasound Imaging of Thick Concrete**. 2017.

ALMANSOURI, H.; VENKATAKRISHNAN, S. V.; BUZZARD, G. T.; BOUMAN, C. A. *et al.*, 2018, English, Anaheim, CA. **DEEP NEURAL NETWORKS FOR NON-LINEAR MODEL-BASED ULTRASOUND RECONSTRUCTION**. NEW YORK: Ieee, 2018. 6-10.

ANASTASIO, M. A.; KUPINSKI, M. A.; PAN, X. C. Noise propagation in diffraction tomography: Comparison of conventional algorithms with a new reconstruction algorithm. **Ieee Transactions on Nuclear Science**, 45, n. 4, p. 2216-2223, Aug 1998. Article; Proceedings Paper.

ANDREUCCI, R. **Ultrasonic Testing.** São Paulo: Brazilian Association of Non-Destructive Testing - ABENDI, 2011. (In Portuguese)

ASL, M. N. A. S. A. Analytical image reconstruction methods in emission tomography. **Journal of Biomedical Science and Engineering**, 06, p. 100-107, 01 2013.

ASSOCIAÇÃO BRASILEIRA DE NORMAS TÉCNICAS. **NBR 8802:** Hardened concrete – Determination of ultrasonic wave propagation velocity. Rio de Janeiro: ABNT, 2019. (In Portuguese)

ASADOLLAHI, A.; KHAZANOVICH, L. Analytical reverse time migration: An innovation in imaging of infrastructures using ultrasonic shear waves. **Ultrasonics**, 88, p. 185-192, 2018.

BAO, K. Y.; LIU, C.; LI, J.; LIU, X. *et al.* Computed Tomography Image under Optimized Iterative Reconstruction Algorithm to Analyze the Characteristics of Blood Flow Field in

Cerebral Aneurysm before and after Stent Implantation. **Scientific Programming**, 2021, Dec 2021.

BASU, S.; THIRUMALAISELVI, A.; SASMAL, S.; KUNDU, T. Nonlinear ultrasonics-based technique for monitoring damage progression in reinforced concrete structures. **Ultrasonics**, 115, Aug 2021.

CAM, R. M.; VILLA, U.; ANASTASIO, M. A., 2022, English, Electr Network. **A learned filtered backprojection method for use with half-time circular Radon transform data**. BELLINGHAM: Spie-Int Soc Optical Engineering, 2022.

CAMASSA, D.; CASTELLANO, A.; FRADDOSIO, A.; PICCIONI, M. D. A New Ultrasonic Amplitude Tomography Approach, with Validation on Masonry Tuff Blocks. **Journal of Nondestructive Evaluation**, 39, n. 3, p. 19, Jun 2020. Article.

CHAI, H. K.; MOMOKI, S.; KOBAYASHI, Y.; AGGELIS, D. G. *et al.* Tomographic reconstruction for concrete using attenuation of ultrasound. **Ndt & E International**, 44, n. 2, p. 206-215, Mar 2011.

CHARAMBA, L. G. R. **Reconstruction of Tomographic Images using GPU**. 2013. 45 p. (Monograph) - Computer Engineering, Center for Informatics, Federal University of Pernambuco , Recife, 2013. (In Portuguese)

CHEN, W. T.; SHIH, C. C.; HUANG, C. C.; IEEE, 2011, Orlando, FL. **High Frequency Ultrasound Computed Tomography for Small Animal Imaging Applications**. 2011. 1415-1418.

CHOI, H.; BITTNER, J.; POPOVICS, J. S. Comparison of Ultrasonic Imagion Techniques for Full-Scale Reinforced Concrete. **Transportation Research Record**, n. 2592, p. 126-135, 2016. Article.

DREIFKE, Vinícius Mateus. **Analysis of methods for interpolation of environmental measurements in diffusing greenhouses**. 2019. Undergraduate Thesis (Bachelor's Degree in Computer Science) - Federal University of Santa Maria , Santa Maria, RS, 2019. (In Portuguese)

ESPINOSA, L.; BRANCHERIAU, L.; CORTES, Y.; PRIETO, F. *et al.* Ultrasound computed tomography on standing trees: accounting for wood anisotropy permits a more accurate detection of defects. **Annals of Forest Science**, 77, n. 3, Jul 2020.

EZELL, N. D. B.; VENKATAKRISHNAN, S. V.; AL MANSOURI, H.; SANTOS-VILLALOBOS, H. *et al.*, 2019, Denver, CO. **High fidelity ultrasonic imaging of concrete structures**. 2019.

FAN, H.; ZHU, H. Improved image reconstruction based on ultrasonic transmitted wave computerized tomography on concrete. **EURASIP Journal on Image and Video Processing**, 2018, n. 1, p. 129, 2018/11/19 2018.

FAN, H.; ZHU, H.; HAN, Q. Image reconstruction of concrete based on Filtered Backprojection method using ultrasonic time of flight data. **Computer Modelling and New Technologies**, 18, p. 72-78, 01 2014.

FAN, H. H.; ZHU, H. J.; ZHAO, X. R.; ZHANG, J. *et al.* Ultrasonic image reconstruction based on maximum likelihood expectation maximization for concrete structural information. **Computers & Electrical Engineering**, 62, p. 293-301, Aug 2017. Article.

FANG, X.; LI, Z. Q.; IEEE, 2009, Kiev, UKRAINE. **Study on Iterative Regularization Method in Ultrasonic Imaging Reconstruction for Concrete's Testing**. 2009. 213-216.

FREESEMAN, Katelyn; HOEGH, Kyle; KHAZANOVICH, Lev. Characterization of concrete at various freeze-thaw damage conditions using SH-waves. **AIP Conference Proceedings**, [S.L.], 2016. AIP Publishing LLC. http://dx.doi.org/10.1063/1.4940463.

GHOSH, D.; KUMAR, R.; GANGULI, A.; MUKHERJEE, A. Nondestructive Evaluation of Rebar Corrosion–Induced Damage in Concrete through Ultrasonic Imaging. **Journal of Materials in Civil Engineering**, 32, n. 10, p. 04020294, 2020.

GIGLIO, V. M. **Application of bioinspired algorithms in defining the optimal trajectory of ultrasonic pulses in concrete elements**. 2021. 159 p. (Master's Thesis) - Structural Engineering, University of São Paulo, São Carlos. (In Portuguese)

GOPI, V. P. A. F. T. K. A. P. P. Regularization based CT image reconstruction using Algebraic techniques, 2014, p. 1-3. DOI: 10.1109/ECS.2014.6892689.

HAACH, V. G. **Application of ultrasound as a non-destructive test for the evaluation of concrete elements.** 2017. Systematized Text (Habilitation Thesis) – School of Engineering of São Carlos, University of São Paulo, São Carlos, 2017. (In Portuguese)

HAACH, V. G.; JULIANI, L. M., 2014, Porto, PORTUGAL. **Application of ultrasonic tomography to detection of damages in concrete**. 2014. 3351-3357.

HAACH, V. G.; RAMIREZ, F. C. Qualitative assessment of concrete by ultrasound tomography. **Construction and Building Materials**, 119, p. 61-70, Aug 2016.

HANSEN, C.; SCHASSE, A.; HUTTEBRAUKER, N.; ASHFAQ, M. *et al.*, 2007, New York, NY. **Reconstruction of speed of sound for a correction of transit time in full angle spatial compounding**. 2007. 785-788.

HOEGH, K.; KHAZANOVICH, L.; MASER, K.; TRAN, N. Evaluation of Ultrasonic Technique for Detecting De lamination in Asphalt Pavements. **Transportation Research Record**, n. 2306, p. 105-110, 2012. Article.

HOEGH, K.; KHAZANOVICH, L.; YU, H. T. Ultrasonic Tomography for Evaluation of Concrete Pavements. **Transportation Research Record**, n. 2232, p. 85-94, 2011. Article.

HOEGH, K.; KHAZANOVICH, L.; YU, H. T. Concrete Pavement Joint Diagnostics with Ultrasonic Tomography. **Transportation Research Record**, n. 2305, p. 54-61, 2012. Article.

HOEGH, K.; KHAZANOVICH, L. Extended synthetic aperture focusing technique for ultrasonic imaging of concrete. **NDT & E International**, 74, p. 33-42, 2015.

HOU, W. X.; TAN, C.; BAO, Y.; DONG, F. Multi-frequency ultrasound tomography based on modified matrix regularization method and wavelet fusion. **Measurement Science and Technology**, 33, n. 8, p. 11, Aug 2022. Article.

HOYLE, C.; SUTCLIFFE, M.; CHARLTON, P.; MOSEY, S. *et al.* Limited-angle ultrasonic tomography back-projection imaging. **Insight**, 63, n. 1, p. 20-+, Jan 2021. Article.

HOYLE, F. W. A. B. S. Development and implementation of real-time ultrasound process tomography using a transputer network. **Parallel Computing**, 17, n. 6, p. 791-807, 1991.

HUANG, C. C.; CHEN, W. T. Developing high-frequency ultrasound tomography for testicular tumor imaging in rats: An in vitro study. **Medical Physics**, 41, n. 1, Jan 2014.

KAI LUO AND LIANG CHEN AND WEI LIANG AND HAOBO, W. A dual-scale morphological filtering method for composite damage identification using FBP. **Mechanical Systems and Signal Processing**, 184, p. 109683, 2023.

KAK, A. C.; SLANEY, M. **Principles of computerized tomographic imaging**. Philadelphia: Society for Industrial and Applied Mathematics, kak2001principles, 2001. 089871494X 9780898714944.

KIM, T. S.; DO, S. H.; MARMARELIS, V. Z., 2003, San Diego, Ca. **Multi-bond tissue differentiation in ultrasonic transmission tomography**. 2003. 41-48.

KORDJAZI, A.; COE, J. T.; AFANASIEV, M. A Hybrid Multi-Scale Full Waveform Inversion Approach to Evaluate the Structural Integrity of Drilled Shafts. *In*: **Geo-Congress 2020**, 2020. p. 190-199.

KWON, H.; JOH, C.; CHIN, W. J. Pulse Peak Delay-Total Focusing Method for Ultrasonic Tomography on Concrete Structure. **Applied Sciences-Basel**, 11, n. 4, p. 12, Feb 2021. Article.

KWON, J.; CHOI, S. J.; SONG, S. M. H., 2005, San Jose, CA. **Implementation and evaluation of the ultrasonic TOF tomography for the NDT of concrete structures**. 2005. 47-54. Disponível em: <Go to ISI>://WOS:000228796600005.

LEACH, R. R.; AZEVEDO, S. G.; BERRYMAN, J. G.; BERTETE-AGUIRRE, H. R. *et al.*, 2002, San Diego, Ca. **Comparison of ultrasound tomography methods in circular geometry**. 2002. 362-377. Disponível em: <Go to ISI>://WOS:000176292800038.

LI, N.; WANG, L. N.; JIA, J. B.; YANG, Y. J. A Novel Method for the Image Quality Improvement of Ultrasonic Tomography. **Ieee Transactions on Instrumentation and Measurement**, 70, p. 10, 2021. Article.

LI, N.; XU, K.; LIU, K.; HE, C. F. *et al.* A Novel Sensitivity Matrix Construction Method for Ultrasonic Tomography Based on Simulation Studies. **Ieee Transactions on Instrumentation and Measurement**, 68, n. 10, p. 3548-3562, Oct 2019. Article.

LI, S. L.; CHU, T. P. Super-Resolution Image Reconstruction for Ultrasonic Nondestructive Evaluation. **Ieee Transactions on Ultrasonics Ferroelectrics and Frequency Control**, 60, n. 12, p. 2575-2585, Dec 2013. Article.

LINDEN, R. **Genetic Algorithms**: An important tool in computational intelligence. Rio de Janeiro: Brasport, 2006. (In Portuguese)

LIU, H.; XIA, H. Y.; ZHUANG, M. W.; LONG, Z. J. *et al.* Reverse time migration of acoustic waves for imaging based defects detection for concrete and CFST structures. **Mechanical Systems and Signal Processing**, 117, p. 210-220, Feb 2019. Article.

NERIS, Airton Martins. **Evaluation of methods for spatial interpolation of precipitation data.** 2019. Undergraduate Thesis (Bachelor's in Information Systems) - Federal Rural University of Pernambuco, Recife, 2019. (In Portuguese)

MALHOTRA, V. M.; CARINO, N. J. **Handbook on Nondestructive Testing of Concrete**. CRC Press, 2004. 9780803120990.

MATHER, M. L.; BALDOCK, C. Ultrasound tomography imaging of radiation dose distributions in polymer gel dosimeters: Preliminary study. **Medical Physics**, 30, n. 8, p. 2140-2148, Aug 2003.

MENSAH, S.; FERRIERE, R. Near-field diffraction tomography. **Ultrasonic Imaging**, 24, n. 1, p. 13-24, Jan 2002.

MOLCHANOVA, O.; GEMMEKE, H.; ZAPF, M.; HOPP, T. *et al.*, 2022, English, Electr Network. **Wave-based ultrasound transmission tomography using the paraxial approximation in 2D**. BELLINGHAM: Spie-Int Soc Optical Engineering, 2022. Disponível em: <Go to ISI>://WOS:000836325500022.

NATTERER, F.; WUBBELING, F. A propagation backpropagation method for ultrasound tomography. **Inverse Problems**, 11, n. 6, p. 1225-1232, Dec 1995.

NG, Andrew. **CS230 Deep Learning**. Class notes. Stanford University, Online, 2022.

NIU, Z. R.; WANG, W.; HUANG, X. H.; LAI, J. Integrated assessment of concrete structure using Bayesian theory and ultrasound tomography. **Construction and Building Materials**, 274, Mar 2021.

ORISTAGLIO, M. L. A geometric approach to the filtered backpropagation algorithm. **Ultrasonic Imaging**, 5, n. 1, p. 30-37, 1983/01/01/ 1983.

PERDIOS, D.; VONLANTHEN, M.; MARTINEZ, F.; ARDITI, M. *et al.* CNN-Based Image Reconstruction Method for Ultrafast Ultrasound Imaging. **Ieee Transactions on Ultrasonics Ferroelectrics and Frequency Control**, 69, n. 4, p. 1154-1168, Apr 2022.

PEREZ-LIVA, M. *et al*. Speed of sound ultrasound transmission tomography image reconstruction based on Bézier curves. **Ultrasonics**, 103, p. 106097, 2020.

PERLIN, L. P.; PINTO, R. C. D. Use of network theory to improve the ultrasonic tomography in concrete. **Ultrasonics**, 96, p. 185-195, Jul 2019. Article.

PINTO, Paulo Marcos. **A methodology for designing low-pass Butterworth filters using FDDTAs**. 2021. Thesis (Doctorate in Electrical Engineering) - Federal University of Itajubá, Itajubá, 2021. (In Portuguese)

RADON, J. **On the determination of functions by their integral values along certain manifolds**. Reports of the Saxon Academy of Sciences, 69, p. 262–277, 1917. (In German)

RAHIMAN, M. H. F.; RAHIM, R. A.; RAHIM, H. A.; AYOB, N. M. N. Novel Adjacent Criterion Method for Improving Ultrasonic Imaging Spatial Resolution. **Ieee Sensors Journal**, 12, n. 6, p. 1746-1754, Jun 2012. Article.

RAHIMAN, M. H. F.; RAHIM, R. A.; RAHIM, H. A.; MUJI, S. Z. M. *et al.* ULTRASONIC TOMOGRAPHY - IMAGE RECONSTRUCTION ALGORITHMS. **International Journal of Innovative Computing Information and Control**, 8, n. 1B, p. 527-538, Jan 2012. Article.

RODRIGUEZ, A. R. M. **Computed Tomography:** Reconstruction Methods. Class notes. Autonomous University of San Luis Potosí, UASLP, 2021. (In Spanish)

SCHIAVON, K.F.B. **Study of the Application of Ultrasound in the Measurement of Stresses in Concrete Structures**. 2015. 130p. Dissertation (Master's in Structures) - School of Engineering of São Carlos, University of São Paulo, São Carlos, 2015. (In Portuguese)

SCHMITZ, K. J. L. A. M. B. A. T. K. A. K. M. A. V. Synthetic aperture focusing technique signal processing. **NDT International**, 19, n. 3, p. 177-189, 1986.

SCHRODER, U.; SCHUSTER, T. An iterative method to reconstruct the refractive index of a medium from time-off-light measurements. **Inverse Problems**, 32, n. 8, Aug 2016.

SOETOMO, K.; RAHMA, T. F.; JULIASTUTI, E.; KURNIADI, D. *et al.*, 2016, English, Bandung, INDONESIA. **Ultrasonic Tomography for Reinforced Concrete Inspection using Algebraic Reconstruction Technique with Iterative Kaczmarz Method**. NEW YORK: Ieee, 2016. 16-21.

SUZUKI, A.; TSUBOTA, Y.; WU, W. J.; YAMANAKA, K. *et al.*, 2019, English, San Diego, CA. **Full waveform inversion for ultrasound computed tomography with high-sensitivity scan method**. BELLINGHAM: Spie-Int Soc Optical Engineering, 2019.

TANG, T. H.; AZUMA, T.; SAKUMA, I.; IEEE, 2019, English, Glasgow, ENGLAND. **A High-Resolution USCT Echo Imaging Method with Reduced Data-Acquisition**. NEW YORK: Ieee, 2019. 2351-2354.

TSENG, C.-W.; CHANG, Y.-F.; WANG, C.-Y. Total Focusing Method or Phased Array Technique: Which Detection Technique Is Better for the Ultrasonic Nondestructive Testing of Concrete? **Journal of Materials in Civil Engineering**, 30, n. 1, p. 04017256, 2018.

URURE, R. M. Q. **Data interpolation based on contextual analysis for generating tomography images in cylindric specimens of concrete**. 2020. (Mestrado) - Faculdade de

Tecnologia da Universidade Estadual de Campinas, Universidade Estadual de Campinas Limeira.

VIEIRA, M. A. C. **Lesson 6 - Frequency Domain Processing**. 2019. 58 p. Class notes. (In Portuguese)

WAHAB, Y. A.; RAHIM, R. A.; RAHIMAN, M. H. F.; AW, S. R. *et al.* Inverse Problem: Comparison between Linear Back-Projection Algorithm and Filtered Back-Projection Algorithm in Soft-Field Tomography. **International Journal of Integrated Engineering**, 9, n. 4, p. 32-36, 2017. Article.

WANG, G.; CHEN, Y.; LI, Q. F.; LU, C. *et al.* Ultrasonic Computerized Tomography Imaging Method With Combinatorial Optimization Algorithm for Concrete Pile Foundation. **Ieee Access**, 7, p. 132395-132405, 2019. Article.

WANG, W. T.; LI, H.; WANG, C. H.; ZHOU, W. S. *et al.* An improved ultrasonic computerized tomography (UCT) technique for damage localization based on compressive sampling (CS) theory. **Structural Control & Health Monitoring**, 29, n. 6, p. 27, Jun 2022. Article.

WITTEN, A. J.; KING, W. C. Acoustic Imaging of Subsurface Features. **Journal of Environmental Engineering**, 116, n. 1, p. 166-181, 1990.

YANAGIDA, H.; TAMURA, Y.; KIM, K. M.; LEE, J. J. Development of ultrasonic time-of-flight computed tomography for hard wood with anisotropic acoustic property. **Japanese Journal of Applied Physics Part 1-Regular Papers Brief Communications & Review Papers**, 46, n. 8A, p. 5321-5325, Aug 2007. Article.

YU, M.; LI, J. H.; LI, Y.; YU, L. J. Optimized Algebraic Reconstruction Algorithm Based Hemodynamic Changes in Color Doppler Ultrasound in Monitoring the Patients with Colorectal Cancer Undergoing Peripherally Inserted Central Catheter and Catheterization Nursing. **Scientific Programming**, 2021, p. 9, Dec 2021. Article.

ZAYED, A. I. Hilbert transform associated with the fractional Fourier transform. **IEEE Signal Processing Letters**, vol. 5, no. 8, pp. 206-208, ago. 1998. 10.1109/97.704973.

ZHANG, W.; TAN, C.; DONG, F. Wide Angle Ultrasonic Transmission Tomography by Sparse Preimaged OMP Algorithm. **Ieee Transactions on Instrumentation and Measurement**, 69, n. 9, p. 6262-6270, Sept 2020. Article.

ZHU, Z. Q.; YU, B.; LI, Y. N.; XIAO, J. Y. *et al.* Simulation study on ultrasonic tomography for grouted reinforced concrete by finite element. **Journal of Central South University**, 22, n. 7, p. 2791-2799, Jul 2015.

ZIELIŃSKA, M.; RUCKA, M. Detection of debonding in reinforced concrete beams using ultrasonic transmission tomography and hybrid ray tracing technique. **Construction and Building Materials**, 262, p. 120104, 2020/11/30/ 2020.


PPG
SET


EESC • USP